THE ZONAL MEAN STRUCTURE OF CLOUDS AND HAZE ON SATURN FROM CASSINI/CIRS OBSERVATIONS

By

HSIN - JUNG LIN

A DISSERTATION PRESENTED TO THE GRADUATE SCHOOL
OF THE UNIVERSITY OF FLORIDA IN PARTIAL FULFILLMENT
OF THE REQUIREMENTS FOR THE DEGREE OF
DOCTOR OF PHILOSOPHY

UNIVERSITY OF FLORIDA

2012

© 2012 Hsin - Jung Lin

To my family and friends

ACKNOWLEDGMENTS

I would not have finished my Ph.D. program without the help and support from my parents, advisors, committee members, professors and many friends.

I would like to express my deepest gratitude to my thesis advisor, Dr. Katia Matcheva, for kindly recruiting me in the end of my third graduate year; I would like to thank Dr. Matcheva for her support, encouragement and relentless patience during the past three and half years. I would also like to thank my committee members in the physics department, Dr. David Tanner, Dr. James Fry and Dr. Steve Detweiler, as well as the external committee member in the astronomy department, Dr. Jian Ge, for their advice on my dissertation and research. My appreciation also goes to my previous advisor, Dr. Guido Mueller, and colleagues in LIGO for teaching me to think critically and put theory into practice.

I would also like to thank Dr. John Sabin, Dr. Robert DeSerio, and Mr. Charles Parks, for assisting me to overcome language barrier and helping me deal with student issues while I was a teaching assistant. A special thanks is given to Dr. John Sabin for his being my substituting committee member during my final examination.

Thanks to the staff in the physics department, especially Pam Marlin, David Hansen, Janet Germany, Martin Meder, and Kristin Nichola for helping me prepare for all the necessary paperwork and solving IT problems so I would be able to focus on my research. I would also like to show my gratitude to Pam Marlin for always making sure that I got paid and registered for the incoming semester on time.

I am grateful to my parents and many of my friends for their support and for keeping me sane through these difficult years : my parents for always encouraging me to pursue my goal; Tzu-Yi Tsai for being my best friend of 15 years and helping me overcome all the difficulties in my life; Hsiu-Shan Liu for going to the football games with me for two seasons; Tzu Ting (Helen) Lin for being a loyal running partner and always being willing to have dinner with me; Tucker Ringger as a buddy and a biking partner; Jeffery

Hoskins and Richard Ottens for showing me American cultures as well as dragging me away from my work for something fun whenever I needed a break; Katherine Dooley for supporting me remotely from Louisiana and from Germany; Shih-Fen Yeh, Hsuan Hsu, Ryan Wong, Jack Chen and Shizuko Okusa for cooking meals for me and playing Algricola with me; Wenya Wang for passing the information about Dr. Matcheva's search for a Ph.D. student so I could be introduced to the wonders of planetary science; many internet friends who were also working on their graduate degrees for accompanying me during the years of my Ph.D. studies.

In the end of the acknowledgements, I want to give my special thanks to Tzu Ting (Helen) Lin and Katherine Dooley for spending countless hours editing my dissertation.

TABLE OF CONTENTS

page

ACKNOWLEDGMENTS 4

LIST OF TABLES 8

LIST OF FIGURES 9

ABSTRACT 12

CHAPTER

1 INTRODUCTION 13

1.1 Overview 13
1.2 Motivations for the Research 14
1.3 Outline of the Dissertation 16

2 OBSERVATIONS AND DATA ANALYSIS 18

2.1 Cassini / CIRS Overview 18
2.2 Data Analysis 20
2.2.1 MIRMAP Observations 20
2.2.2 Coverages and Emission Angles 21
2.2.3 Sensitivity Study of the Data 22
2.2.4 Brightness Temperature Maps at 1392 cm^{-1} 25
2.2.4.1 Global brightness temperatures from 2005 to 2007 25
2.2.4.2 Latitudinal variations of brightness temperatures 27
2.2.4.3 Calibration and data quality 29

3 RETRIEVAL ALGORITHM AND NUMERICAL MODEL 69

3.1 Introduction 69
3.2 Forward Model 69
3.3 Retrieval Method 72
3.4 Functional Derivative Matrix K 75
3.4.1 K_{ij} for the Temperature Retrievals 76
3.4.2 K_{ij} for the Clouds/Haze Retrievals 77
3.5 Error Analysis 79
Error Analysis for Cloud/Hazes Retrievals 80

4 TEMPERATURE RETRIEVAL 82

4.1 Introduction 82
4.2 Results and Discussion 84
4.2.1 Stratospheric Temperature 84
4.2.2 Tropospheric Temperature and Temperature Knee 85

5 CLOUD RETRIEVAL 103

5.1 Introduction 103
5.2 Numerical Experiment 104
5.3 χ^2 Minimization Approach 106
5.4 Cloud Retrieval Results and Discussion 108

6 SUMMARY 119

REFERENCES 122

BIOGRAPHICAL SKETCH 126

LIST OF TABLES

Table page

1-1 Observed properties of Saturn, Jupiter and Earth. 17

2-1 Summary of the CIRS MIRMAPs used in this work 33

2-2 Spectral range used for the temperature and cloud inversions. 35

2-3 600 cm^{-1} 35

2-4 1304 cm^{-1} 35

2-5 1392 cm^{-1} 35

LIST OF FIGURES

Figure page

2-1 CIRS Focal Plane Locations. 36

2-2 Noise Equivalent Spectral Radiance for FP3 and FP4 at 2.8 cm^{-1} spectral resolution during Jupiter encounter in 2000. 37

2-3 MIRMAP coverage in 2005. 38

2-4 MIRMAP coverage in 2006. 39

2-5 MIRMAP coverage of Saturn's northern hemisphere in 2007. 40

2-6 MIRMAP coverage of Saturn's southern hemisphere at latitudes between 7°S and 80°S in 2007. 41

2-7 MIRMAP coverage in 2009. 42

2-8 MIRMAP coverage in 2010. 43

2-9 Emission angles of MIRMAP observations. 44

2-10 Reference atmospheric structure of Saturn. 45

2-11 Synthesized spectrum based on the reference atmospheric structure. 46

2-12 Pressure level of unity optical depth in nadir-viewing geometry. 47

2-13 Sensitivity study to the abundance of phosphine. 48

2-14 Sensitivity study to the abundance of ammonia. (1000 - 1200 cm^{-1}) 49

2-15 Sensitivity study to the abundance of ammonia. (1350 - 1490 cm^{-1}) 50

2-16 Brightness temperature map at 1392 cm^{-1} from 2005 MIRMAP observations in the southern hemisphere. 51

2-17 Brightness temperature map at 1392 cm^{-1} from 2007 MIRMAP observations in the southern hemisphere. 52

2-18 Brightness temperature map at 1392 cm^{-1} from 2006 MIRMAP observations in the northern hemisphere. 53

2-19 Number of radiances at 1392 cm^{-1} averaged for brightness temperature calculation in 2005. 54

2-20 Number of radiances at 1392 cm^{-1} averaged for brightness temperature calculation in 2007. 55

2-21 Number of radiances at 1392 cm^{-1} averaged for brightness temperature calculation in 2006. . . . 56

2-22 Zonal mean brightness temperature at 1392 cm^{-1} from 2005 to 2007. . . . 57

2-23 Zonal mean brightness temperature at 1392 cm^{-1} of the southern hemisphere in 2005 and 2007. . . . 58

2-24 Zonal mean brightness temperature at 1392 cm^{-1} in 2005 compared with the modeled brightness temperature retrieved from the reference atmosphere without clouds and hazes. . . . 59

2-25 Discontinuity in the brightness temperature at 1392 cm^{-1}. (2005 MIRMAP observations) . . . 60

2-26 Discontinuity in the brightness temperature at 1392 cm^{-1}. (2007 MIRMAP observations) . . . 61

2-27 Number of spectra used in MIRMAP observations at 60°S in 2005 for cold calibration (Deep Space). . . . 62

2-28 Number of spectra used in MIRMAP observations at 60°S in 2005 for warm calibration (Shutter closed). . . . 63

2-29 Variances of the zonal mean brightness temperature of the southern hemisphere in 2005. . . . 64

2-30 Variances of the zonal mean brightness temperature of the northern hemisphere in 2006. . . . 65

2-31 Variances of the zonal mean brightness temperature of the southern hemisphere in 2007. . . . 66

2-32 Spectra of the MIRMAP observations 009A007 and 009B007 in FP3 spectral range. . . . 67

2-33 Spectra of the MIRMAP observations 009A007 and 009B007 in FP4 spectral range. . . . 68

3-1 Flow chart of the retrieval algoritm. . . . 81

4-1 Initial temperature profiles for temperature retrievals. . . . 88

4-2 Contribution function for CH_4 at 27°S in 2005. . . . 89

4-3 Contribution function for H_2 at 27°S in 2005. . . . 90

4-4 Temperature profile at 27°S in 2005 after the second stage of temperature retrieval. . . . 91

4-5 Temperature profile at 77°S in 2005 after the second stage of temperature retrieval. . . . 92
4-6 Partial spectrum (1200 - 1400 cm^{-1}) at 27°S in 2005 after the first stage of temperature retrieval. . . . 93
4-7 Partial spectrum (1200 - 1400 cm^{-1}) at 77°S in 2005 after the first stage of temperature retrieval. . . . 94
4-8 Partial spectrum (590 - 750 cm^{-1}) at 27°S in 2005 after the second stage of temperature retrieval. . . . 95
4-9 Partial spectrum (590 - 750 cm^{-1}) at 77°S in 2005 after the second stage of temperature retrieval. . . . 96
4-10 Spectrum at 27°S in 2005 after temperature retrieval. . . . 97
4-11 Spectrum at 77°S in 2005 after temperature retrieval. . . . 98
4-12 Temperature profile at 27°S in 2005 after the first stage of temperature retrieval. 99
4-13 Temperature profile at 77°S in 2005 after the first stage of temperature retrieval. 100
4-14 Retrieved temperature of southern hemisphere in 2005. . . . 101
4-15 Retrieved tropospheric temperature knee in 2005. . . . 102
5-1 Cloud absorption coefficient of the numerical experiment. . . . 111
5-2 Optical thickness of the numerical experiment. . . . 112
5-3 Results of χ^2 minimization approach. . . . 113
5-4 Cloud retrieval results (a). . . . 114
5-5 Cloud retrieval results (b). . . . 115
5-6 Cloud retrieval results (c) 116
5-7 Retrieved cloud with uncertainties. . . . 117
5-8 Spectrum of the retrieved cloud. . . . 118

Abstract of Dissertation Presented to the Graduate School
of the University of Florida in Partial Fulfillment of the
Requirements for the Degree of Doctor of Philosophy

THE ZONAL MEAN STRUCTURE OF CLOUDS AND HAZE ON SATURN FROM CASSINI/CIRS OBSERVATIONS

By

Hsin - Jung Lin

December 2012

Chair: Katia I. Matcheva
Major: Physics

Clouds and haze can be used as a tracer for the dynamic activities and seasonal circulation of Saturn's atmosphere. The vertical distributions of clouds and haze can also provide a strong constraint on the chemical and physical process of the planet. Furthermore, knowledge of the composition of Saturn's atmosphere also contributes to information about the models of the Solar System formation as well as the evolution of the gas giants. The vertical distribution of clouds and haze on Saturn has been researched from ground-based, space-based and spacecraft observations. In this work, we use the Cassini/CIRS mid-infrared MIRMAP data from 2005 to 2008 during the Prime Mission to study the latitudinal distribution of clouds and haze both in the southern and northern hemispheres. We develop a retrieval algorithm and provide error analysis for temperature and clouds/haze retrievals.

CHAPTER 1
INTRODUCTION

1.1 Overview

Saturn, with its magnificent ring system and 62 natural satellites, is the second largest planet in the Solar System. It is mostly composed of molecular hydrogen ($96.3\% \pm 2.4\%$), helium ($3.25\% \pm 2.4\%$) and methane (4500 ± 2000 ppm); its mean bulk density is 687 kg/m^3 (Williams, 2012).

Saturn rotates extremely rapidly at a rate of 10 hours and 32 minutes per revolution (Anderson and Schubert, 2007) with 26.73° obliquity to the orbit (Williams, 2012). The rapid rate of rotation causes Saturn to be an oblate spheroid, and this obliquity similar to the Earth[1] drives Saturn's seasonal cycle in the atmosphere. The mean distance from Saturn to the Sun is 9.5 AU[2] (Irwin, 2009), the resultant solar irradiance (flux) is 14.99 W/m^2, and the effective temperature[3] is 82.4 K. The effective temperature of Saturn is significantly smaller than the observed mean bolometric temperature[4] (95 K). This indicates the emitted thermal energy of Saturn exceeds the absorbed solar energy, which can be explained by internal heat sources.[5]

The composition and vertical structure of the atmospheric properties of Saturn are similar to those on Jupiter, the other gas giant in the solar system. A comparison of the

[1] Earth has 23.44° obliquity.

[2] 1 AU $= 1.494 \times 10^8$ km.

[3] The effective temperature of a planet is the blackbody temperature at which solar radiation is balanced by the emitted radiation of the planet.

[4] The bolometric temperature is the mean blackbody temperature at which the planet actually radiates.

[5] One possible source of the internal heat is due to the internal differentiation of helium (Irwin, 2009).

observed properties of the two gas giants, Saturn and Jupiter, with Earth are listed in Table 1-1.

1.2 Motivations for the Research

The atmosphere of Saturn is observed to be meteorologically active and highly convective. Clouds have been used as tracers for the dynamic activities of gas giants. The variations of chemical compounds as well as the optical properties of clouds and haze provide information of Saturn's atmospheric dynamic process and seasonal circulation. The pressure level of cloud and haze layers is sensitive to the mixing ratios of the chemical compounds. The vertical distribution of clouds and haze in the troposphere and in the stratosphere will provide a strong constraint on the physical and chemical process in the atmosphere of Saturn.

In addition, studying Saturn's atmospheric structure does not only assist us to obtain knowledge of gas giants, but it would also improve our current understanding of meteorological phenomena observed on Earth. Furthermore, the understanding of the composition of Saturn's atmosphere also provides constraints on models of the Solar System formation, which are the foundations for exoplanetary research.

Our understanding of the clouds and haze on Saturn has originated mostly from ground-based observations and space-based observations, such as the Hubble Space Telescope. In addition, information retrieved from spacecraft missions, like Voyager 1, Voyager 2, and the Cassini-Huygens mission, has also offered significant contributions to the study of Saturn.

Equilibrium Cloud Condensation Model (Atreya et al., 1999; Weidenschilling and Lewis, 1973) predicts that there are three layers of clouds in the atmosphere of Saturn. These thermochemical-predicted cloud layers are an aqueous-ammonia cloud based at the pressure level of 20 bar, an ammonium hydrosulfide cloud at the pressure level of about 6 bar, and a top ammonia ice cloud with a base at around 2-bar pressure level with the condensible volatiles taken as $5\times$ solar (Atreya and Wong, 2005).

Above the top cloud deck located at 1 - 2 bar pressure level, numerous studies (e.g., Karkoschka and Tomasko, 1992; 1993; 2005; Munoz et al., 2004; Ortiz et al., 1996; Stam et al., 2001; Temma et al., 2005) illustrate that there is a stratospheric haze layer of particles with a small radius of $r \sim 0.1 - 0.2\mu m$ at the pressure of 1 - 100 mbar, and there is a tropospheric haze layer with particle size of $r \geq 0.5\mu m$ from the tropopause (near 100 mbar) down to the top of the first condensation cloud deck at 1.5 - 2.0 bar with possible aerosol-free gaps in between.

Stratospheric haze particles (ethane, acetylene, and other hydrocarbon products) presumably originates from photolysis process of methane (Irwin, 2009). Tropospheric haze is expected to form from the condensation of the ammonia gas; if the atmospheric vertical mixing is efficient, clouds can extend to the upper boundary of the convective region, which is at about 500 - 600 mbar (Bzard et al., 1984). However, no spectral signature of solid ammonia has been observed near 3 μm, where such feature would be expected (Kerola et al., 1997). Kerola et al. (1997) indicate that the topmost tropospheric aerosols are not made of pure ammonia ice, which may have provided the explanation for the absent spectral feature. Compared with the stratospheric haze, the tropospheric haze is considered to have a larger optical depth and its pressure level exists over a wider range.

Regardless of the different optical properties and diverse forming mechanism of both haze layers, both the tropospheric and stratospheric haze layers show hemispherical asymmetry between the northern and southern hemispheres on Saturn. Tropospheric haze shows strong hemispherical asymmetry due to seasonally varying photochemical and condensation processes combined with aerosol microphysical processes (Stam et al., 2001), and its concentration and thickness vary latitudinally. The stratospheric haze also has seasonal asymmetry for having a larger optical depth in the fall hemisphere than in the spring hemisphere (Munoz et al., 2004).

Different data-analysis models and retrieval methods have been used to extract information about the vertical distribution and composition of Saturn's atmosphere. However, the number of the cloud and haze layers, the optical properties of the vertical profiles, as well as the presence of the aerosol-free gap between layers are not fully constrained from the previous observations. For the purpose of providing an alternative analysis with a different spectral range and retrieval method, we use CIRS MIRMAP data of the Cassini-Huygens mission (Flasar et al., 2004) with a mid-infrared spectral range centered at 1392 cm^{-1} and a retrieval algorithm used in Matcheva et al. (2005) to retrieve the vertical structure of the clouds and haze on Saturn.

1.3 Outline of the Dissertation

This work is focused on 27° latitudes in the southern hemisphere in 2005 during the Prime Mission (2004 - 2008) of the Cassini mission immediately after Saturn's southern summer solstice. We will describe the MIRMAP data sets and several parameters used in this work in Chapter 2. The numerical models used for temperature and cloud retrieval are described in Chapter 3. Retrieved results for the temperature and the clouds are discussed in Chapter 4 and Chapter 5, respectively.

Table 1-1. Observed properties of Saturn, Jupiter and Earth.

Property	Saturn	Jupiter	Earth
Solar distance [AU]	9.5	5.2	1
Sidereal orbital period [yr]	29.5	11.9	1
Equatorial radius [km]	60268	71492	6378
Mean density [kg/m^3]	700	1330	5515
Equatorial surface gravity at 1 bar [m/s^2]	9.1	23.1	9.81
Sidereal day	10 hr 32 min♣ (System III)	9hr 55 min (System III)	23 hr 56 min
Obliquity	26.73°⋆	3°	23.5°
Bolometric temperature [K]	95	124	255
Equilibrium radiating temperature [K]	82	110	255
Number of natural satellites#	62	67	1
Planetary ring system	Yes	Yes	No

Data reference :
Irwin (2009)
♣ Anderson and Schubert (2007)
⋆ Williams (2012)
NASA planetary fact sheets for Saturn, Jupiter, and Earth.

CHAPTER 2
OBSERVATIONS AND DATA ANALYSIS

2.1 Cassini / CIRS Overview

The NASA-ESA joint Cassini-Huygens orbiter launched in October 1997. It had a short flyby of Jupiter in December 2000 with a closest approach of approximately 136 Jupiter radii (Flasar et al., 2004), and it then entered the Saturnian system in 2004. In July 2004, the Huygens Probe separated from the Cassini Orbiter after the Saturn Orbit Insertion (SOI) and entered the atmosphere of Titan to make in situ measurements during an approximately 150 minute descent in January 2005. In July 2004, the Cassini Orbiter started the first four-year Prime Mission tour of the exploration of Saturn, its rings, satellites, and magnetosphere via 75 orbits about Saturn and close flybys of its satellites along with many radio and solar occultations. After completing a successful four-year Prime Mission in 2008, a two-year extended mission named Equinox Mission (EM) and a seven-year Extended-Extended Mission (XXM) called Solstice Mission (SM) were initiated in June 2008 and in September 2010 separately. With the time span of these missions (about half of the Saturn year), we are able to observe the seasonal variations in the Saturnian system.

The Cassini Orbiter is a three-axis stabilized spacecraft designed for 27 diverse science investigations (Flasar et al., 2004). It carries 12 onboard instruments including four optical remote sensing instruments (Composite Infrared Spectrometer, Imaging Science Subsystem, Ultraviolet Imaging System, and Visible and Infrared Mapping Spectrometer), two microwave remote sensing instruments (Cassini Radar and Radio Science Subsystem), and instruments for particles, waves and fields studies (Cassini Plasma Spectrometer, Cosmic Dust Analyzer, Ion and Neutral Mass Spectrometer, Magnetometer, Magnetospheric Imaging Instrument, and Radio and Plasma Wave Science). The Cassini Mission investigates the physical, chemical as well as temporal properties of Saturn, its rings, icy satellites, magnetosphere, and the largest moon Titan.

The Composite Infrared Spectrometer (CIRS) is an infrared Fourier Transform Spectrometer (FTS) among one of the 12 instruments onboard the Cassini Orbiter. Its design is based on the Voyager Infrared Interferometer Spectrometer (IRIS) with extended far-infrared coverage, improved sensitivity and spectral resolution. CIRS measures the thermal emission in wavenumber from 10 to 1400 cm^{-1} (1 mm to 7 μm) with a selectable spectral resolution from 0.5 to 15.5 cm^{-1} (Flasar et al., 2004). The far-Infrared spectrum is measured with a polarization interferometer with a focal plane labeled FP1 (5 - 695 cm^{-1}) consisting of two thermopile detectors with a 3.9 mrad Field of View (FOV). The mid-infrared part of the spectrum is measured with a conventional Michelson interferometer with two focal planes FP3 (570 - 1125 cm^{-1}) and FP4 (1025 - 1495 cm^{-1}), both of which is composed of a 1×10 array of HgCdTe detectors, with 0.273 mrad FOV. Figure 2-1 shows the CIRS field of views projected on the sky.

CIRS has both nadir-viewing and limb-viewing capability to perform different observations. The limb-viewing capability allows CIRS to provide vertical profiles of atmospheric variables with highly resolved resolution of one scale height or better in the stratosphere and the mesosphere. In this geometry, the sensitivity to the minor constituents is enhanced due to the long absorber paths viewed against a cold space background. The vertical resolution of nadir sounding is very limited. However, the advantage is that the nadir-viewing has better horizontal space resolution with less cloud and aerosol interferences.

CIRS, with the variable spacecraft-to-Saturn range, is not only able to provide vertical profiles of the target scientific objectives, but it also has the capacity to construct global maps of temperature and chemical composition to study the southern and northern hemispheric asymmetry due to the inclination of the rotational axis. In addition, with about half of the Saturn year timespan of the combined Prime Mission

and the extended missions,[1] CIRS can also observe the seasonal variation of Saturn's atmospheric constituents.

2.2 Data Analysis

2.2.1 MIRMAP Observations

In order to retrieve the cloud and haze profiles in the atmosphere of Saturn, we choose a series of Saturn mapping observations by CIRS known as MIRMAPs from February 2005 to June 2010. MIRMAP observation used in this work acquired thermal emission from Saturn's atmosphere at a single latitude with 2.8 cm^{-1} spectral resolution for roughly one Saturn day while the planet rotated beneath the spacecraft. The spacecraft kept a distance of 25 - 40 Rs (radius of Saturn) from the planet, with the long axis (Z axis) of the CIRS arrays pointing toward the pole of Saturn (Cassini/CIRS, 2012), giving a spatial resolution of 1.1° to 1.7°. Fletcher et al. (2009) calculated the fields of views (FOVs) by scaling the footprint of the instrument to degree-latitudes at the equator, and these calculations showed the FOVs of MIRMAP observations from 2005 to 2008 are about 0.75° - 1.6°. Each data set contains at least a thousand spectra calibrated with about 50 to 100 deep space spectra. The Noise Equivalent Spectral Radiance (NESR) is the signal for which the signal-to-noise ratio (SNR) is unity (Flasar et al., 2004). The NESR of the data with 2.8 cm^{-1} spectral resolution for FP3 and FP4 do not vary significantly with frequency (see Fig. 2-2), and we can use the averaged NESR for error analysis. The averaged NESR is 7.811314×10^{-9} $Wcm^{-2}sr^{-1}(cm^{-1})^{-1}$ for FP3 and is 1.601580×10^{-9} $Wcm^{-2}sr^{-1}(cm^{-1})^{-1}$ for FP4 respectively. A summary of the MIRMAP observations from 2005 to 2010 is listed in Table 2-1.

[1] Cassini-Huygens missions started in July 2004, shortly after Saturn's southern summer solstice (October 2002), until the end of the Cassini Solstice Mission in May 2017, which will be a few months past Saturn's northern summer solstice.

2.2.2 Coverages and Emission Angles

MIRMAP data collected during the Prime Mission were measured while the spacecraft was sitting at the near-equatorial orbit, and the emission angles for the observations varied from 0° to around 75°. Latitudinal coverage for both hemispheres were built up over the span of a few months. The southern hemisphere coverage was obtained in 2005, 2007 and 2009, while the northern hemisphere coverage was obtained in 2006, 2007 and 2010. Fig. 2-3 to 2-8 show the FP4 MIRMAP coverage from 2005 to 2010.[2] In these figures, a set of five close parallel lines in the same color represent the coverage of a individual observation sequence.

During each MIRMAP observation, CIRS uses one of four pre-programmed observation modes called PAIRS when processing signals collected from each mid-infrared focal plane. Although there are 10 detectors each for FP3 and FP4, CIRS has only five solid-state 'channels' for post-detection signal processing (Nixon, 2011). Hence, there are exactly five data points in each array of the focal plane that can be processed at a time. When PAIRS mode is activated[3] , 10 detectors of each focal plane are divided into 5 pairs. In each pair, the signals of individual detectors would be combined before being processed. Therefore, as we can see in Fig. 2-3 as an example, there are 5 data lines per latitudinal band for a single observation (shown in the same color) when the spacecraft is scanning over the planet.

Saturn orbits around the Sun every 29.5 Earth years, so atmospheric properties will not show large scale seasonal variations in the MIRMAP observations from 2005 to 2007. When comparing the data from 2005, 2006, and 2007 MIRMAP observations with those from 2009 and 2010, the data from 2005 to 2007 have better southern and northern hemispherical coverages. With the data coverages of 85°S - 75°N

[2] FP3 coverages and emission angles are similar to those of FP4.

[3] Database ID Code 1 - 5 for FP3, and 36 - 40 for FP4

in these three years, we are able to observe the hemispherical asymmetry of the atmospheric properties in the beginning of the Cassini Prime Mission (right after Saturn's southern summer solstice). However, consistency of the emission angles within the same latitudinal bands is important if we need to co-add the apodized spectra from different MIRMAP observations. When examining the latitudinal variations of the brightness temperatures at particular wave numbers, we also need to take emission angle variations into consideration. Fig. 2-9 shows that the emission angles in 2007 for Saturn's northern hemisphere do not increase steadily along latitudes, and they have about a 20° discrepancy compared with 2006 MIRMAP data at mid-latitudes. Therefore, when analyzing the hemispherical asymmetry of brightness temperature, data from the northern hemisphere in 2007 will not be included.

2.2.3 Sensitivity Study of the Data

To construct the global temperature maps and to retrieve the vertical clouds/haze profiles of Saturn's atmosphere, we need to select the appropriate spectral range from the nadir mid-infrared measurements. We first examined the sensitivity of Saturn's thermal emission to a number of atmospheric parameters, including mixing ratios and optical depth of hydrogen (H_2), methane (CH_4), ammonia (NH_3), phosphine (PH_3), and hydrocarbons, such as C_2H_2 and C_2H_6. Fig. 2-10 presents the reference atmosphere structure of Saturn, showing the volume mixing ratios of some main atmospheric constituents (excluding H_2, CH_4, and He) varying with pressure. Other constituents such as H_2O, GeH_4, CO, AsH_3 and CO_2 do not contribute much to the mid-infrared spectrum and were neglected from the reference model.

The reference phosphine vertical profile is based on rotational line observations by Orton et al. (2000; 2001). The PH_3 volume mixing ratio is 7.4×10^{-6} at 645 mbar and drops linearly in log-log scale to a value of 4.3×10^{-7} at 150 mbar due to photolysis. The reference vertical distribution of ammonia followed results from Voyager 2 by Courtin et al. (1984). NH_3 saturates at pressures near 1.3 bar, and its abundance decreases

more rapidly than PH_3 with altitude due to condensation and photolysis in the upper troposphere (Fouchet et al., 2009) and almost becomes negligible at tropopause. The vertical distributions of C_2H_2 and C_2H_6 are assumed based on the research by Moses and Greathouse (2005) to increase with altitude. The volume mixing ratio of He/H_2 is a fixed value of 0.135 based on the Voyager/IRIS result from 200 - 600 cm^{-1} by Conrath and Gautier (2000). Theoretical models predicted that methane does not condense and is well-mixed throughout Saturn's atmosphere. In our model, we assumed the volume mixing ratio of CH_4/H_2 is 5.3×10^{-3} based on the retrieved result by Fletcher et al. (2009).

Combining the composition profiles mentioned above with an a priori vertical temperature profile from Voyager/IRIS observations (Courtin et al., 1984), we then can generate a synthetic mid-infrared spectrum shown in Fig. 2-11. This synthesized spectrum shows the spectral features contributed by different atmospheric species. For example, C_2H_2, C_2H_6 and CH_4 have strong emitting features at 625-825 cm^{-1}, 700-900 cm^{-1} and 1150-1350 cm^{-1} respectively, whilst PH_3 and NH_3 appear in absorption relative to the background continuum between 900-1200 cm^{-1}.

Vertical temperature profiles of Saturn can be retrieved from the ν_4 methane band at 1200 - 1400 cm^{-1} and S(1) and S(2) collision-induced absorption (CIA) lines with the translational continuum from 590 to 700 cm^{-1}. The methane emissive region provides information on lower stratospheric temperatures at few mbar in nadir-viewing observations. Temperature information in the upper troposphere and the tropopause at few hundred mbar could be extracted in the CIA continuum region.

The Equilibrium cloud condensation model (ECCM) predicted that, on Saturn, the top ammonia ice cloud base is located at around 2 bar with the condensible volatiles being $5\times$ solar (Atreya and Wong, 2005). This is deeper than the top cloud base in Jupiter due to the colder temperature. To obtain information on the aerosol distribution above the top cloud layer, we need to find spectral regions, where CIRS can probe as

deep as possible in nadir-viewing mode based on the reference atmospheric structure of Saturn. We then further construct a figure to infer the unity optical depth at different wavenumbers in nadir-viewing geometry, which provides information of deepest probing pressure level based on the known atmospheric constituents. As shown in Fig. 2-12, the deepest probing wavenumbers are presented in the regions between 1100 and 1200 cm^{-1} as well as in the region between 1390 and 1450 cm^{-1}. CIRS can potentially sample around 900 mbar at 1392 cm^{-1} and 600 mbar between 1100-1200 cm^{-1} in a clear atmosphere of Saturn, assuming there are no influences from clouds and haze. Due to the increasing emission angles of higher latitudes, the altitudes at the same spectral regions that CIRS can sample would become higher. Nevertheless, CIRS is still able to probe as deep as 700 mbar and 500 mbar within these two deep probing regions respectively.

The atmospheric opacity of the spectrum between 1100 and 1200 cm^{-1} is mostly provided by the absorption of phosphine and ammonia. The abundance of PH_3 and NH_3 varies significantly as the result of the global atmospheric circulation and the local atmospheric dynamics, and therefore the abundance of these two constituents is not well constrained. We performed a series of sensitivity experiments similar to the sensitivity studies in Matcheva et al. (2005) to examine how the spectrum between 1100 and 1200 cm^{-1} varies with the mixing ratios of PH_3 and NH_3. The spectra in FP4 spectral range shown in Fig. 2-13, Fig. 2-14 and Fig. 2-15 present how the spectra vary if we were to set the mixing ratio one tenth or ten times the reference PH_3 or NH_3 abundances. PH_3 emission between 1100 and 1200 cm^{-1} is significantly modified by the change of the abundance. This change of the abundances has almost no effect on the spectrum at wavenumber larger than 1250 cm^{-1} as shown in Fig. 2-13. The change of NH_3 abundance would also modify the spectrum at 1000-1200 cm^{-1} and the region larger than 1460 cm^{-1} as shown in Fig. 2-14 and 2-15. The NH_3 spectrum modification is not as significant as that of PH_3 due to the small mixing ratio in the

upper troposphere, but it is still sensitive to the mixing ratio variation. Therefore, the unconstrained abundances of both constituents make the deep probing region between 1100 and 1200 cm^{-1} hard to extract useful information for vertical cloud and haze structures. It is also difficult to look for any latitudinal or global variations of the cloud properties.

The narrow spectral window centered at 1392 cm^{-1} is free of influence of ammonia and phosphine. The spectrum near 1392 cm^{-1} is only constructed by the CH_4 and H_2 gaseous absorbers (Flasar et al., 2004), whose mixing ratios are well-mixed throughout Saturn's atmosphere and are well studied. In our work, we choose a spectral window between 1389 and 1395 cm^{-1} for clouds and haze retrievals.

Spectral regions used for temperature and cloud/haze inversions in this work along with related information are listed in Table 2-2.

2.2.4 Brightness Temperature Maps at 1392 cm^{-1}

2.2.4.1 Global brightness temperatures from 2005 to 2007

Brightness temperature maps of Saturn's southern hemisphere from 2005 and 2007 CIRS MIRMAP observations at 1392 cm^{-1} are shown in Fig. 2-16 and Fig. 2-17, and the map from 2006 observations of the northern hemisphere is shown in Fig. 2-18. The thermal emission of Saturn's atmosphere is not expected to vary much seasonally in one year, and averaging the calibrated data would eliminate the temporal atmospheric fluctuations. To obtain these yearly brightness temperature maps, we co-added and averaged the calibrated intensities at 1392 cm^{-1} within rectangles of 4° in latitude and 6° in longitude, with 2° latitudinal and 1.5° longitudinal overlapping between the adjacent rectangles. White blocks in these maps correspond to regions of data with low signal-to-noise ratio or regions containing no data. The temperature is decreasing with altitude in the troposphere; a low brightness temperature at 1392 cm^{-1} indicates that the emission originates at a lower pressure level (higher altitude). In this work, we assume

that the horizontal temperature variations at 1392 cm^{-1} are very small near the pressure level at which CIRS is sensitive.

The belt and zone structures on Saturn are less clear than those on Jupiter, so we do not see clear boundaries for zones and belts in the global brightness temperature maps as expected. However, these brightness temperature maps still reveal several interesting properties, which are listed below.

In the map from 2005 (Fig. 2-16), the brightness temperature is slightly increasing towards the equator in the equatorial region at latitudes less than 15°S. The lowest brightness temperature is observed between 15°S and 65°S in the low and mid-latitudes. For latitudes higher than 65°S, the brightness temperature is significantly higher compared with that in the low and mid-latitude regions; and the brightness temperature in the polar region is about 10 - 15K higher than that in the equator. If we take the viewing geometry into consideration, the tropospheric temperature would be decreasing with the elevated emission angle toward the pole with the emission angle minimum at 8° in 2005 (Fig. 2-9), which makes the unexpected increasing brightness temperature at higher latitudes even more pronounced. The presence of high stratospheric absorbers may be the reason for the large amount of temperature increase at high latitudes.

The map in 2007 (Fig. 2-17) presents bands of higher brightness temperature centered at 10°S, 30°S, 55°S, and 78°S with about 5K higher compared to the neighboring lower temperature regions. The temperature is not increasing towards the polar region for latitudes higher than 65°S as seen in the map of 2005. With no data at latitudes higher than 80°S and no further data analysis, we are not able to determine if the high brightness temperature band located at 78 °S indicates an increasing temperature trend, or if it is simply a local band structure at high latitudes. These band or belt features shown in the 2007 map may be corresponding to the zonal motions in the upper troposphere, or they could simply be a results of the fluctuations due to the co-added spectra from different observations. Another cause for the observed

latitudinal variations may be related to the calibration of the raw data, and it will be discussed in section 2.2.4.3.

Through a comparison of the southern hemisphere maps from 2005 and 2007 (Fig. 2-16 and Fig. 2-17) to the northern hemisphere map from 2006 (Fig. 2-18), we can observe that the brightness temperatures on average in the northern hemisphere are colder than those in the southern hemisphere. This is likely due to more solar insolation on the southern hemisphere immediately after southern summer solstice. The map in 2006 also shows no clear band or belt structures at 1392 cm^{-1}.

2.2.4.2 Latitudinal variations of brightness temperatures

To see the latitudinal variation of the zonal mean brightness temperatures (ZMTb) of 1392 cm^{-1} based on observations from 2005 to 2007, we averaged all the measured radiance of the same year at 1392 cm^{-1} within a 4° latitudinal band centered at each latitude. We then converted the mean radiance to a mean brightness temperature via Planck function. The number of entries in the averaged radiance at 1392 cm^{-1} for each latitude is shown in Fig. 2-19, Fig. 2-20 and Fig. 2-21.

In Fig. 2-22, we can see the large scale asymmetry of brightness temperature in the northern and southern hemispheres due to the seasonal effect (Cess and Caldwell, 1979). The ZMTb in the northern hemisphere is about 5 K, on average, colder than that in low and mid-latitudes of the southern hemisphere. For latitudes higher than 60°S in the southern hemisphere, there is a significant elevation towards the polar region in 2005. In 2007, ZMTb is also increasing in a similar manner for latitudes higher than 70°S. The highest ZMTb in the southern hemisphere is about 10K warmer than the ZMTb at the average level in the northern hemisphere.

If we compare the ZMTb in 2005 with that in 2006 in Fig. 2-22, it seems like in the northern and southern hemispheres there are small scale variations symmetric with respect to the equator, which may be related to Saturn's symmetric zonal jet system and the ring shadow effect. The ZMTb in 2005 and in 2007 should show similar behavior

because the two-year timespan is relatively short when compared with a full Saturn year (29.7 Earth years), and will not cause much change in the insolation of the southern atmosphere. However, Fig. 2-23 shows that the ZMTbs are not correlated latitudinally in 2005 and 2007, which should show similar patterns if the variations are due to the same global atmospheric circulation on Saturn. Therefore, the small scale latitudinal variations may have resulted from systematic measurement errors or caused by noise.

In order to analyze the vertical distribution of the clouds and haze in Saturn's atmosphere, we focus on the latitudes where the data may provide clear information about aerosols. We first ran several quick temperature retrievals[4] for different latitudes and compared the calculated brightness temperature at 1392 cm^{-1} with the observed latitudinal ZMTb in 2005, as shown in Fig. 2-24.

The expected zonal brightness temperatures (blue line in Fig. 2-24) are calculated from the spectrum generated from the retrieved vertical temperature profiles at different latitudes, assuming that there are no clouds or haze in the atmosphere. At 1392 cm^{-1}, the emission comes from a pressure level deeper than 500 mbars, where the temperature varies with height following the dry adiabatic lapse rate. If the emission angle of the measurement is constant, then the calculated temperature at 1392 cm^{-1} should be a horizontal straight line, which corresponds to the temperature at certain height in a clear atmosphere. If the emission angle increases with latitude, the retrieved brightness temperature decreases towards the polar region as shown in Fig. 2-24 because the emission comes from higher altitudes in the troposphere.

For latitudes higher than 70°S, the observed ZMTb is about 5-8K warmer than the expected brightness temperature assuming no clouds or atmospheric aerosols, while the observed ZMTb is about 10 K colder than the expected one at low and mid-latitudes.

[4] Details of the forward model and the retrieval algorithm will be discussed in the following chapter.

Lower observed temperatures than the expected one can be explained by the presence of clouds or haze in the upper troposphere; warmer than expected temperatures are possibly due to haze in the lower stratosphere at pressure less than 100 mbar where the temperature is higher.

The observed brightness temperature map implied diverse physics properties which may indicate different vertical structures of clouds and haze for low and mid-latitudes compared to high-latitudes. To verify the statements above, we use the MIRMAP observations in 2005 to perform cloud inversions at 27°S for low and mid-latitudes as well as 77°S for high latitudes. The inversion model and the retrieved results will be discussed in the following chapters.

2.2.4.3 Calibration and data quality

Calibrations. After a careful examination of the band and belt structures shown in the global brightness temperature map in Fig. 2-16 and Fig. 2-17, we can see that there is temperature discontinuity at latitudes centered at 5°S, 19°S, 43°S and 60°S in the 2005 data, while in 2007, there are also discontinuities centered at 13°S, 20°S, 50°S and 60°S. Those regions are boxed and shown in Fig. 2-25 and Fig. 2-26. After a careful inspection of the apodized spectra and other information corresponding to the calibrations, we found that those brightness temperature discontinuities may be related to the calibration of the instrument.

The array detectors of FP3 and FP4 are operated at the temperature range of 75K to 80K, and this temperature is different from the operating temperature of the interferometer, which is around 170K. For calibration of mid-infrared spectra, CIRS has to use deep space reference interferograms at around 2.7K (cold) and internal shutter reference interferograms at 170K (warm) when the shutter is closed. The calibration method also requries Fourier transforms and the use of complex power spectra, which makes the calibration challenging. The detail of the calibration algorithm is beyond the

scope of this dissertation. Interested readers may wish to refer to Flasar et al. (2004) and Carlson (2001) for further information.

During the MIRMAP observations, FP3 and FP4 are viewing both cold and warm targets periodically. If we take brightness temperature centered at 60°S in 2005 MIRMAPs as an example, the latitudinal coverage between 53°S and 66°S are mainly from two MIRMAP observations, 004MIRMAP1392A039 and 004MIRMAP1392B039. The colder brightness temperature between 150° and 330° in longitude corresponds to the different cold calibrating sequences as shown in Fig. 2-27, while the warm calibration sequences shown in Fig. 2-28 appear to contribute little to the discontinuity in the brightness temperature bands. Other brightness temperature discontinuities are also related to discontinuity of the cold or warm calibration during observations. However, we also noticed that not all the discontinuities in the calibration will cause a discontinuity in the brightness temperature zonal bands. Warm calibrations appear to have less influence on these discontinuities compared to the cold calibrations.

To show the variances of the brightness temperature for each latitude, we first averaged all the radiances in a block of 4° in latitude and 6° in longitude with 1.5° longitudinal overlapping. From there, we converted the mean radiances into the brightness temperature at 1392 cm^{-1} using the Planck function. The brightness temperature variance for each 4° latitudinal band is the standard deviation based on the averaged results of 237 blocks along the same latitudinal band. Red vertical lines in Fig. 2-29 and Fig. 2-31 show the variances of the zonal mean brightness temperature in the southern hemisphere in 2005 and 2007; Fig. 2-30 shows the variances of the zonal mean brightness temperature in the northern hemisphere in 2006. In 2005, the variance is from 2 K to 10 K as shown in Fig. 2-29, and the variance is smaller for higher zonal mean brightness temperatures at higher latitudes in the southern hemisphere. In 2006, as shown in Fig. 2-30, the variances of the zonal mean brightness temperature in the northern hemisphere are much larger, and it may be a result of the low signal-to-noise

ratios for these observations. In 2007, Fig. 2-31 illustrates that the variance is from 2.5 K to 16.5 K, and the variance is smaller for zonal mean brightness temperatures higher than 125 K. The large variance in these figures indicates that the small meridional variations of the zonal mean brightness temperature may be a consequence of a systematic error or due to the low signal-to-noise ratios during the measurements.

Data Quality. HgCdTe detector arrays of FP4 are expected to have the highest performance near 80 K in the spectral range of 7 - 9 μm. However, as shown in the figure in Flasar et al. (2004), the average bandpass spectral response of these 10 detectors is unity centered around 1200 cm^{-1}, and the response decreases to 0.8 near 1400 cm^{-1}. Hence, the signal-to-noise ratio for these detectors of FP4 are smaller near 1392 cm^{-1}.

To check the MIRMAP data quality, we use observations 009A007 and 009B007 in 2005 and 050028 and 050B028 in 2007 to see if the zonal mean brightness temperatures are consistent for consecutive observations. In the experiment, we chose 27°S as an example. For each observation listed above, we used three different methods to calculate the zonal mean brightness temperature at 600 cm^{-1}, 1304 cm^{-1}, and 1392 cm^{-1}, respectively.

Method A is to calculate the averaged brightness temperature by using all the radiances within a 4° latitudinal bin centered at 27°S, which is the standard procedure for calculating the zonal mean brightness temperature in our work. Method B is to calculate the mean intensities in small rectangles centered at 27°S of 4° in latitude and 6° in longitude with 1° longitudinal overlapping. And the average brightness temperature is then calculated based on the positive averaged intensities in those rectangles. Method C is similar to method B, but instead of using 4° x 6° rectangles, we used 4° x 4° squares for the mean brightness temperature. The experiment results are listed in Table 2-3, Table 2-4 and Table 2-5.

For these three different wavenumbers, if the measurement had good longitudinal coverage, then method A, B and C will provide similar averaged brightness temperatures. The measurements used for calculation covered approximately 360° in longitude, and for each observation, the measurement last for about one Saturn day. Ideally, the averaged zonal radiances at the same latitude band should not vary dramatically for consecutive measurements. For the wavenumber at 600 cm^{-1} and 1304 cm^{-1}, the differences of the averaged brightness temperatures centered at 27°S of two consecutive observations are less than 1 K in 2005 and less than 2.5 K in 2007. However, at 1392 cm^{-1}, which is the spectral region for cloud retrievals, the differences between the consecutive observations are about 5 K in both 2005 and 2007.

Fig. 2-32 and Fig. 2-33 show the spectra at 27°S of the 2005 observations 009A007 (red line) and 009B007 (green line) in the FP3 and FP4 spectral range, respectively. The general shape of the spectra in FP3 and in FP4 are similar for both observations. Those spectra match especially well in the methane emission region between 1150 and 1350 cm^{-1}. However, as the signal-to-noise ratio decreases towards the spectral edge of each focal plane, the spectra of these consecutive observations are not consistent.

Based on the results shown above, MIRMAP data at 27°S will have smaller error bars for temperature retrievals if only data at 590 - 700 cm^{-1} and 1250 - 1350 cm^{-1} are used. However, the uncertainties for inversions of clouds and haze will be large if data at the wavenumber larger than 1350 cm^{-1} are used.

Table 2-1. Summary of the CIRS MIRMAPs used in this work

Observations	Sequence	Year	Duration	Latitude Covered	Start SCET	End SCET	Range (km)
003SA_MIRMAPA001	S08	2005	19 hr 30 m	40°S-60°S	1109042460	1109112660	2204100
003SA_MIRMAPA003	S08	2005	11 hr	30°S-50°S	1109158560	1109198160	2424737
003SA_MIRMAPB003	S08	2005	11 hr	30°S-50°S	1109234160	1109273760	2528366
004SA_MIRMAPA039	S09	2005	11 hr	50°S-70°S	1109676000	1109715600	2590282
004SA_MIRMAPB039	S09	2005	11 hr	50°S-70°S	1109751600	1109791200	2509606
006SA_MIRMAPA004	S10	2005	10 hr 50 m	71°-85°S	1114233240	1114272240	2438399
007SA_MIRMAPB004	S10	2005	11 hr	71°-85°S	1114311000	1114350600	2449009
008SA_MIRMAPA006	S11	2005	11 hr 40 m	60°S-80°S	1117078740	1117120740	2090136
008SA_MIRMAPB006	S11	2005	10 hr 17m	60°S-80°S	1117166340	1117203360	2248117
009SA_MIRMAPA007	S11	2005	10 hr 25 m	26°-33°S	1118628840	1118666340	2042730
009SA_MIRMAPB007	S11	2005	11 hr	26°-33°S	1118703840	1118743440	2192441
010SA_MIRMAPA008	S12	2005	11 hr	10°S-30°S	1120276140	1120315740	2191238
010SA_MIRMAPB008	S12	2005	8 hr 30 m	10°S-30°S	1120351200	1120381800	2306071
011SA_MIRMAPA009	S12	2005	11 hr	0°-20°S	1121652000	1121691600	1682126
011SA_MIRMAPB009	S12	2005	11 hr	0°-20°S	1121736120	1121775720	1933113
012SA_MIRMAPA002	S13	2005	12 hr 17 m	0°S-10°S	1123463820	1123503420	2237457
012SA_MIRMAPB002	S13	2005	9 hr 42 m	0°S-10°S	1123540920	1123580520	2341344
023SA_MIRMAPA010	S19	2006	11 hr	5°N-15°N	1145602800	1145642400	3025640
023SA_MIRMAPB010	S20	2006	11 hr 45 m	5°N-15°N	1145689200	1145731500	2810285
023SA_MIRMAP011	S20	2006	20 hr 29 m	15°N-25°N	1147124580	1147198320	2875805
025SA_MIRMAPA012	S21	2006	11 hr	25°N-35°N	1151122920	1151162520	2730276
025SA_MIRMAPB012	S21	2006	11 hr	26°N-34°N	1151208420	1151248020	2478734
026SA_MIRMAP013	S21	2006	21 hr 26 m	34°N-47°N	1152724380	1152801540	2915013
026SA_MIRMAP014	S22	2006	11 hr 30 m	55°N-65°N	1154308800	1154350200	2621692
028SA_MIRMAP015	S23	2006	12 hr 45 m	46°N-54°N	1157492700	1157538600	1935292
030SA_MIRMAP036	S24	2006	21 hr 30 m	66°N-73°N	1161171600	1161249000	2063491

Table 2-1. Continued.

Observations	Sequence	Year	Duration	Latitude Covered	Start SCET	End SCET	Range (km)
046SA_MIRMAP024	S31	2007	21 hr 14 m	10°S-30°S	1182195900	1182272340	2264004
047SA_MIRMAPB024	S31	2007	11 hr	0°-20°S	1182309300	1182348900	2299727
048SA_MIRMAP025	S31	2007	20 hr 30 m	30°S-50°S	1184008920	1184082720	2881444
048SA_MIRMAP026	S32	2007	21 hr 30 m	40°S-60°S	1185382260	1185459660	2352865
049SA_MIRMAP027	S33	2007	11 hr 30 m	50°S-70°S	1188948000	1188989400	2676443
050SA_MIRMAP037	S34	2007	21 hr 30 m	60°S-80°S	1190555460	1190632860	2779837
050SA_MIRMAP028	S34	2007	11 hr	20°S-40°S	1191538740	1191578340	2127765
050SA_MIRMAPB028	S34	2007	11 hr	20°S-40°S	1191617520	1191657120	2336377
112SA_MIRMAP001	S50	2009	21 hr 10 m	43°N-48°N	1244154120	1244230320	1490000
118SA_MIRMAP001	S53	2009	23 hr 17 m	36°S-48°S	1254028380	1254112200	2632500
122SA_MIRMAP001	S55	2009	22 hr 41 m	4°S-4°N	1259803080	1259884740	2405000
122SA_MIRMAP002	S55	2009	15 hr 40 m	12°S-19°S	1259975880	1260084540	2010000
123SA_MIRMAP001	S55	2009	23 hr 00 m	27°S-34°S	1261406760	1261489560	1920000
125SA_MIRMAP001	S56	2010	20 hr 55 m	26°N-34°N	1264148700	1264224000	1970000
126SA_MIRMAP001	S57	2010	22 hr 25 m	40°S-50°S	1266615780	1266696480	2335000
129SA_MIRMAP001	S58	2010	23 hr	11°N-19°N	1270022940	1270105740	2345000
130SA_MIRMAP001	S59	2010	20 hr 55 m	46°N-58°N	1273022820	1273098120	2551500
132SA_MIRMAP001	S60	2010	23 hr	45°S-55°S	1276155420	1276238220	2278000

Table 2-2. Spectral range used for the temperature and cloud inversions.

Retrieved parameter	Property	Spectral range (cm^{-1})	Pressure range (mbar)
Temperature	CH_4	1250 - 1350	0.3 - 5
Temperature	H_2	590 - 700	80 - 300
Clouds/haze	gray cloud	1389 - 1395	300-800

Table 2-3. 600 cm^{-1}

	2005 observations		2007 observations	
	009A007	009B007	050028	050B028
A	93.83 K	94.01 K	94.32 K	91.60 K
B	93.83 K	93.99 K	94.08 K	91.59 K
C	93.83 K	93.99 K	94.07 K	91.56 K

Table 2-4. 1304 cm^{-1}

	2005 observations		2007 observations	
	009A007	009B007	050028	050B028
A	142.54 K	142.07 K	141.94 K	142.58 K
B	142.54 K	142.07 K	141.97 K	142.55 K
C	142.52 K	142.07 K	141.97 K	142.56 K

Table 2-5. 1392 cm^{-1}

	2005 observations		2007 observations	
	009A007	009B007	050028	050B028
A	118.97 K	123.78 K	126.39 K	131.20 K
B	118.21 K	122.90 K	125.90 K	131.06 K
C	118.69 K	122.78 K	125.84 K	131.04 K

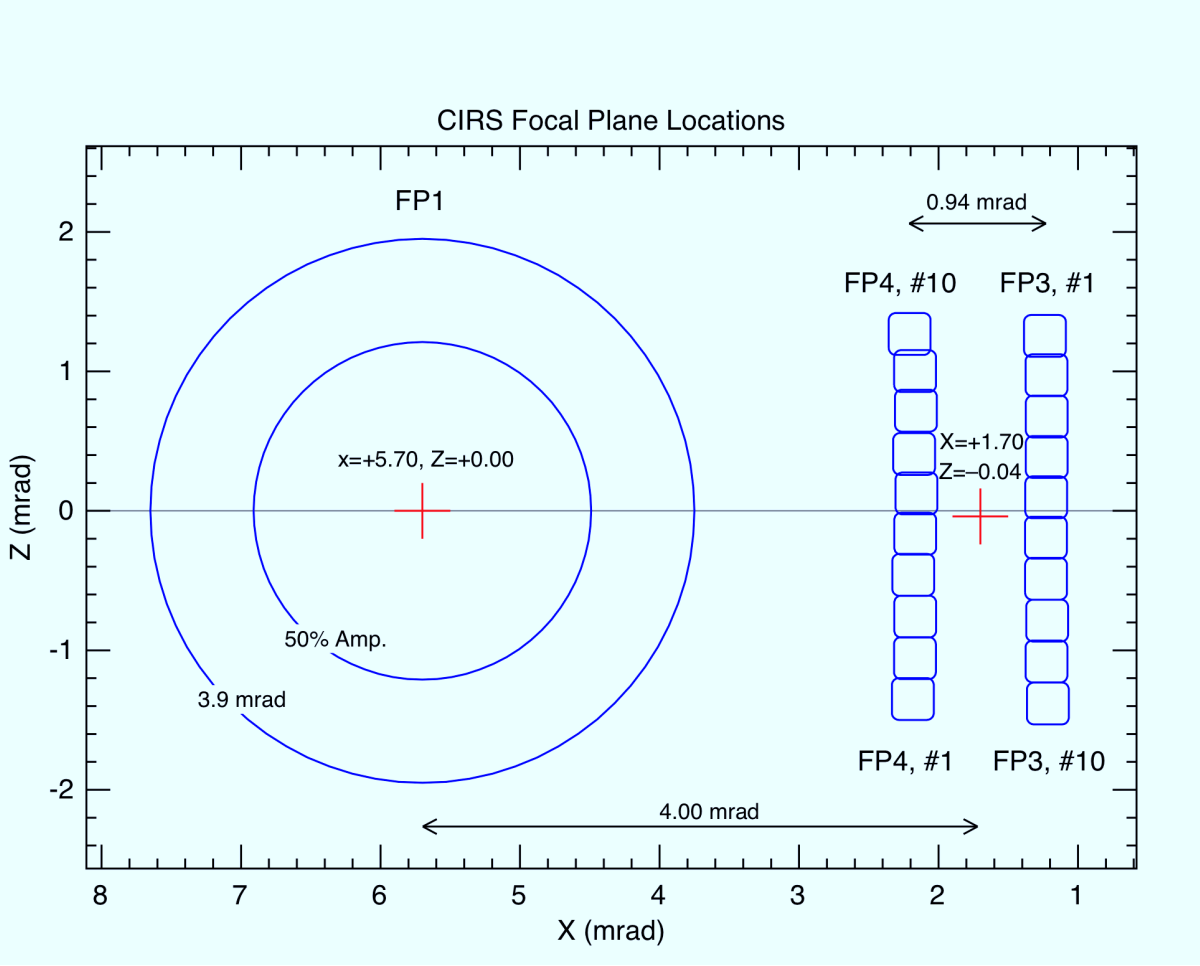

Figure 2-1. CIRS Focal Plane Locations. FP1 is the far-infrared interferometer with FOV of 3.9 mrad, and it covers the spectral range from 5 to 695 cm^{-1}. The mid-infrared interferometers contains two focal plane arrays FP3 (570 - 1125 cm^{-1}) and FP4 (1025 - 1495 cm^{-1}). Each array has 10 detecters with 0.297 mrad FOV. This graph is taken from the Fig. 3 in CIRS_FOV_OVERVIEW.pdf of the PDS archive co-s-cirs-234-tsdr-v31. This graph is also shown in Flasar et al. (2004)

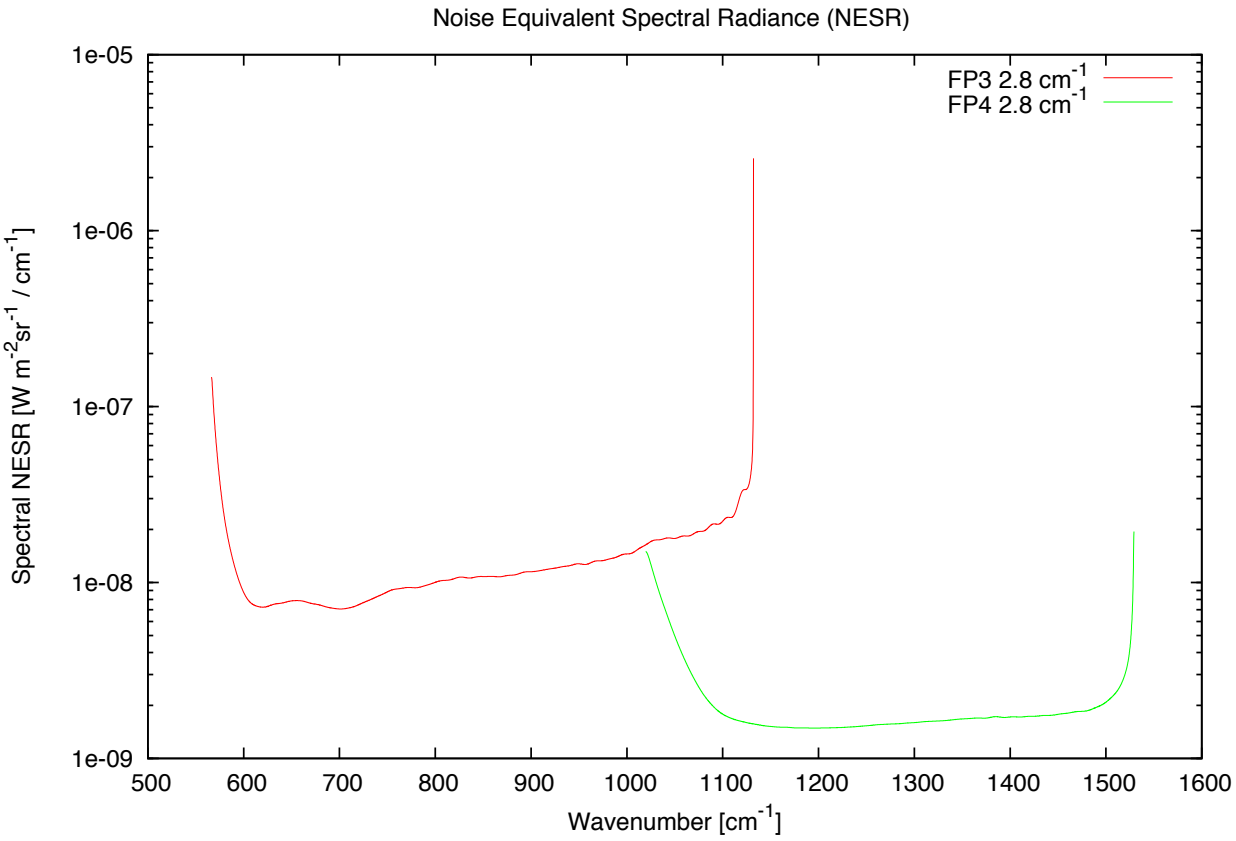

Figure 2-2. Noise Equivalent Spectral Radiance for FP3 and FP4 at 2.8 cm^{-1} spectral resolution during Jupiter encounter in 2000. Calculation of NESR is described in Flasar et al. (2004).

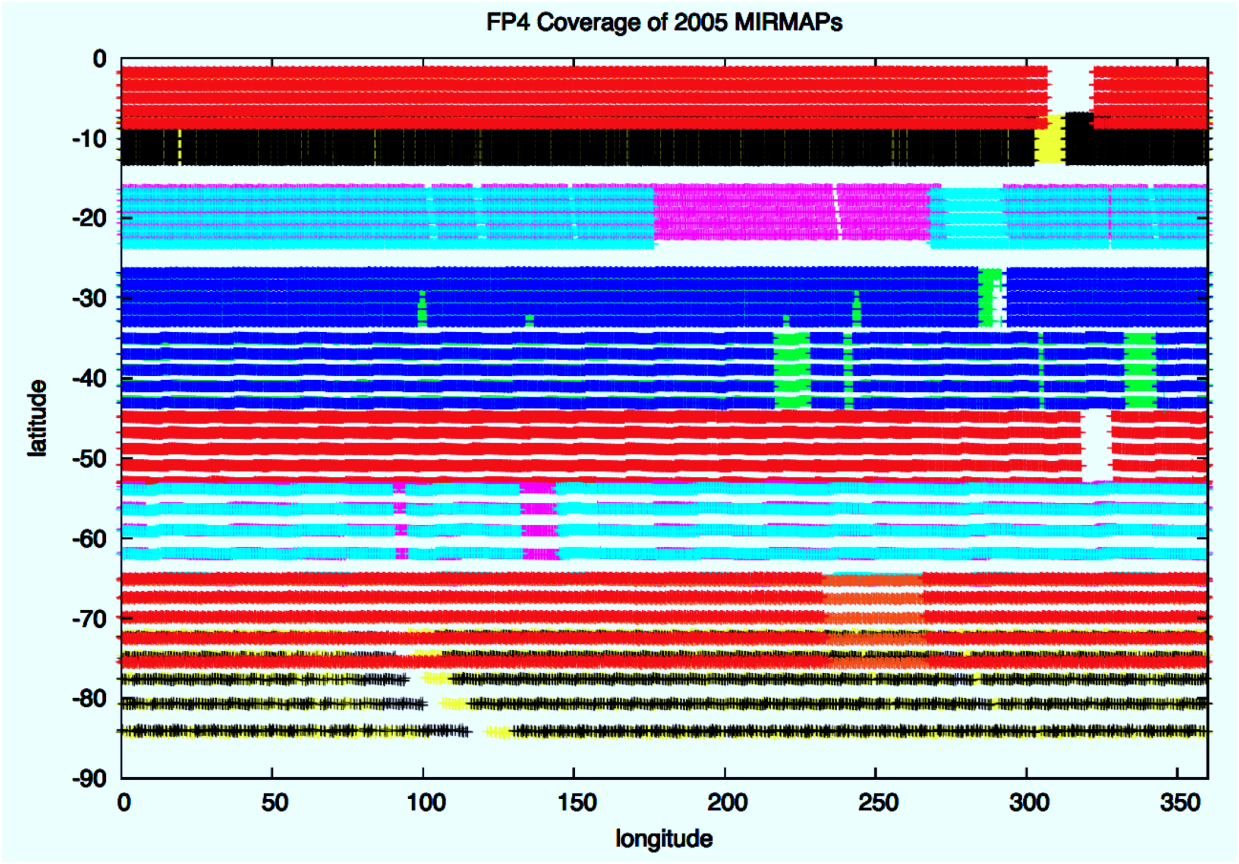

Figure 2-3. MIRMAP coverage in 2005. In each observation, the spacecraft scanned over a latitudinal band with 5 active detectors (shown as 5 horizontal lines with the same color). Lines centered at different latitudes but shown in the same color (for example, 5 horizontal red data lines centered at 70°S and 5 horizontal red data lines centered at 5°S) are from seperate observations measured at different sequences. In 2005, MIRMAP observations covered the latitudes between 0° and 85°S in the southern hemisphere on Saturn.

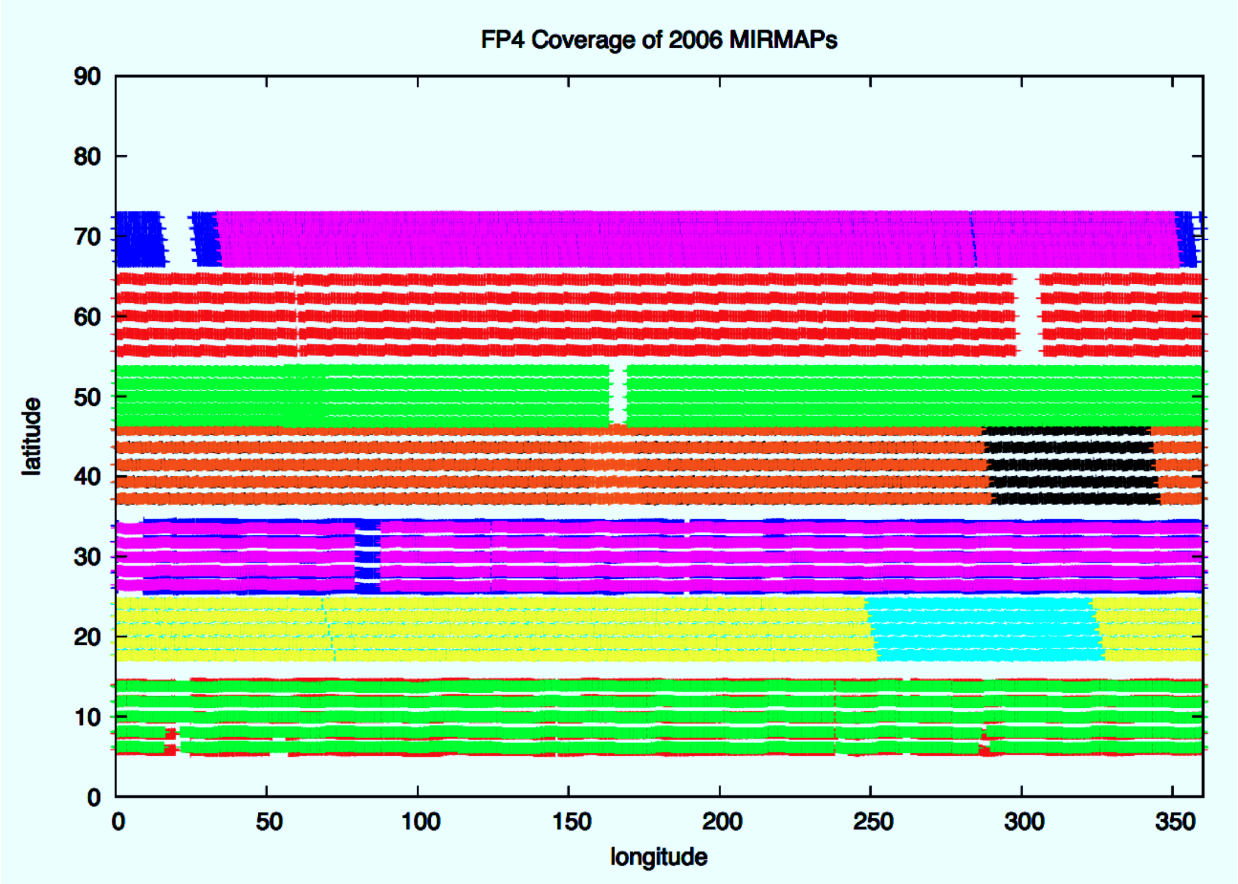

Figure 2-4. MIRMAP coverage in 2006. MIRMAP observations in 2006 covered Saturn's northern hemisphere at latitudes between 5°N and 73°N.

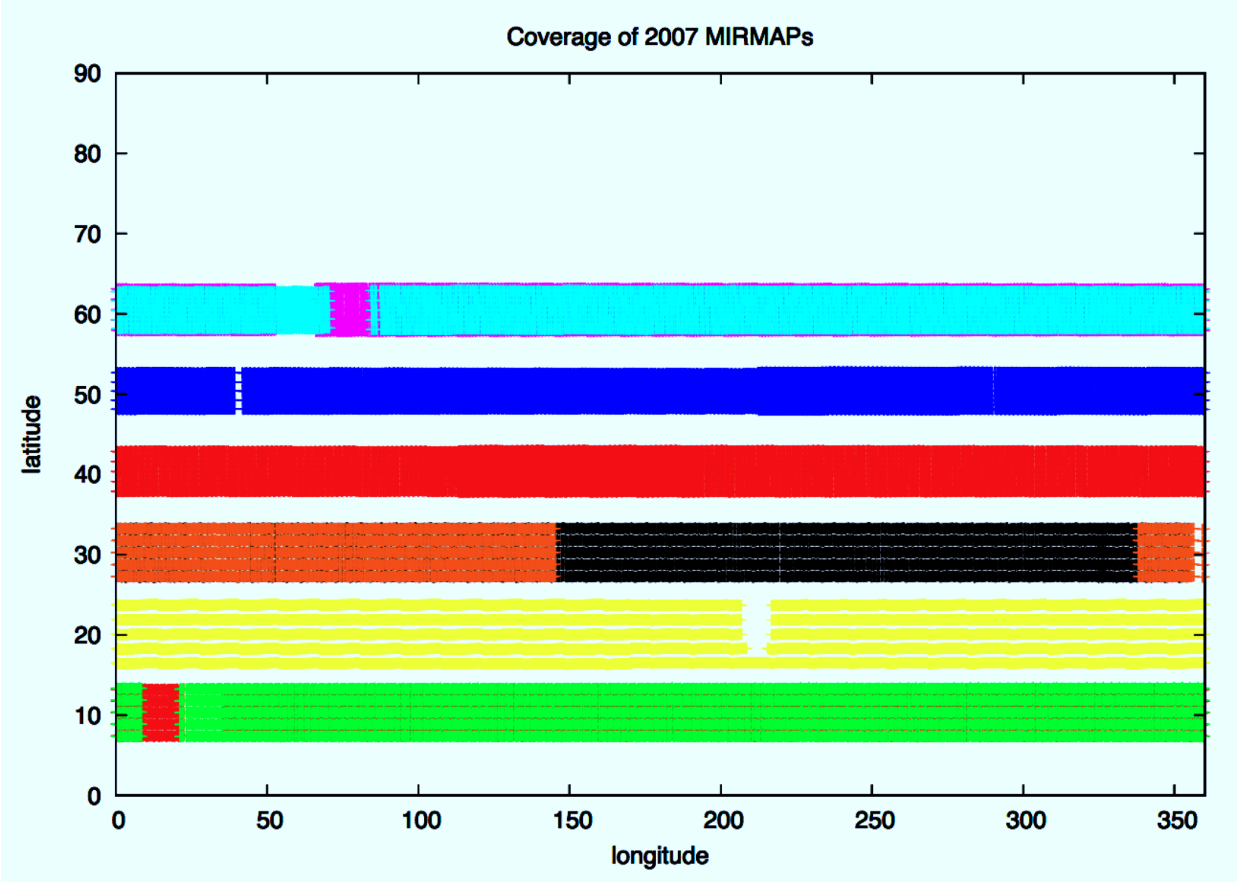

Figure 2-5. MIRMAP coverage of Saturn's northern hemisphere at latitudes between 8°N and 65°N in 2007.

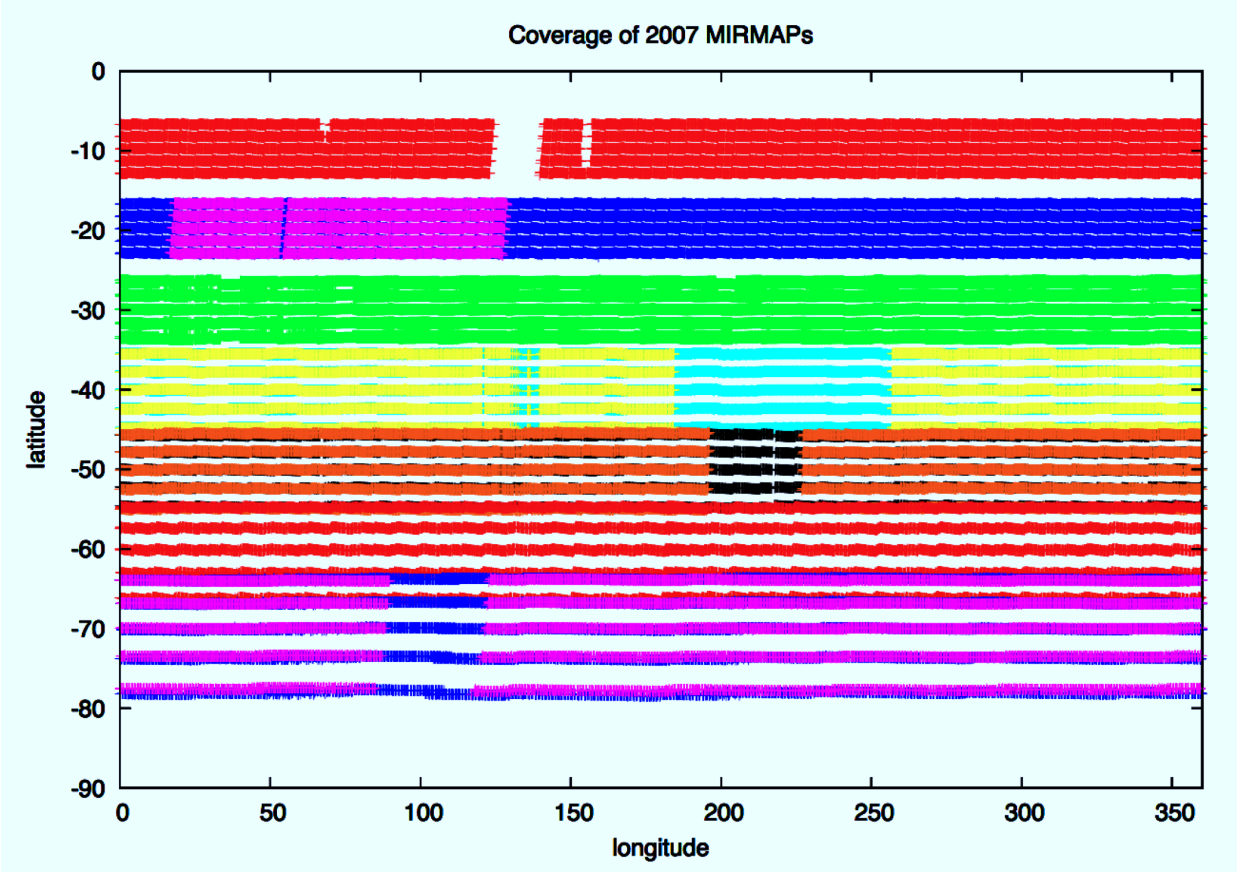

Figure 2-6. MIRMAP coverage of Saturn's southern hemisphere at latitudes between 7°S and 80°S in 2007.

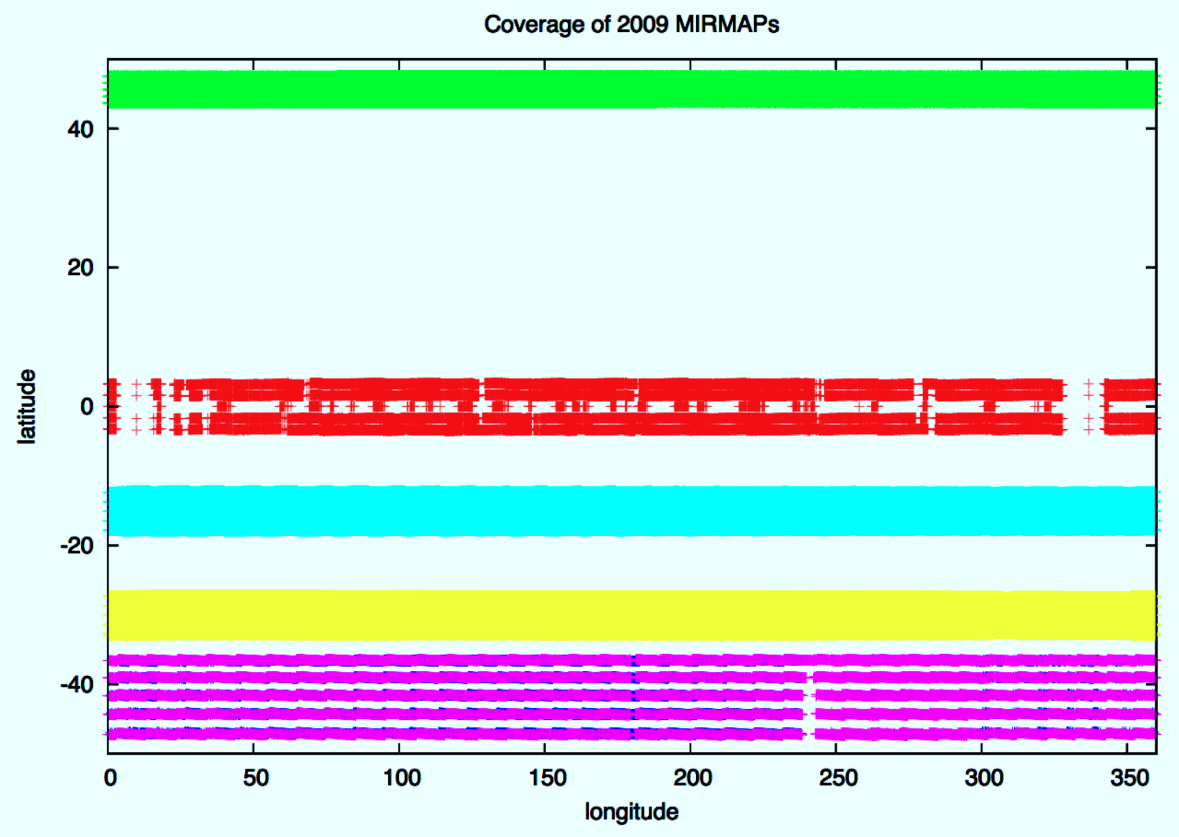

Figure 2-7. MIRMAP coverage in 2009. In 2009, the MIRMAP observations covered the equatorial region between 5°S and 5°N, and the latitudinal region between 10°S and 50°S.

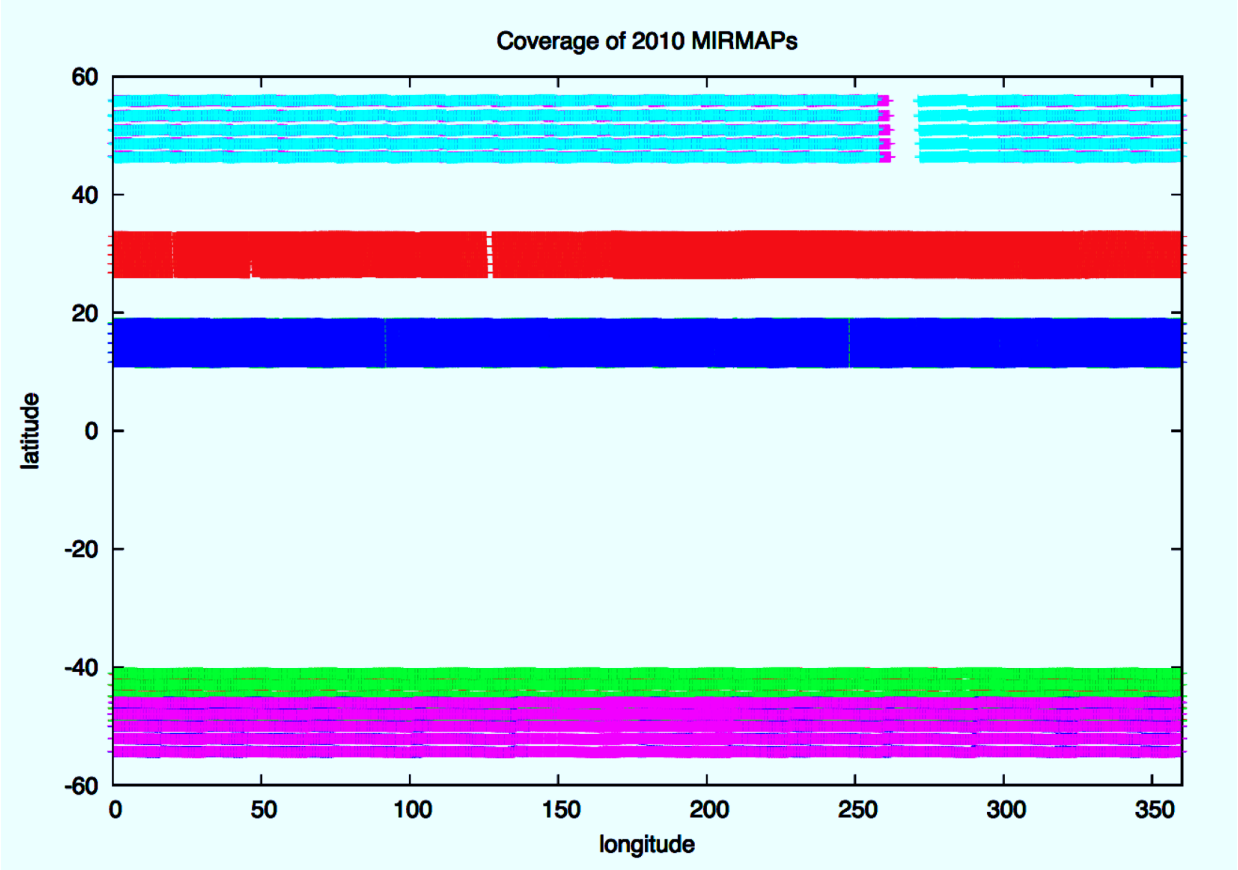

Figure 2-8. MIRMAP coverage in 2010.

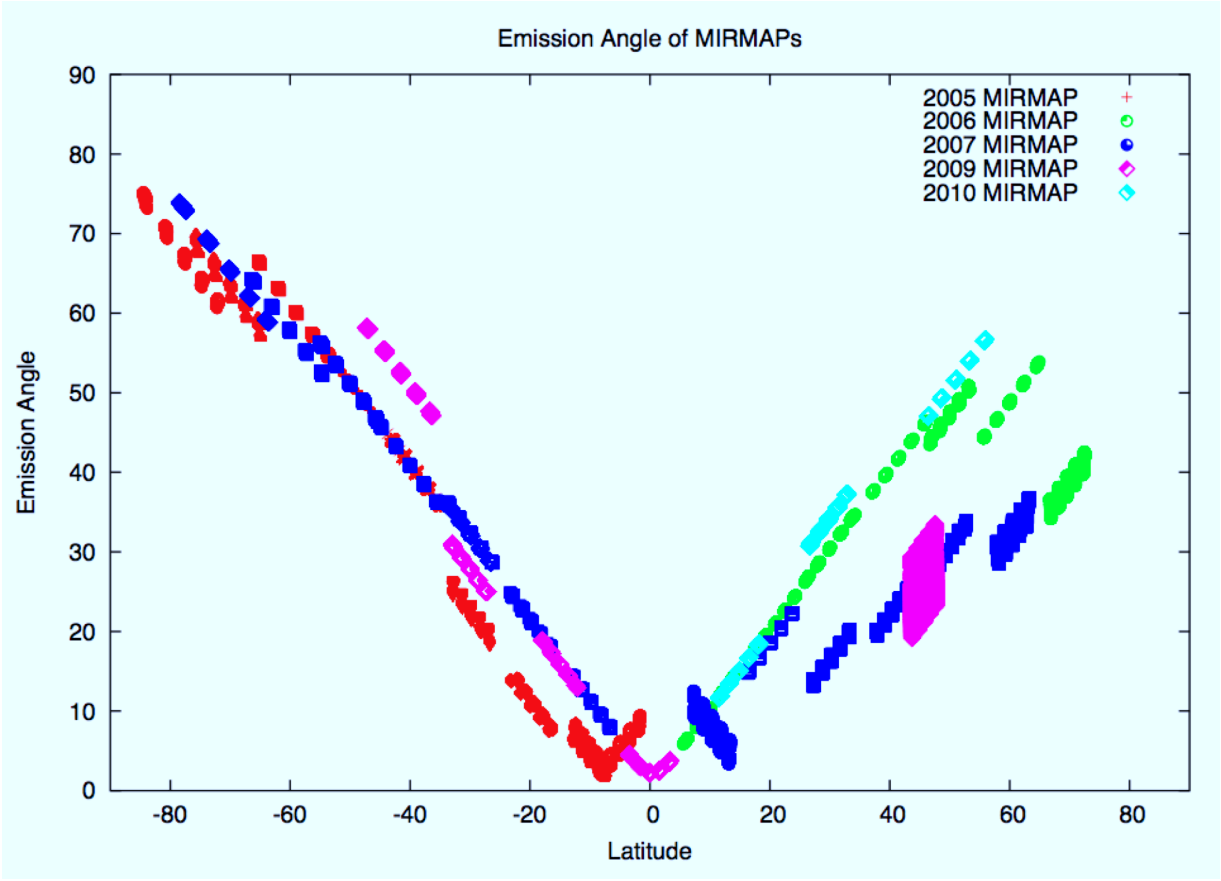

Figure 2-9. Emission angles of MIRMAP observations from 2005 to 2010. The Cassini spacecraft is near the equatorial region for MIRMAP observations, therefore, the emission angles increase with latitudes.

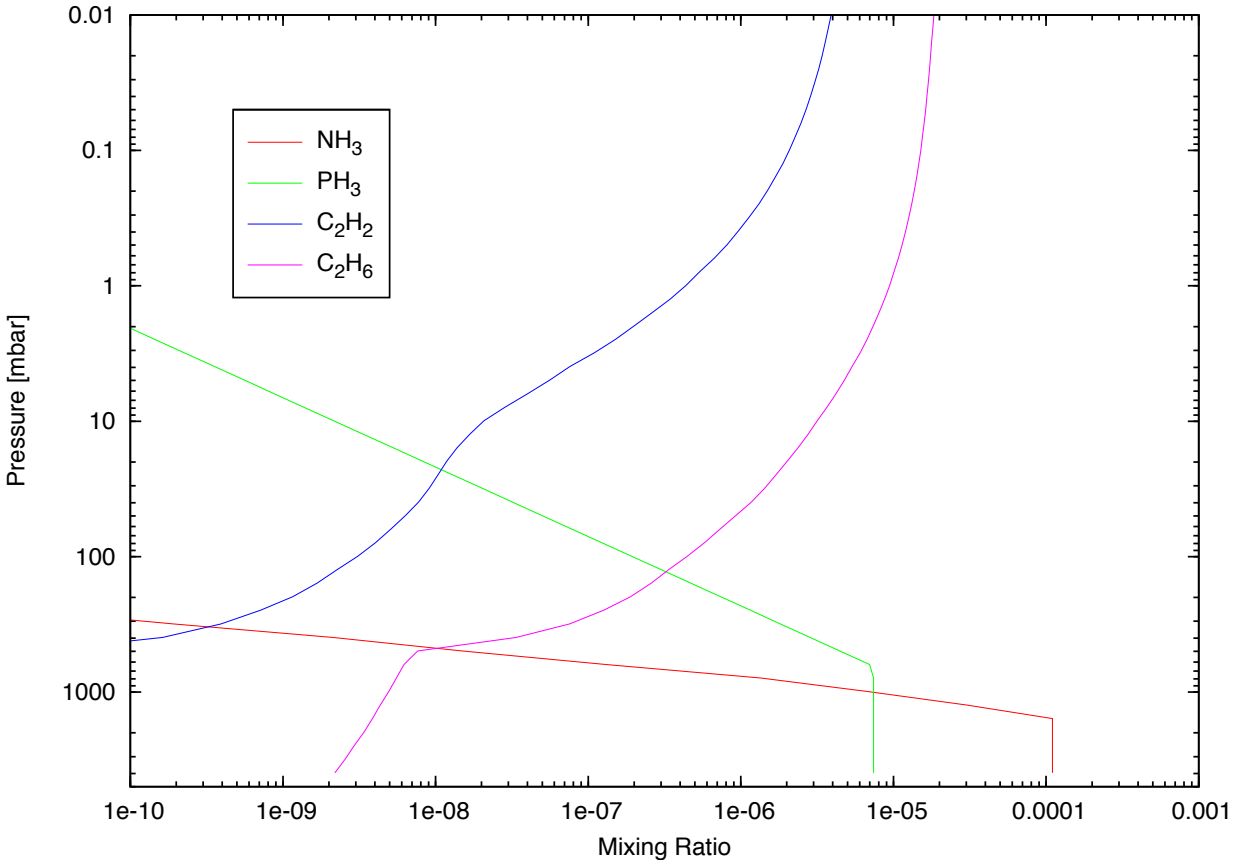

Figure 2-10. Reference atmospheric structure of Saturn. The volume mixing ratios of ethane and acetylene increase with height, based on the study by Moses and Greathouse (2005). The reference phosphine vertical profiles is based on rotational line observations by Orton et al. (2000; 2001). The vertical distribution of ammonia followed results by Courtin et al. (1984). Chemical constituents such as H_2O, GeH_4, CO, AsH_3, and CO_2 do not contribute much to the mid-infrared spectrum and were neglected from the reference model.

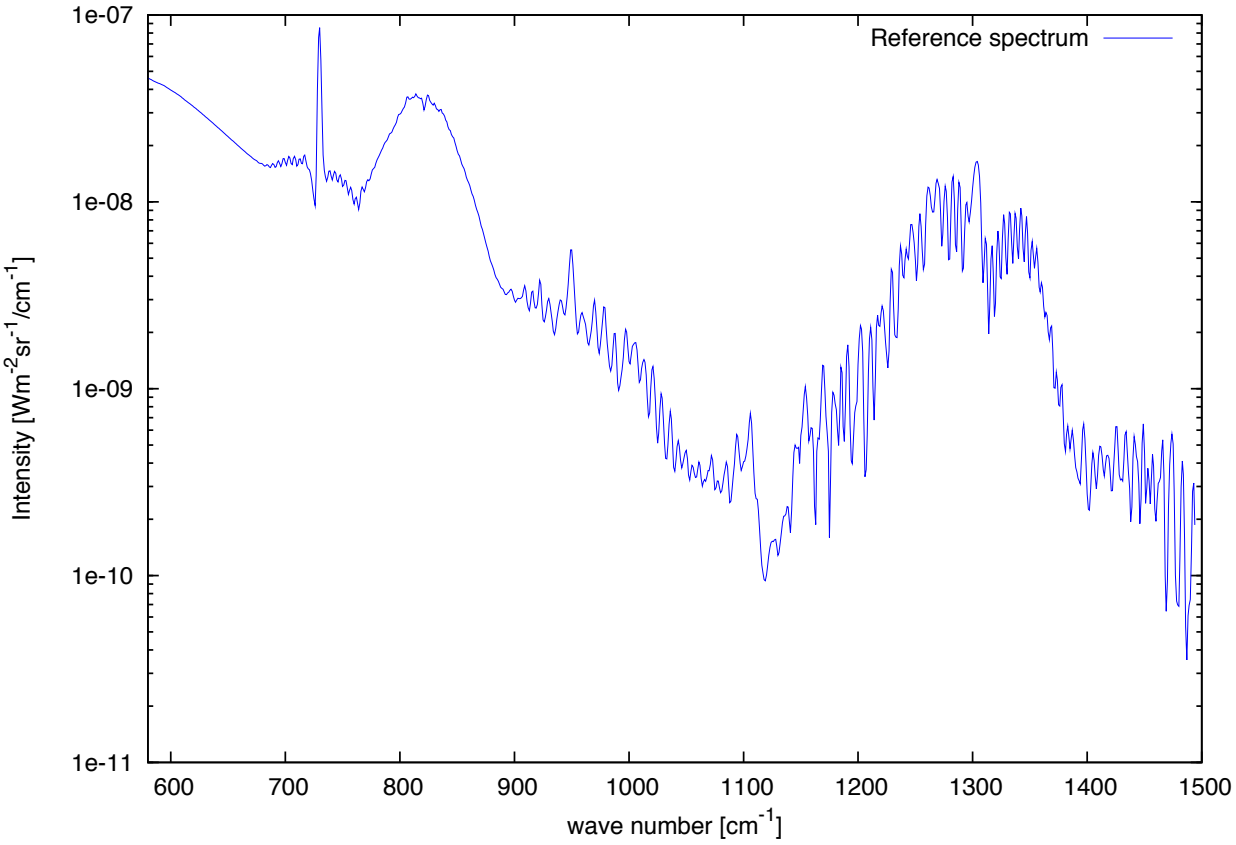

Figure 2-11. Synthesized spectrum based on the reference atmospheric structure. This figure shows the spectral features contributed by different atmospheric species. C_2H_2, C_2H_6 and CH_4 have strong emitting features at 625-825 cm^{-1}, 700-900 cm^{-1}, and 1150-1350 cm^{-1}, respectively. PH_3 and NH_3 appear in absorption relative to the background continuum between 900-1200 cm^{-1}.

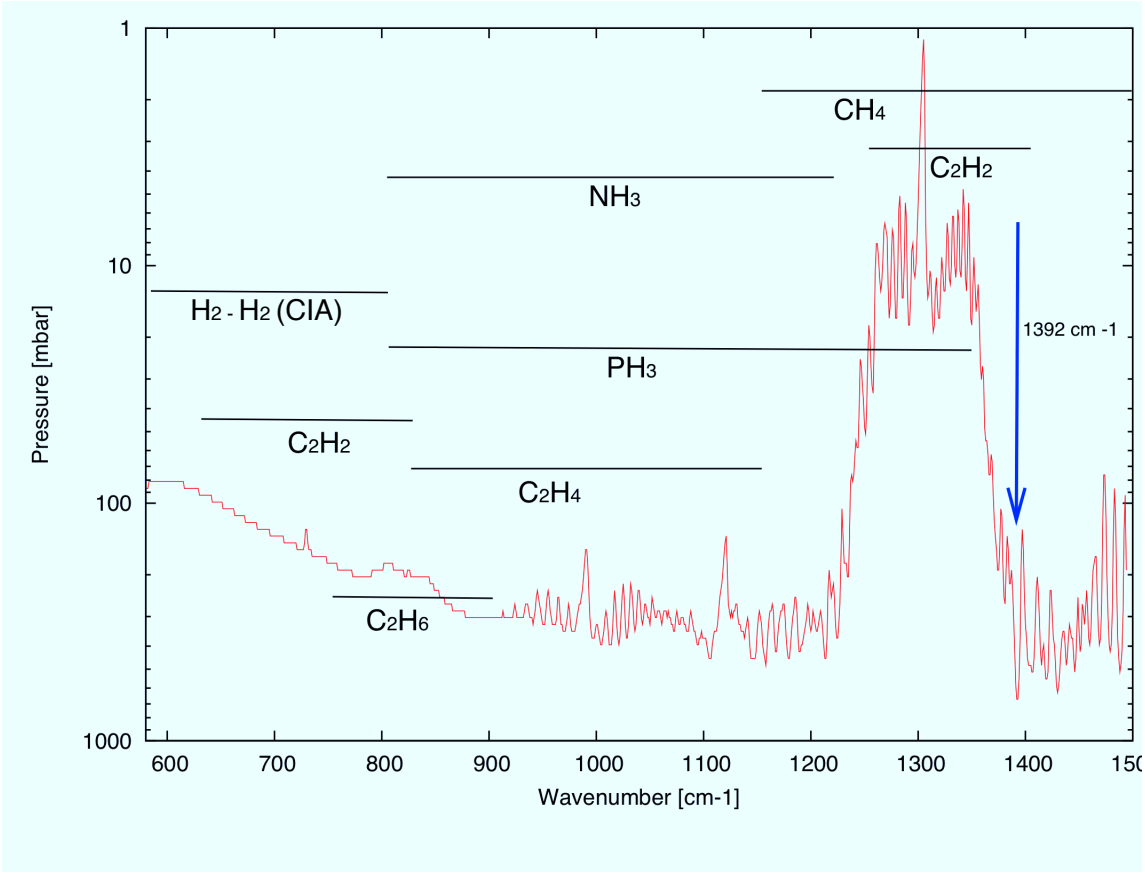

Figure 2-12. Pressure level of unity optical depth in nadir-viewing geometry. The atmospheric model assumes a clear atmosphere based on the reference atmospheric structure in Fig. 2-10. Horizontal lines indicate the spectral ranges contributed by the chemical constituents.

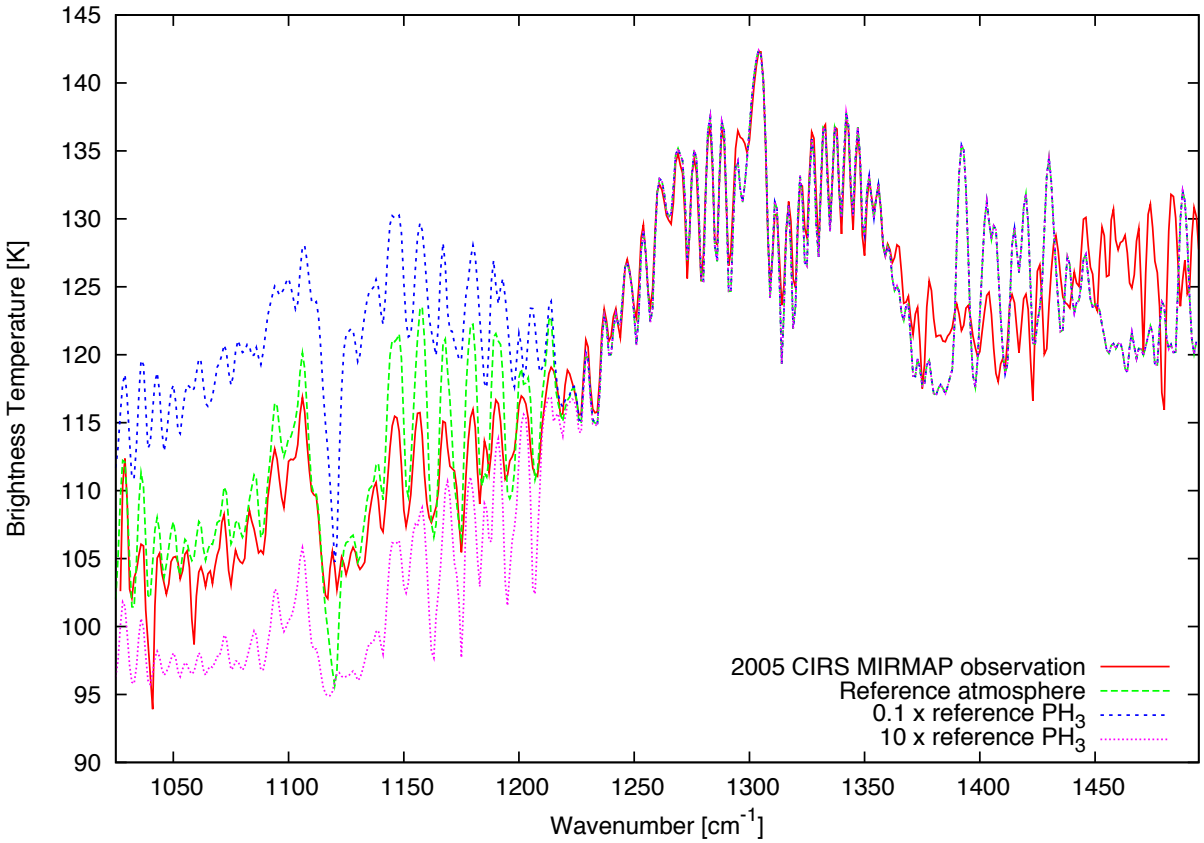

Figure 2-13. Sensitivity study to the abundance of phosphine.

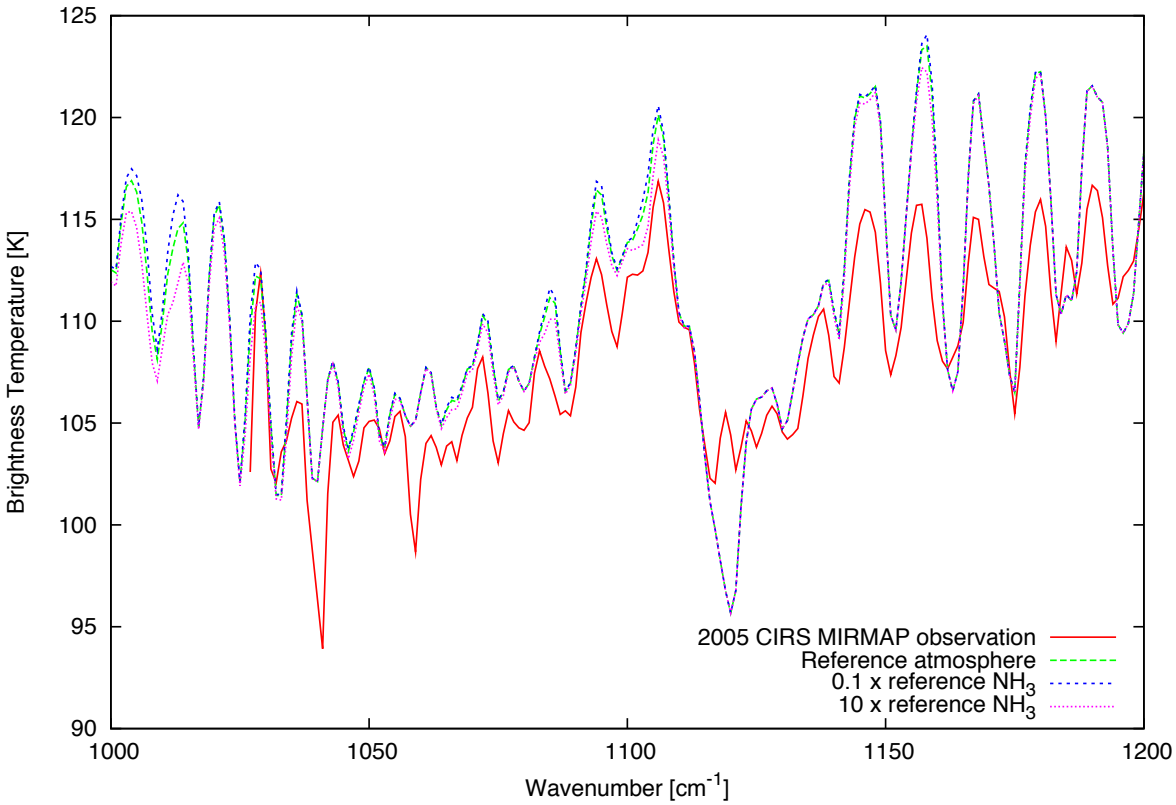

Figure 2-14. Sensitivity study to the abundance of ammonia. (1000 - 1200 cm^{-1})

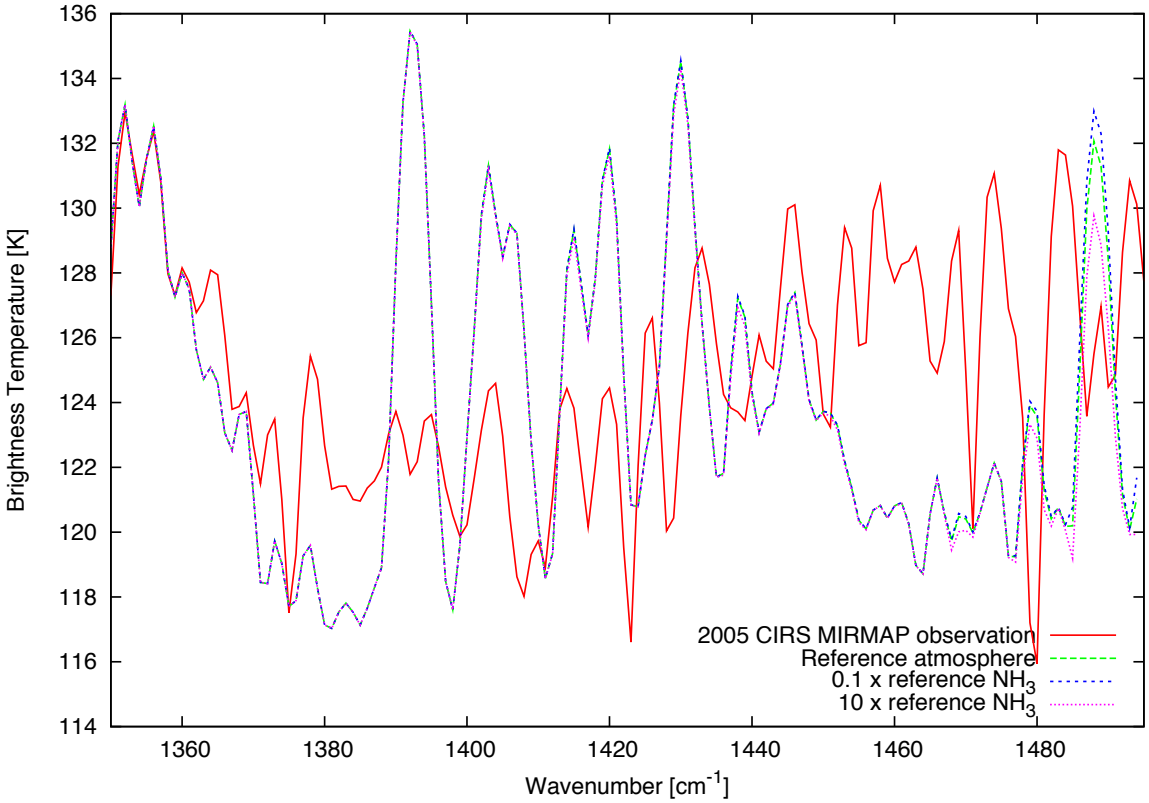

Figure 2-15. Sensitivity study to the abundance of ammonia. (1350 - 1490 cm^{-1})

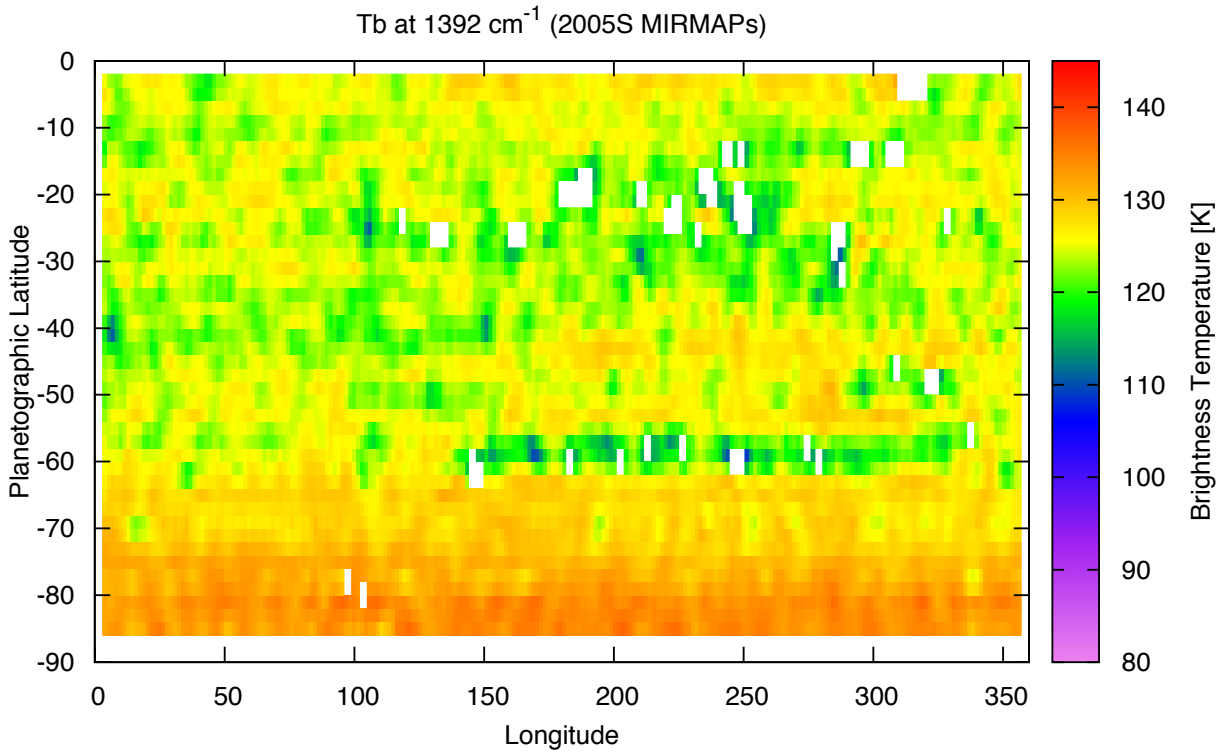

Figure 2-16. Brightness temperature map at 1392 cm^{-1} from 2005 MIRMAP observations in the southern hemisphere.

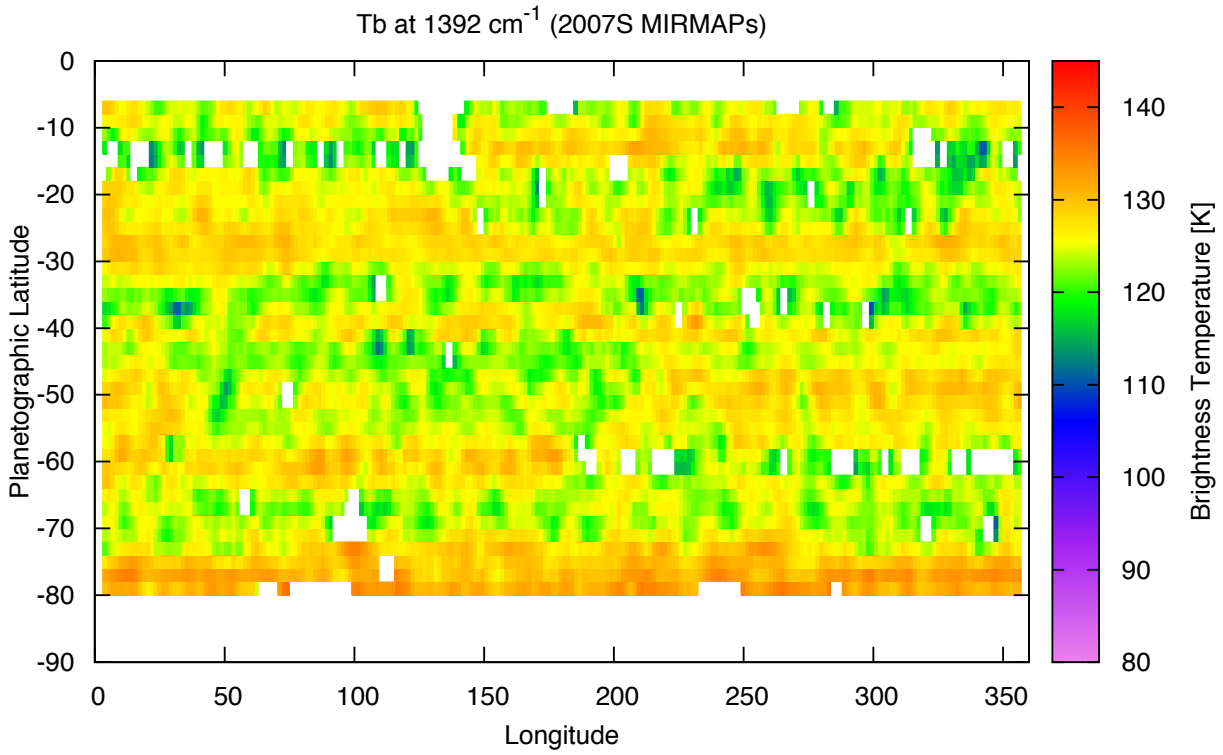

Figure 2-17. Brightness temperature map at 1392 cm^{-1} from 2007 MIRMAP observations in the southern hemisphere.

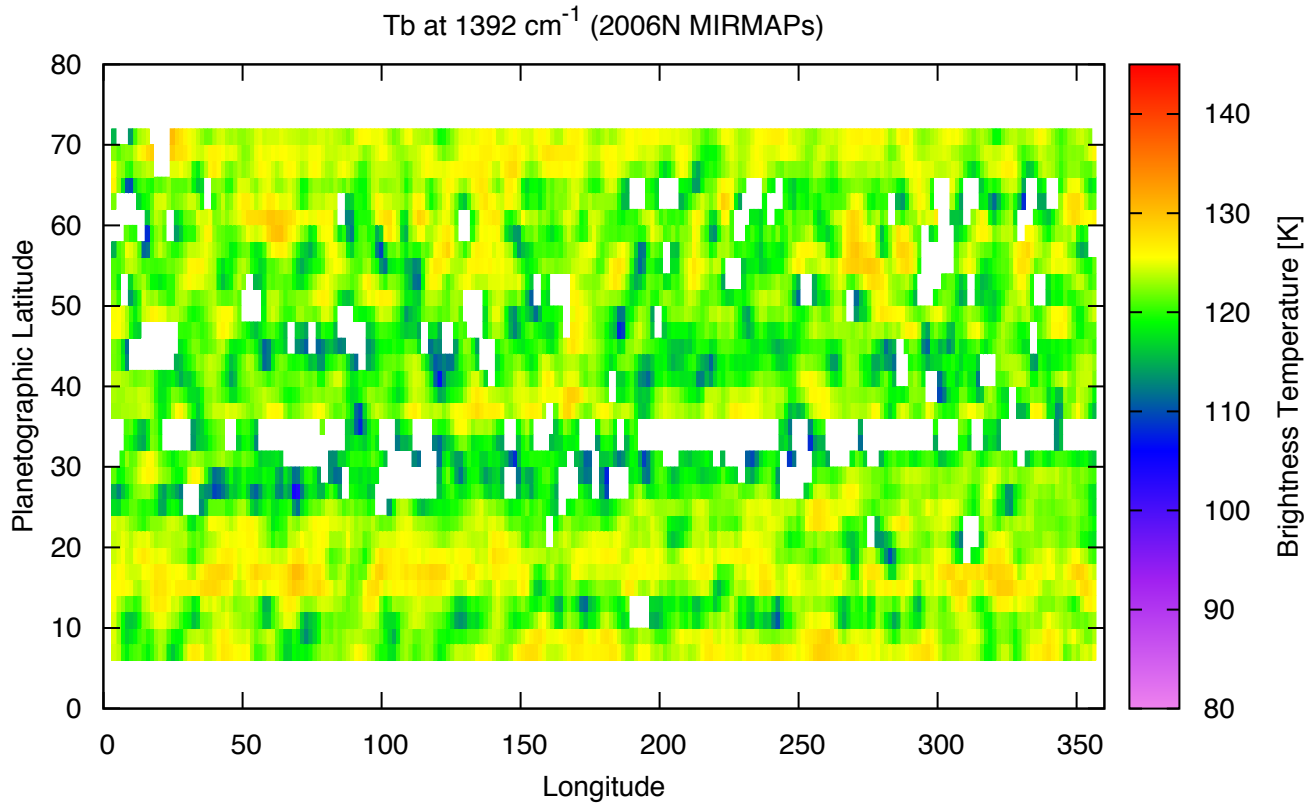

Figure 2-18. Brightness temperature map at 1392 cm^{-1} from 2006 MIRMAP observations in the northern hemisphere.

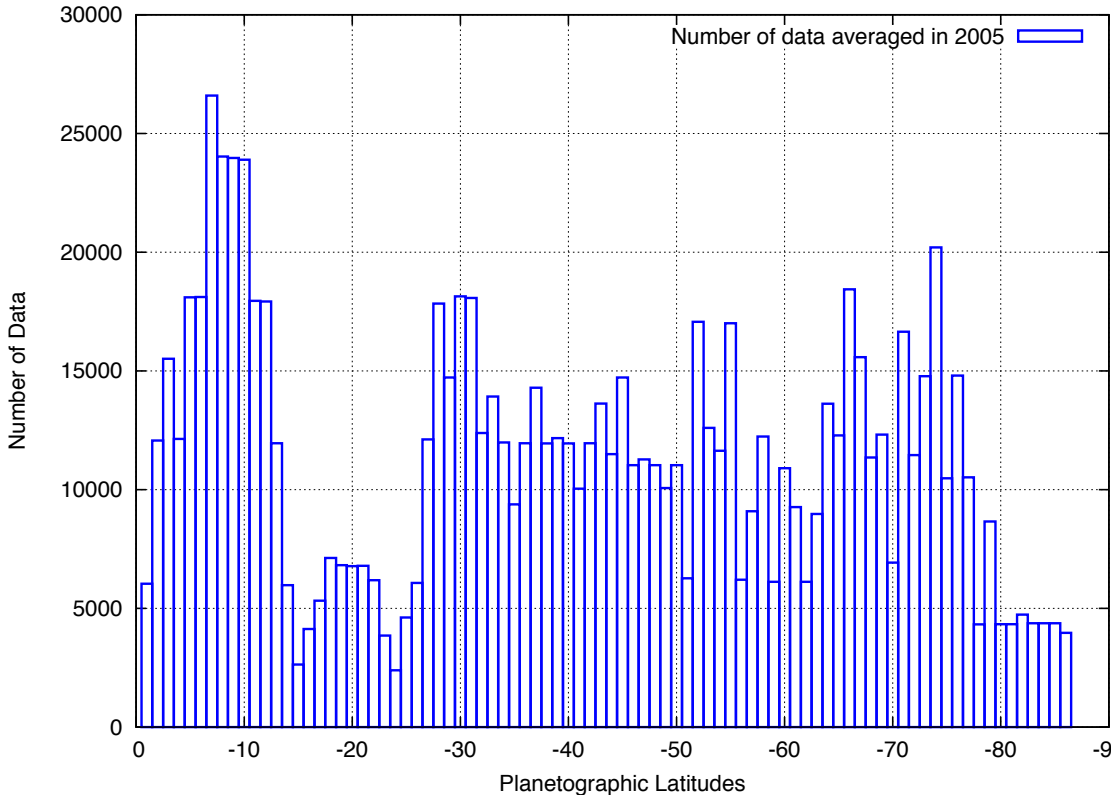

Figure 2-19. Number of radiances at 1392 cm^{-1} averaged for brightness temperature calculation in 2005.

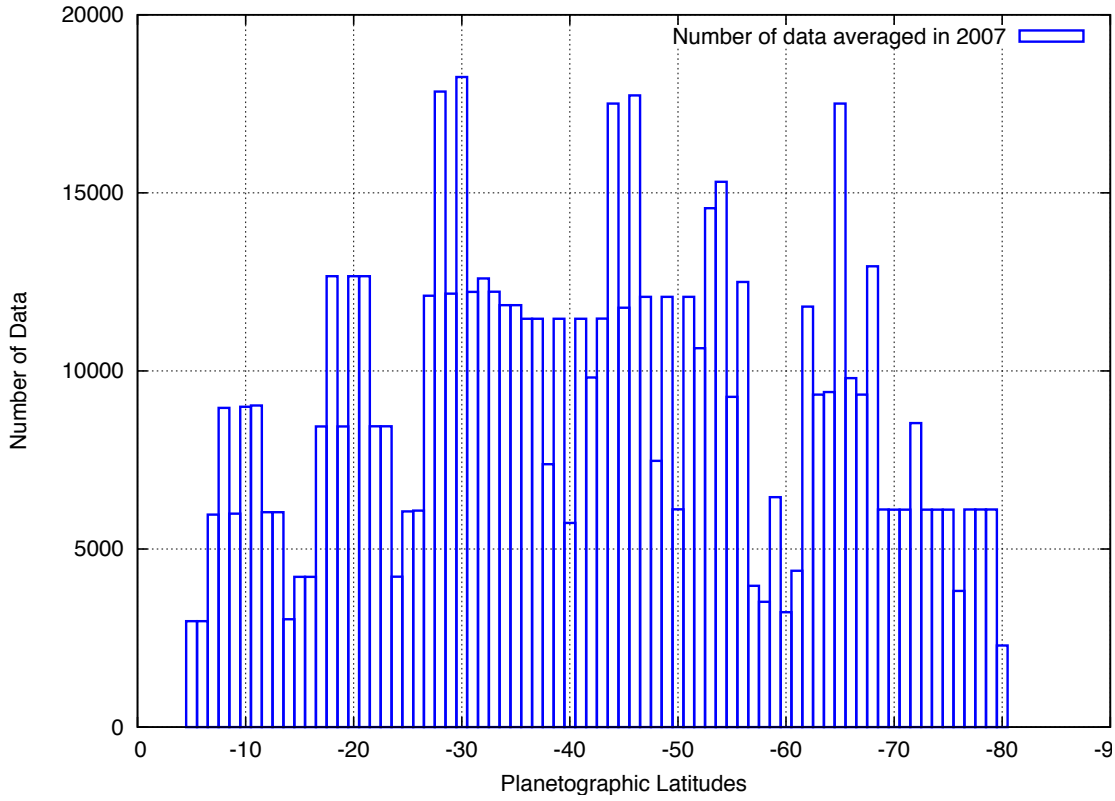

Figure 2-20. Number of radiances at 1392 cm^{-1} averaged for brightness temperature calculation in 2007.

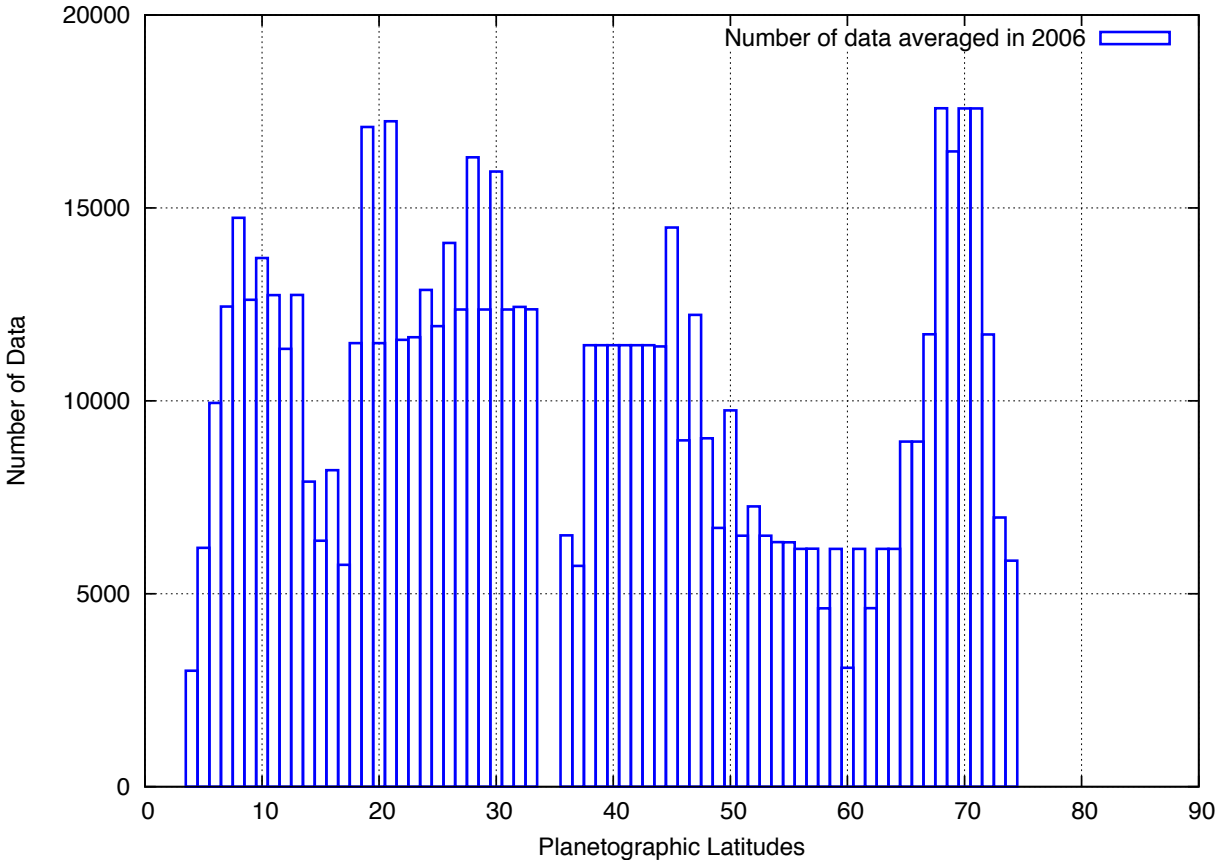

Figure 2-21. Number of radiances at 1392 cm^{-1} averaged for brightness temperature calculation in 2006.

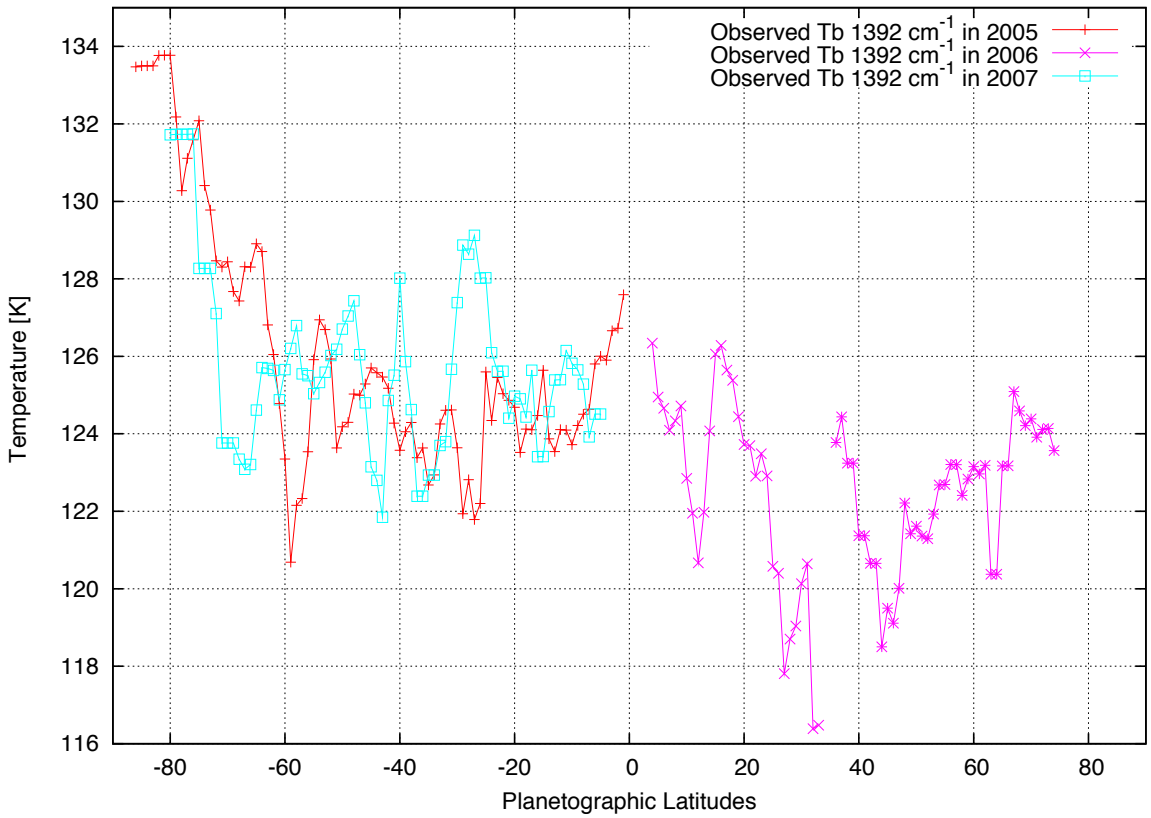

Figure 2-22. Zonal mean brightness temperature at 1392 cm^{-1} from 2005 to 2007.

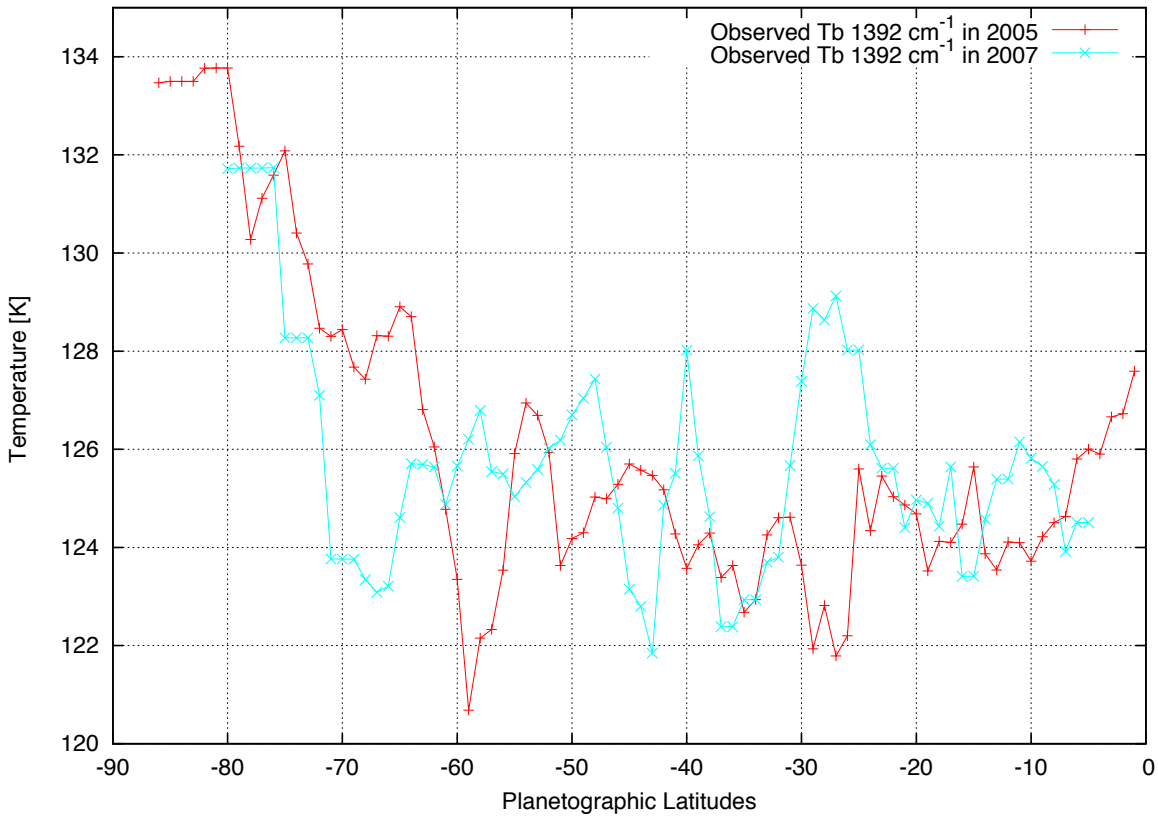

Figure 2-23. Zonal mean brightness temperature at 1392 cm^{-1} of the southern hemisphere in 2005 and 2007.

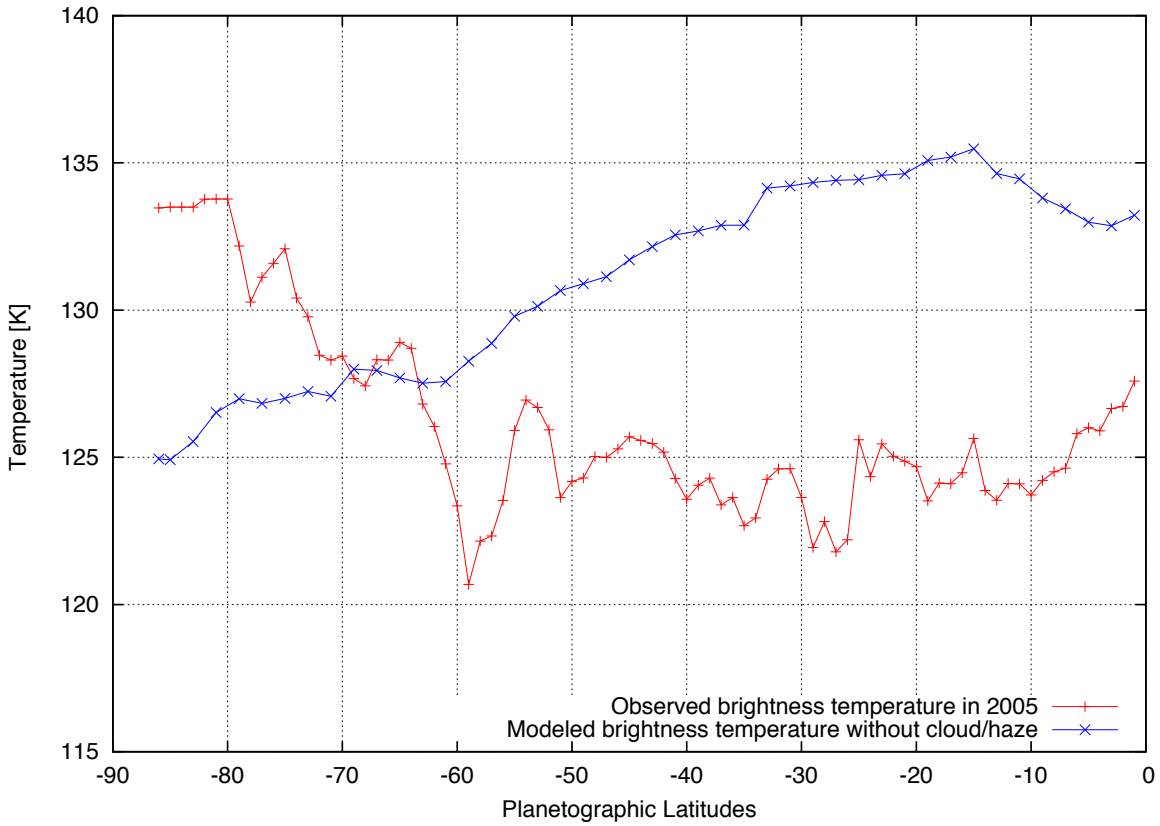

Figure 2-24. Zonal mean brightness temperature at 1392 cm^{-1} in 2005 compared with the modeled brightness temperature retrieved from the reference atmosphere without clouds and hazes. The modeled brightness temperature (blue line) decreases with increasing emission angles at higher latitudes.

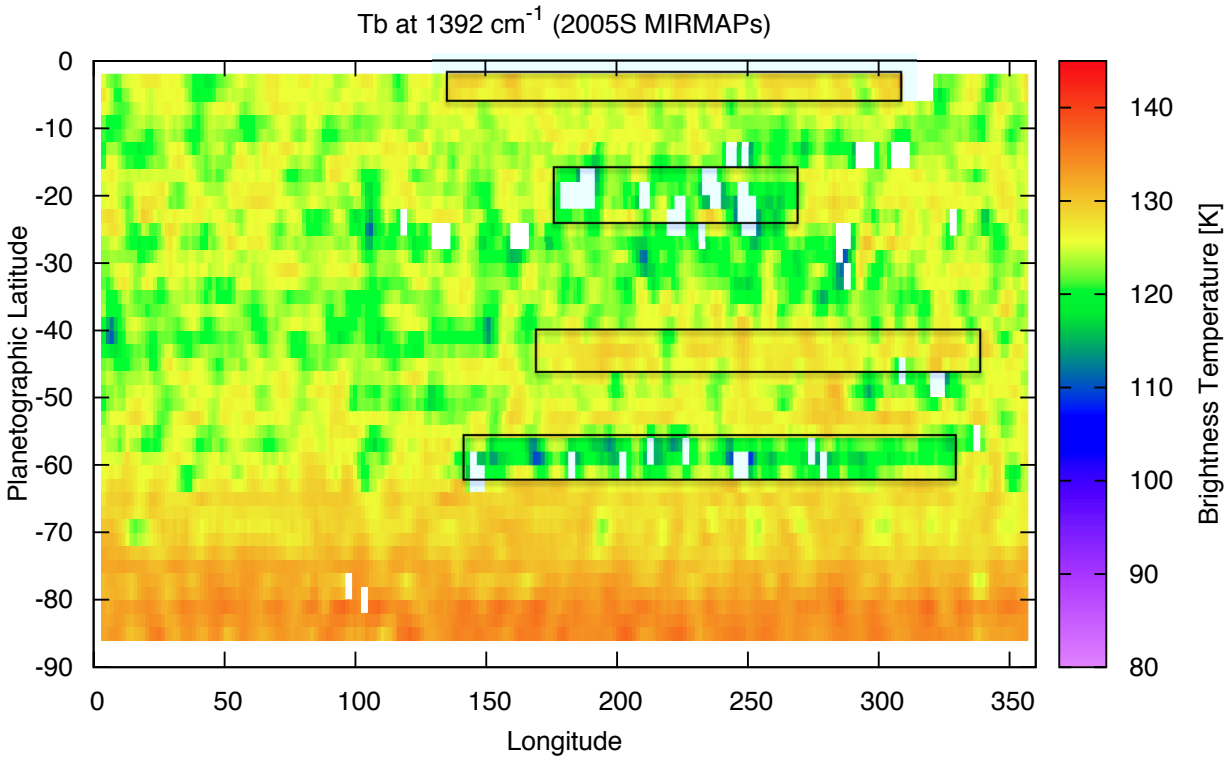

Figure 2-25. Brightness temperature map at 1392 cm^{-1} from 2005 MIRMAP observations in the southern hemisphere. Rectangular boxes label the discontinuity regions of the brightness temperature at 1392 cm^{-1}.

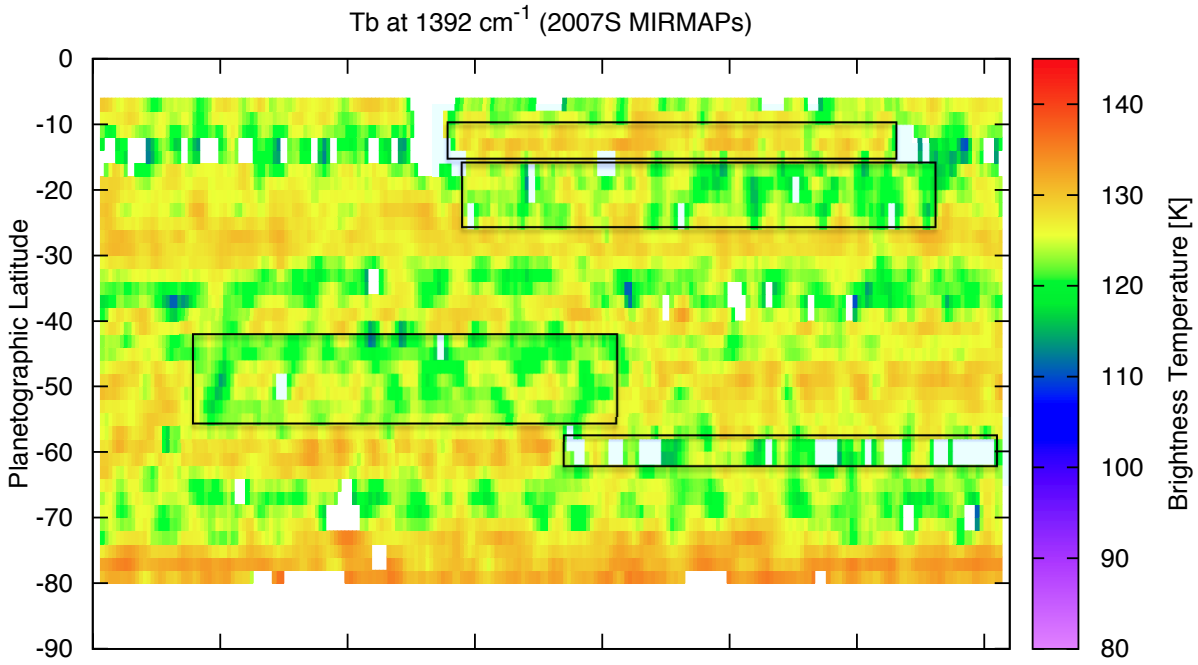

Figure 2-26. Brightness temperature map at 1392 cm^{-1} from 2007 MIRMAP observations in the southern hemisphere. Rectangular boxes label the regions of discontinuity of the brightness temperature at 1392 cm^{-1}.

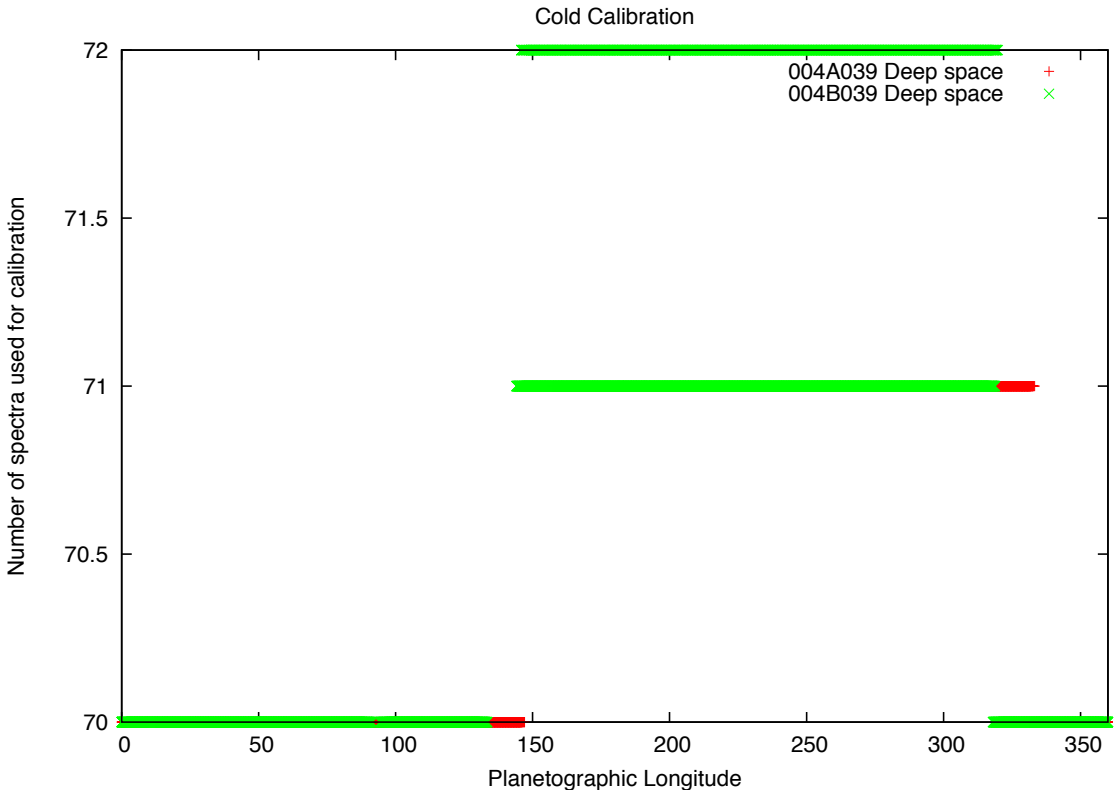

Figure 2-27. Number of spectra used in MIRMAP observations at 60°S in 2005 for cold calibration (Deep Space).

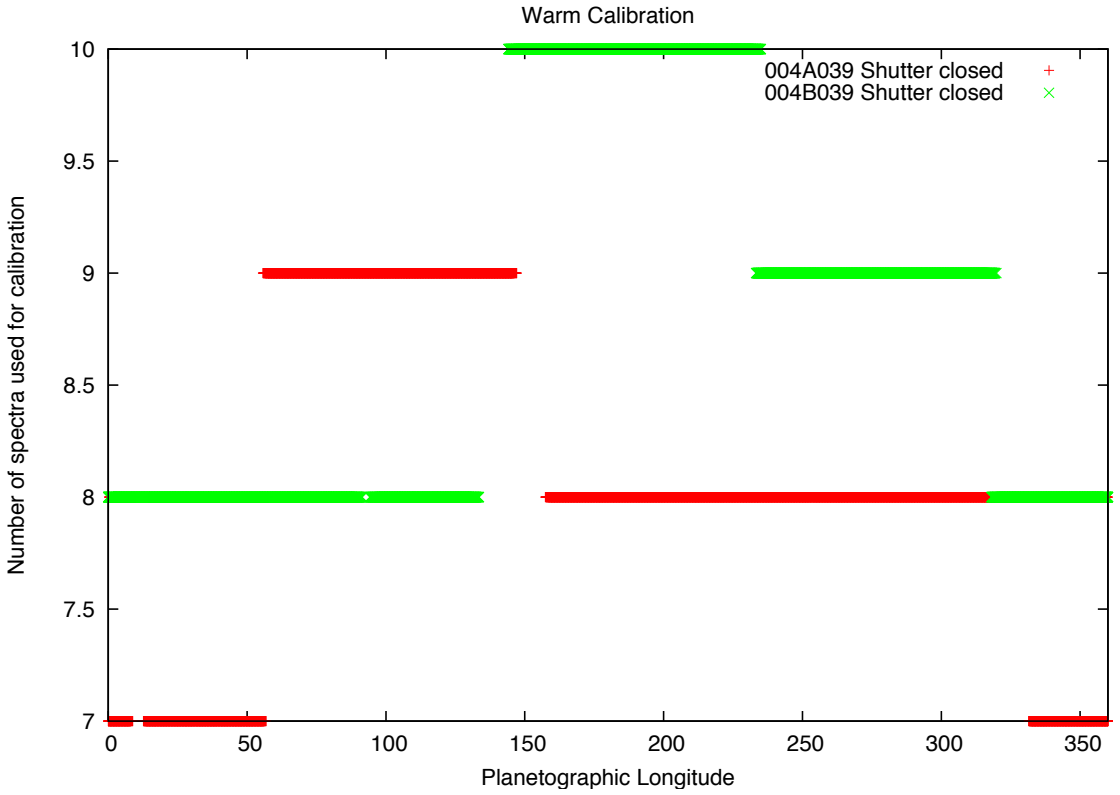

Figure 2-28. Number of spectra used in MIRMAP observations at 60°S in 2005 for warm calibration (Shutter closed).

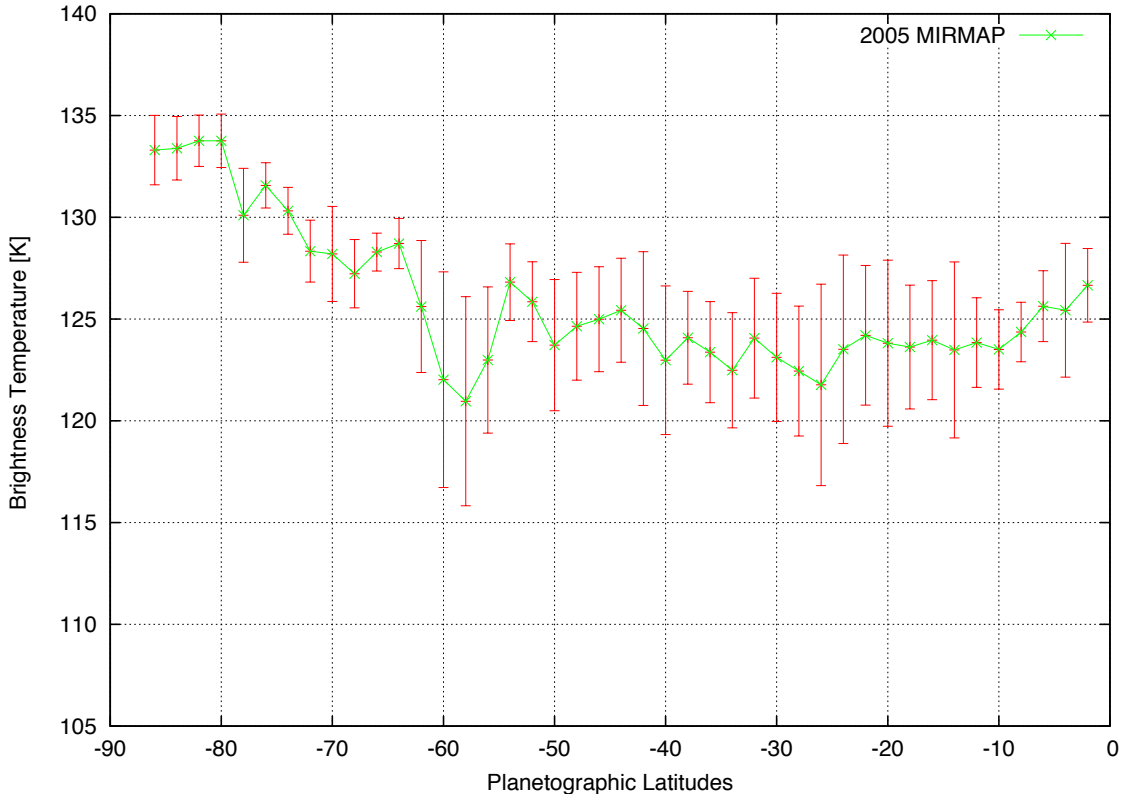

Figure 2-29. Variances of the zonal mean brightness temperature of the southern hemisphere in 2005.

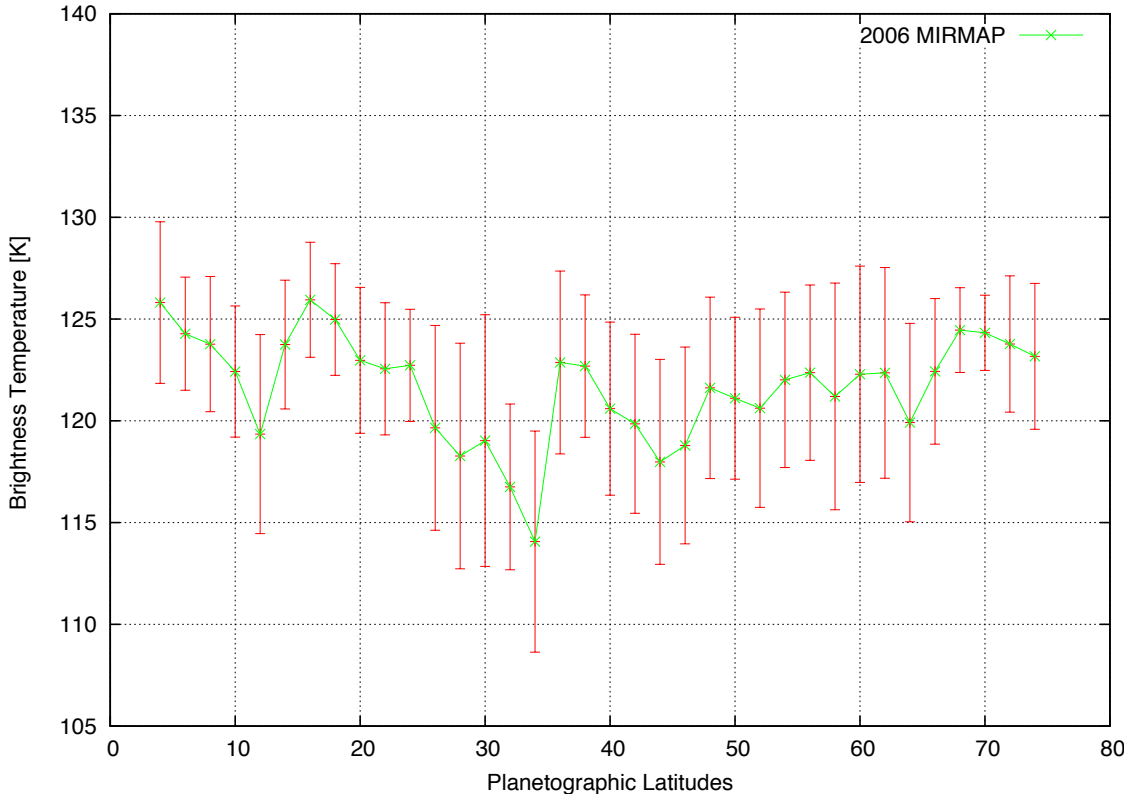

Figure 2-30. Variances of the zonal mean brightness temperature of the northern hemisphere in 2006.

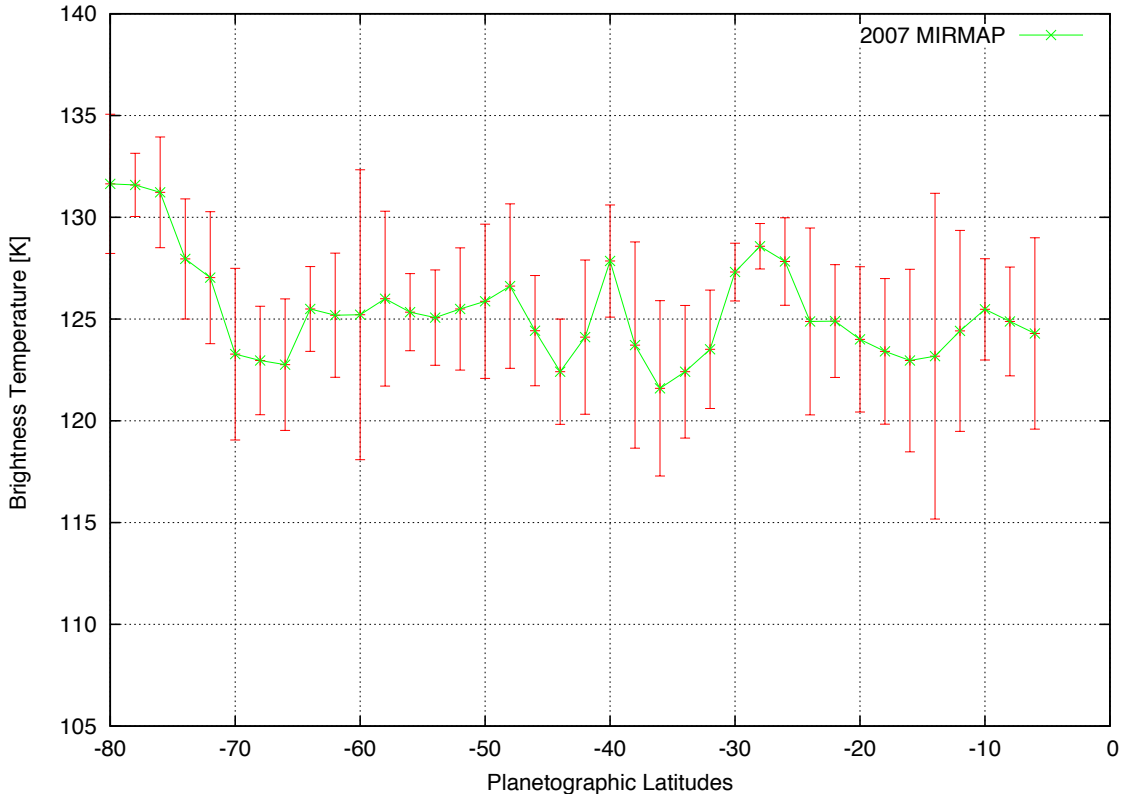

Figure 2-31. Variances of the zonal mean brightness temperature of the southern hemisphere in 2007.

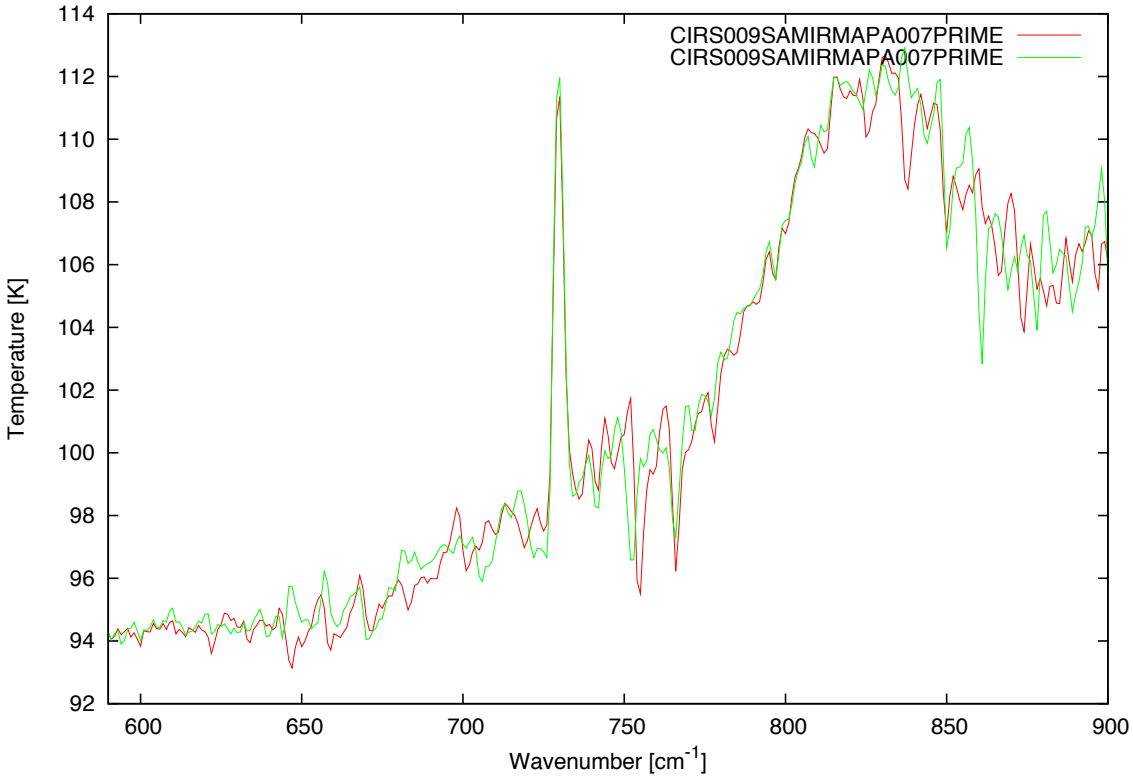

Figure 2-32. Spectra of the MIRMAP observations 009A007 and 009B007 in FP3 spectral range.

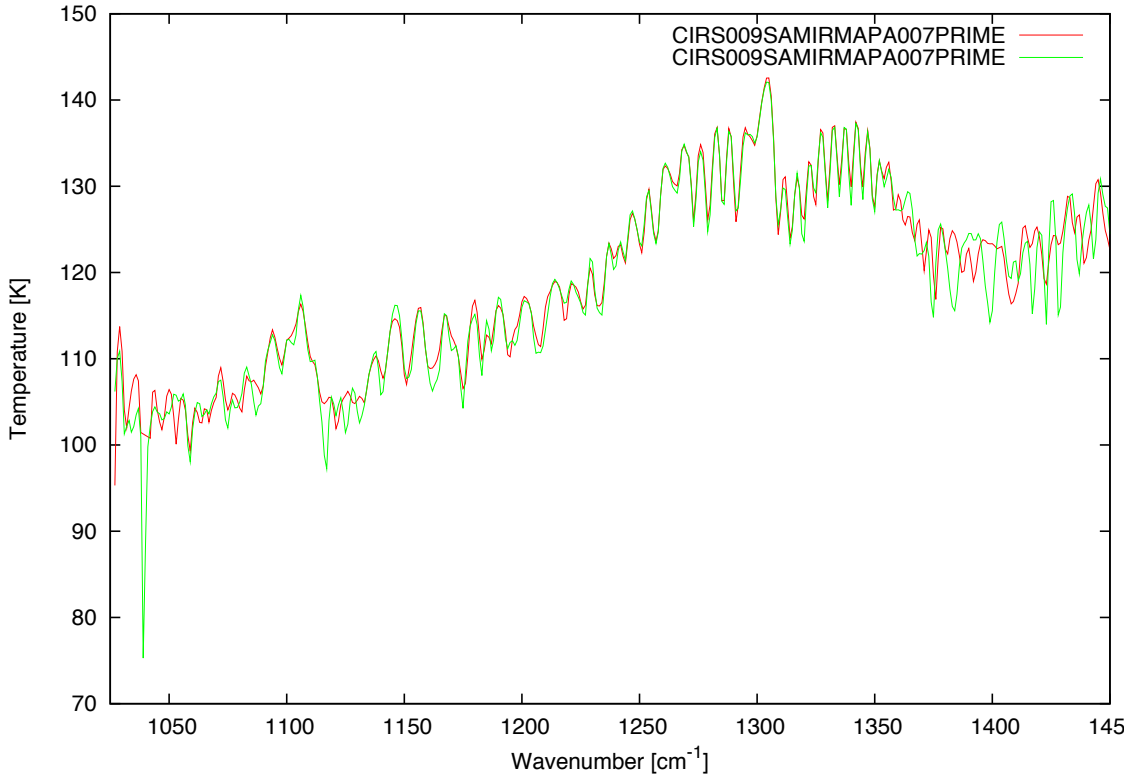

Figure 2-33. Spectra of the MIRMAP observations 009A007 and 009B007 in FP4 spectral range.

CHAPTER 3
RETRIEVAL ALGORITHM AND NUMERICAL MODEL

3.1 Introduction

For satellite-based remote sounding observations, we need to rely on inverse methods to retrieve the atmospheric properties because the desired physical quantities are not typically directly measurable. To obtain the vertical distribution of Saturn's atmospheric properties, such as temperature and clouds/haze profiles, we first acquire infrared spectra from the Cassini Orbiter with remote sounding techniques. We then compare the observed spectrum with a synthetic one generated by a forward model with initial physical parameters. New synthetic spectra will be generated with different sets of varying physical parameters, and the retrieved atmospheric profiles will be provided by the parameters that best fit synthetic spectra. A schematic diagram of the retrieval process is shown in Fig. 3-1. A detailed description of the forward model and the retrieval algorithm will be discussed in the following sections.

3.2 Forward Model

The forward model is the key component which converts physical parameters to spectrum in the retrieval algorithm. This model not only has to include all the relevant physics, but it must also be numerically efficient to reduce the computing time.

In a non-scattering homogeneous atmosphere, the mean radiance $I(\nu)$ emitted to space between frequencies ν and $\Delta\nu$ can be calculated as

$$I(\nu) = \bar{B}_\nu(T_0)\,\bar{T}_{r,\nu}(0) + \int_0^\infty \bar{B}_\nu(T(z))\frac{\mathrm{d}\,\bar{T}_{r,\nu}(z)}{\mathrm{d}z}\mathrm{d}z, \tag{3–1}$$

where $\bar{T}_{r,\nu}(z)$ is the mean transmittance from the altitude z to space at frequency ν, $\bar{B}_\nu(T(z))$ is the mean Planck radiance at temperature T, and T_0 is the temperature at a reference height. For rocky planets, the reference height is the ground; for gas giants, it is usually the 1-bar pressure level. The mean transmittance $\bar{T}_{r,\nu}$ between the frequency

interval ν and $\nu + \Delta\nu$ can be calculated as

$$\bar{T}_r(m) = \frac{1}{\Delta\nu} \int_{\nu}^{\nu+\Delta\nu} \exp\left(-m \sum_j k_j(\nu')\right) \mathrm{d}\nu', \tag{3–2}$$

where m is the total absorber amount, and k_j is the absorption coefficient of the jth line.

To calculate the synthetic spectrum from Eq. 3–1 and 3–2, a line-by-line model, which computes the absorption of each individual spectral line, is considered the most accurate forward model. Line data are provided from the standard line databases, such as HITRAN (Rothman et al., 2005) or GEISA (Jacquinet-Husson et al., 2005). The individual absorptions need to be calculated for the different pressures and temperatures (Irwin et al., 2008). The spectral ranges of interest are usually large, and the required spectral resolution for Eq. 3–2 to resolve the individual line shapes is much smaller than the spectral interval $\Delta\nu$, which results in substantial amount of computing time. Therefore, the line-by-line model is unrealistic for retrieval purposes.

To balance between efficiency and accuracy, a correlated-k method (Goody et al., 1989; Lacis and Oinas, 1991; Liou, 2002) is used as a forward model in our work. With the correlated-k method, we can calculate the mean transmittance based on grouping the absorption coefficients k_ν instead of integrating over the frequency intervals to save computing time.

The mean transmittance in a non-scattering homogeneous atmosphere is not dependent on the order of the absorption coefficients for a given spectral range. We can rewrite Eq. 3–2 as the integration over the k space with the fraction $f(k)$ of the frequency domain. The new mean transmittance equation, therefore, becomes

$$\bar{T}_r(m) = \int_0^{\infty} f(k) \exp(-km) \mathrm{d}k. \tag{3–3}$$

Furthermore, if we define a smooth single-value cumulative function $g(k)$ as

$$g(k) = \int_0^{k} f(k') \mathrm{d}k', \tag{3–4}$$

which increases monotonically in k space, then Eq. 3–3 can be rewritten as

$$\bar{T}_r(m) = \int_0^1 \exp(-k(g)m)\mathrm{d}g, \tag{3–5}$$

where $k(g)$ is called the k-distribution function. $k(g)$ is the inverse function of $g(k)$, and it is a smooth function in g space.

Comparing Eq. 3–2 with Eq. 3–5, we can see that Eq. 3–2 requires a small frequency interval $\mathrm{d}\nu$ in a numerical integration to acquire optimal resolution because $k(\nu)$ is a rapidly changing function of ν; Eq. 3–5 uses fewer steps and larger interval $\mathrm{d}g$ because $k(g)$ is a slowly increasing function. Therefore, by integrating over the g-space, we can save numerical computing time by using the correlated-k method for the forward model.

For computational purposes, we need to approximate Eq. 3–5 by discretizing it as

$$\bar{T}_r(m) = \sum_{i=1}^{N} \exp(-k_i m)\Delta g_i, \tag{3–6}$$

where N is 20 in our work to balance the computational speed and the accurate sampling of the k-distribution. k_i is the k-distribution value at the ith point and Δg_i is the corresponding weight. However, a real atmosphere is not homogeneous because the temperature and pressure vary with height. We can treat the real inhomogeneous atmosphere as several stacked homogeneous layers. The mean transmittance along the path through M layers can be written as

$$\bar{T}_r(m) = \sum_{i=1}^{N} \exp\left(-\sum_{j=1}^{M} k_{ij} m_j\right) \Delta g_i. \tag{3–7}$$

As a result, the discretized mean radiance through M layers in the inhomogeneous atmosphere can be written as

$$I(\nu) = \sum_{i=1}^{N} \left\{ \bar{B}_\nu(T_0)\,\bar{T}_{ri,1} + \sum_{j=1}^{M} \bar{B}_\nu(T_j)(\bar{T}_{ri,j+1} - \bar{T}_{ri,j}) \right\} \Delta g_i. \tag{3–8}$$

Before applying the correlated-k method in the retrieval algorithm to calculate the spectrum in a particular spectral region, we need to first calculate $k(g)$ to form a set of k-tables corresponding to the specific planet and the instrument. The k-tables are obtained from line data and must include all the spectral active gas within the frequency range of interested. Detailed calculations are beyond the scope of this dissertation, and interested readers can refer to Irwin et al. (1999; 2006).

3.3 Retrieval Method

The relationship between the measurement **y** and the profile of interest **x** can be described by a forward function **f**, so that $\mathbf{y} = \mathbf{f}(\mathbf{x})$. However, not only is the physics of the forward function not fully understood, but there are also measurement and experimental errors. Thus, the actual relationship between the measured quantity and the desired profile can be written as $\mathbf{y} = \mathbf{F}(\mathbf{x}) + \epsilon$. **F** is the forward model, which describes the physics of the measurement, based on our knowledge of atmospheric radiation theory with approximations as described in Section 3.2. ϵ is the error corresponding to the measurement, which includes systematic and random errors.

To derive the vertical temperature profile and the cloud distribution in Saturn's atmosphere, we use the infrared radiation emitted from the top of the atmosphere measured by the spacecraft Cassini/CIRS orbiting around Saturn. The problems we try to solve are ill-posed non-linear problems, and it is nearly impossible to find exact solutions with the presence of the measurement error. Therefore, finding a reasonable solution that fits the observation within the experimental errors is the essential task.

In this work, we use a multi-stage linear inversion technique, which is described in detail by Matcheva et al. (2005), Conrath et al. (1998), Rodgers (1976; 2000) and Rodgers and Connor (2003). The inversion method is outlined below.

Let $X(z)$ be the profile of an atmospheric parameter we wish to retrieve at a given height z, and $I(\nu)$ is the measured radiance, which is a function of the wavenumber ν. Atmospheric parameters $X(z)$ can be temperature, gas mixing ratios, or cloud

absorption coefficient. In a multi-stage inversion, $X(z)$ is retrieved sequentially to avoid non-uniqueness problems arising from the correlation of variables (Fletcher et al., 2009).

Discretizing the continuous profiles into hundreds of levels and retrieving the solutions with vectors and matrices help to avoid the tedious numerical calculation. We can discretize $X(z)$ into n vertical layers and $I(\nu)$ into m wavenumbers within the chosen spectral range. The non-linear problem can also be simplified by linearizing the forward model about a reference atmospheric state $X^0(z)$, and the relationship between the measured radiance and the profile becomes

$$I(\nu_i) = F_i(X^0(z_j)) + \sum_{j=1}^{n} \frac{\partial F_i(X(z))}{\partial X(z_j)}(X(z_j) - X^0(z_j)) + \epsilon_i, \tag{3–9}$$

and

$$i = 1, 2, ...m; \quad j = 1, 2, ...n,$$

where F_i is the intensity of the outgoing thermal radiation at wavenumber ν_i measured from the top of an optically thick atmosphere based on the radiative transfer theory, and

$$F_i(X(z)) = \int_0^\infty \left(\frac{\partial T_r(z)}{\partial z}\right) B(\nu_i, z)\mathrm{d}z. \tag{3–10}$$

Upon replacing $F_i(X^0(z_j))$ with $I^0(\nu_i)$, Eq. 3–9 becomes

$$\Delta I_i = \sum_{j=1}^{n} \frac{\partial F_i(X(z))}{\partial X(z_j)} \Delta X_j + \epsilon_i, \tag{3–11}$$

where

$$\Delta I_i = I(\nu_i) - I^0(\nu_i), \quad \Delta X_j = X(z_j) - X^0(z_j). \tag{3–12}$$

In our discretized equation, z is a dimensionless altitude defined as

$$z = -ln\frac{p}{p_0} \tag{3–13}$$

with a reference altitude $z_0 = 0$ at $p_0 = 1000$ mbar.

Define the functional derivative matrix **K** with components

$$K_{ij} = \frac{\partial F_i(X(z))}{\partial X(z_j)}, \tag{3–14}$$

the linear radiative equation Eq. 3–11 then can be written as

$$\mathbf{\Delta I} = \mathbf{K}\mathbf{\Delta X} + \boldsymbol{\epsilon}. \tag{3–15}$$

The $m \times n$ matrix **K** is sometimes referred to as the weighting matrix, the Jacobian, the kernel, the sensitivity kernel, the tangent linear model, or the adjoint in the inverse method literatures (Rodgers, 2000). The properties and the detailed mathematical derivation of **K** corresponding to the radiation theory will be discussed in Section 3.4.

ΔI is a column vector in a m-dimensional measurement space, while **ΔX** can be thought of as a column vector in a n-dimensional state space. Therefore, to solve Eq. 3–15 is to determine a mapping back from the measurement space into the state space. Eq. 3–15 can be solved by minimizing a cost function Q defined as

$$Q = (\mathbf{\Delta I} - \mathbf{K}\mathbf{\Delta X})^T \mathbf{E}^{-1} (\mathbf{\Delta I} - \mathbf{K}\mathbf{\Delta X}) + \gamma \mathbf{a}^T \mathbf{a}. \tag{3–16}$$

E is the measurement error covariance matrix. The superscript T in the equation above denotes matrix transposition, and the parameter γ reflects the relative weight of the initial guess for the solution in the final result. Column vector **a** contains the expansion coefficients and expands **ΔX** in a set of basis vectors. The relationship between **ΔX** and **a** is

$$\mathbf{\Delta X} = \mathbf{H}\mathbf{a}, \tag{3–17}$$

where **H** is a matrix whose columns are the basis vectors.

With the minimization of the cost function Q, **ΔX** can be estimated as

$$\mathbf{\Delta X} = \mathbf{S}\mathbf{K}^{\mathsf{T}} (\mathbf{K}\mathbf{S}\mathbf{K}^{\mathsf{T}} + \gamma \mathbf{E})^{-1} \mathbf{\Delta I}. \tag{3–18}$$

$\mathbf{S} = \mathbf{H}\mathbf{H}^T$ is a two-point correlation matrix of the basis vectors and is defined as

$$S_{ij} = \exp\left[\frac{-(z_i - z_j)^2}{2c^2}\right], \tag{3–19}$$

where c is the correlation length in scale heights. We use $c = 0.5$ for the temperature inversions and $c = 0.01$ for the cloud inversions in this work.

In each iteration, the functional derivative matrix **K** is calculated for the estimation of $\mathbf{\Delta X}$ to modify the radiance I. This procedure is repeated iteratively until a set of requirements is satisfied.

3.4 Functional Derivative Matrix K

In the retrieval model, functional derivative matrix **K**, defined as Eq. 3–14, is the matrix whose components are the rate of change of the radiance with respect to changes in the atmospheric variables. To obtain **K** in the retrieval model, we can adjust the atmospheric variable at each layer and calculate the entire spectrum, and then divide calculated change in the emission by the change of the atmospheric property. This approach is straightforward, however, it requires multiple calculations of the spectrum for each iteration; this would result in a rather slow and inefficient retrieval process.

An alternative approach is to calculate **K** analytically at the deepest subroutine level, starting from Eq. 3–10 with transmittance at wavenumber ν_i defined as

$$T_r(\mu, \nu_i, z) = e^{-\frac{1}{\mu}\tau(z)}. \tag{3–20}$$

μ is the cosine of the emission angle and

$$\tau(z) = \int_z^\infty Y(z')\mathrm{d}z' = \int_{-\infty}^\infty Y(z')\theta(z' - z)\mathrm{d}z' \tag{3–21}$$

is the optical depth at height z. $Y(z)$ is the dimensionless cloud absorption coefficient.

The detailed derivations of K_{ij} for the temperature retrieval and the cloud retrieval are discussed in the following sections.

3.4.1 K_{ij} for the Temperature Retrievals

For the temperature retrieval, the rate of the change of radiance with respect to the change of the temperature is

$$\begin{aligned}\frac{\partial F_i}{\partial T_j} &= \frac{\partial F_i(\mu, \nu_i, z)}{\partial T(z_j)} \\ &= \int_0^\infty \frac{\partial}{\partial T(z_j)} \left[\frac{\partial Tr(\mu, \nu_i, z)}{\partial z} B(\nu_i, T(z))\right] \mathrm{d}z \\ &= \int_0^\infty \frac{\partial^2 Tr(\mu, \nu_i, z)}{\partial T(z_j)\partial z} B(\nu_i, T(z))\mathrm{d}z + \int_0^\infty \frac{\partial B(\nu_i, T(z))}{\partial T(z_j)} \frac{\partial Tr(\mu, \nu_i, z)}{\partial z}\mathrm{d}z\end{aligned} \tag{3–22}$$

$B(\nu_i, T(z))$ is the Planck radiance at temperature T at wavenumber ν_i. The partial derivative

$$\begin{aligned}\frac{\partial T_r(\mu, \nu_i, z)}{\partial z} &= -\frac{1}{\mu} e^{-\frac{1}{\mu}\tau(z)} \frac{\partial \tau}{\partial z} \\ &= -\frac{1}{\mu} T_r(\mu, \nu_i, z) \frac{\partial \tau(z)}{\partial z}.\end{aligned} \tag{3–23}$$

The equation above becomes

$$\begin{aligned}\frac{\partial F_i}{\partial T_j} &= \int_0^\infty \frac{\partial}{\partial T(z_j)} \left[-\frac{1}{\mu} Tr(\mu, \nu_i, z) \frac{\partial \tau(z)}{\partial z}\right] B(\nu_i, T(z))\mathrm{d}z \\ &\quad + \int_0^\infty \frac{\partial B(\nu_i, T(z))}{\partial T(z_j)} \frac{\partial Tr(\mu, \nu_i, z)}{\partial z}\mathrm{d}z \\ &= \int_0^\infty -\frac{1}{\mu}\left[\frac{\partial Tr(\mu, \nu_i, z)}{\partial T(z_j)} \frac{\partial \tau(z)}{\partial z} B(\nu_i, T(z)) + Tr(\mu, \nu_i, z) \frac{\partial^2 \tau(z)}{\partial T(z_j)\partial z} B(\nu_i, T(z))\right] \mathrm{d}z \\ &\quad + \int_0^\infty \frac{\partial B(\nu_i, T(z))}{\partial T(z_j)} \frac{\partial Tr(\mu, \nu_i, z)}{\partial z}\mathrm{d}z.\end{aligned} \tag{3–24}$$

The first term vanishes because $Tr(\mu, \nu_i, z)$ and $\tau(z)$ are independent on $T(z_j)$, and

$$\frac{\partial B(\nu_i, T(z))}{\partial T(z_j)} \neq 0$$

only when $z_j = z$. The functional derivative K_{ij} for temperature retrieval at wavenumber ν_i at height z_j becomes

$$\boxed{K_{ij} = \frac{\partial F_i}{\partial T_j} = \frac{\partial B(\nu_i, T(z))}{\partial T(z_j)} \frac{\partial Tr(\mu, \nu_i, z)}{\partial z} \mathrm{d}z} \tag{3–25}$$

3.4.2 K_{ij} for the Clouds/Haze Retrievals

We use a similar approach to calculate the functional derivative K_{ij} for cloud retrievals. However, instead of using the change of the absorption coefficient Y_j at the height z_j, we chose to use the change of the $\ln Y_j$ as the denominator. Solving for $\ln Y_j$ in the cloud retrievals will eliminate the possibility of resulting in unphysical solutions due to mathematical consistency. It will avoid the negative absorption coefficient Y_j in the solution, so that the optical depth τ_c would decrease monotonically with height. Moreover, many atmospheric parameters, such as pressure, mass and density, vary exponentially with altitude. Consequently, using logarithmic variables would also make the numerical computation less demanding (Matcheva et al., 2005).

K_{ij} for cloud retrievals is derived as

$$\begin{aligned}
K_{ij} &= \frac{\partial F_i(\mu, \nu_i, z)}{\partial \ln Y_j} = Y(z_j) \frac{\partial F_i(\mu, \nu_i, z)}{\partial Y(z_j)} \\
&= Y(z_j) \int_{-\infty}^{\infty} \frac{\partial}{\partial Y(z_j)} \left[\frac{\partial Tr(\mu, \nu_i, z)}{\partial z} B(T(z)) \right] \mathrm{d}z \\
&= Y(z_j) \int_{-\infty}^{\infty} \left[\frac{\partial^2 Tr(\mu, \nu_i, z)}{\partial Y(z_j) \partial z} B(T(z)) + \frac{\partial Tr(\mu, \nu_i, z)}{\partial z} \cancelto{0}{\frac{\partial B(T(z))}{\partial Y(z_j)}} \right] \mathrm{d}z \\
&= Y(z_j) \int_{-\infty}^{\infty} \frac{\partial}{\partial Y(z_j)} \left[-\frac{1}{\mu} Tr(\mu, \nu_i, z) \frac{\partial \tau(z)}{\partial z} B(T(z)) \right] \mathrm{d}z \\
&= -\frac{Y(z_j)}{\mu} \int_{-\infty}^{\infty} \left[\frac{\partial Tr(\mu, \nu_i, z)}{\partial Y(z_j)} \frac{\partial \tau(z)}{\partial z} + Tr(\mu, \nu_i, z) \frac{\partial^2 \tau(z)}{\partial Y(z_j) \partial z} \right] B(T(z)) \mathrm{d}z
\end{aligned} \tag{3–26}$$

The partial derivatives

$$\begin{aligned}\frac{\partial\tau(z)}{\partial Y(z_j)} &= \int_{-\infty}^{\infty}\frac{\partial}{\partial Y(z_j)}\left[Y(z')\theta(z'-z)\right]\mathrm{d}z' \\ &= \int_{-\infty}^{\infty}\frac{\partial Y(z')}{\partial Y(z_j)}\theta(z'-z)\mathrm{d}z' + \int_{-\infty}^{\infty}Y(z')\cancelto{0}{\frac{\partial\theta(z'-z)}{\partial Y(z_j)}}\mathrm{d}z' \\ &= \theta(z_j-z)\mathrm{d}z_j,\end{aligned} \tag{3–27}$$

and

$$\begin{aligned}\frac{\partial T_r(\mu,\nu_i,z)}{\partial Y(z_j)} &= -\frac{1}{\mu}e^{-\frac{1}{\mu}\tau(z)}\frac{\partial\tau(z)}{\partial Y(z_j)} \\ &= -\frac{1}{\mu}\tau(z)\,T_r(\mu,\nu_i,z)\frac{\partial\tau(z)}{\partial Y(z_j)} \\ &= -\frac{1}{\mu}\tau(z)\,T_r(\mu,\nu_i,z)\theta(z_j-z)\mathrm{d}z_j\end{aligned} \tag{3–28}$$

Eq. 3–26 can be written as

$$\begin{aligned}K_{ij} &= -\frac{Y(z_j)}{\mu}\int_{-\infty}^{\infty}-\frac{1}{\mu}\tau(z)\,Tr(\mu,\nu_i,z)\theta(z_j-z)\mathrm{d}z_j\frac{\partial\tau(z)}{\partial z}B(T(z))\mathrm{d}z \\ &\quad -\frac{Y(z_j)}{\mu}\int_{-\infty}^{\infty}Tr(\mu,\nu_i,z)\frac{\partial^2\tau(z)}{\partial z\partial Y(z_j)}B(T(z))\mathrm{d}z \\ &= -\frac{Y(z_j)}{\mu}\int_{-\infty}^{\infty}\left[-\frac{1}{\mu}\tau(z)\,Tr(\mu,\nu_i,z)\frac{\partial\tau(z)}{\partial z}\mathrm{d}z\right]\theta(z_j-z)\mathrm{d}z_jB(T(z)) \\ &\quad -\frac{Y(z_j)}{\mu}\int_{-\infty}^{\infty}Tr(\mu,\nu_i,z)\frac{\partial}{\partial z}\left[\theta(z_j-z)\mathrm{d}z_j\right]B(T(z))\mathrm{d}z \\ &= -\frac{Y(z_j)}{\mu}\int_{-\infty}^{\infty}\mathrm{d}\,Tr(\mu,\nu_i,z)B(T(z))\theta(z_j-z)\mathrm{d}z_j \\ &\quad -\frac{Y(z_j)}{\mu}\int_{-\infty}^{\infty}Tr(\mu,\nu_i,z)\left[-\delta(z_j-z)\mathrm{d}z_j\right]B(T(z))\mathrm{d}z \\ &= -\frac{Y(z_j)}{\mu}\int_{-\infty}^{\infty}\mathrm{d}\,Tr(\mu,\nu_i,z)B(T(z))\theta(z_j-z)\mathrm{d}z_j \\ &\quad +\frac{Y(z_j)}{\mu}\int_{-\infty}^{\infty}Tr(\mu,\nu_i,z)\delta(z_j-z)B(T(z))\mathrm{d}z_j \\ &= -\frac{Y(z_j)}{\mu}\int_{-\infty}^{\infty}\mathrm{d}\,Tr(\mu,\nu_i,z)B(T(z))\theta(z_j-z)\mathrm{d}z_j+\frac{Y(z_j)}{\mu}Tr(\mu,\nu_i,z_j)B(T(z_j))\mathrm{d}z_j\end{aligned} \tag{3–29}$$

The discretized functional derivative K_{ij} at height z_j at wavenumber ν_i for the clouds/haze retrieval is

$$K_{ij} = \frac{\partial F_i}{\partial \ln Y_j} = Y(z_j)\frac{\Delta z}{\mu}\left[B(\nu_i, T(z_j))\,Tr(\mu, \nu_i, z_j) - \sum_{q=j}^{m} B(\nu_i, T(z_q))\Delta\, Tr(\mu, \nu_i, z_q)\right]$$

3.5 Error Analysis

To estimate the uncertainty in the retrieved X profile, X_j is allowed to vary so that the change of radiance I_i is limited within the observational error. For FP3 (570 - 1125 cm^{-1}) and FP4 (1025 - 1495 cm^{-1}), observational noise is present in the measured spectra, deep space calibration spectra and warm calibration spectra. Following a similar approach in Teanby et al. (2006), the expected error of N spectra in the zonal mean average with N_w warm calibration (shutter closed) spectra and N_c cold calibration (deep space) spectra can be written as

$$\sigma^2 = \frac{\varepsilon^2_{NESR}}{N^2} + \frac{\varepsilon^2_{NESR}}{N_w^2} + \frac{\varepsilon^2_{NESR}}{N_c^2}, \tag{3–30}$$

where ε_{NESR} is the mean Noise Equivalent Spectral Radiance (NESR). The NESRs of FP3 and FP4 vary slowly with wavenumbers and are assumed to be constant. The averaged values of ε_{NESR} are 7.811314×10^{-9} $Wcm^{-2}sr^{-1}(cm^{-1})^{-1}$ for FP3 and 1.601580×10^{-9} $Wcm^{-2}sr^{-1}(cm^{-1})^{-1}$ for FP4.

In our work, the observational error within the selected spectral range is dominated by the calibration spectra because the typical number of N is about 4000 - 10000, and the number of calibration spectra is usually less than 100. Therefore the relationship between the change of the radiance I_i and the varying amount of X_j can be written based on Eq. 3–11 and Eq. 3–14 as

$$|\delta I_i| = \left|\sum_{j=1}^{n} K_{ij}\delta X_j\right| \leq \sqrt{\frac{\varepsilon^2_{NESR}}{N_w^2} + \frac{\varepsilon^2_{NESR}}{N_c^2}} = \sigma_{calibration}, \tag{3–31}$$

and

$$i = 1, 2, ...m; \quad j = 1, 2, ...n.$$

For each altitude z_j and wavenumber ν_i, Eq. 3–31 should be satisfied independently; for each i and j, it can be shown as

$$|K_{ij}\delta X_j| \leq \sigma_{calibration}. \tag{3–32}$$

For each altitude z_j, if we let the functional derivative K_{qj} be the largest amongst the spectral range of interest ($|K_{qj}| \geq |K_{ij}|$), then $|K_{qj}|$ will provide the best sensitivity in that layer j. Eq. 3–31 can then be written as

$$|\delta X_j| \leq \frac{\sigma_{calibration}}{|K_{qj}|} = \varepsilon_{X_j}, \tag{3–33}$$

$$j = 1, 2, ...n.$$

ε_{X_j} is the uncertainty of the retrieved atmospheric parameter X_j at altitude z_j within the retrieval spectral range due to the observational and calibration noise.

Error analysis for cloud/hazes retrievals

The atmospheric parameter solved from the retrieval model for clouds and haze is the logarithmic of the absorption coefficient Y, so the uncertainty of the retrieved results at height z_j can be derived from Eq. 3–33 with $X_j = \ln Y_j$, where

$$|\delta X_j| = |\delta \ln Y_j| = \left|\frac{\delta Y_j}{Y_j}\right| \leq \frac{\sigma_{calibration}}{|K_{qj}|}. \tag{3–34}$$

The uncertainty of the retrieved absorption coefficient for clouds and haze at height z_j is

$$\varepsilon_{Y_j} = |\delta Y_j| = \frac{|Y_j|}{|K_{qj}|}\sigma_{calibration}, \tag{3–35}$$

$$j = 1, 2, ...n.$$

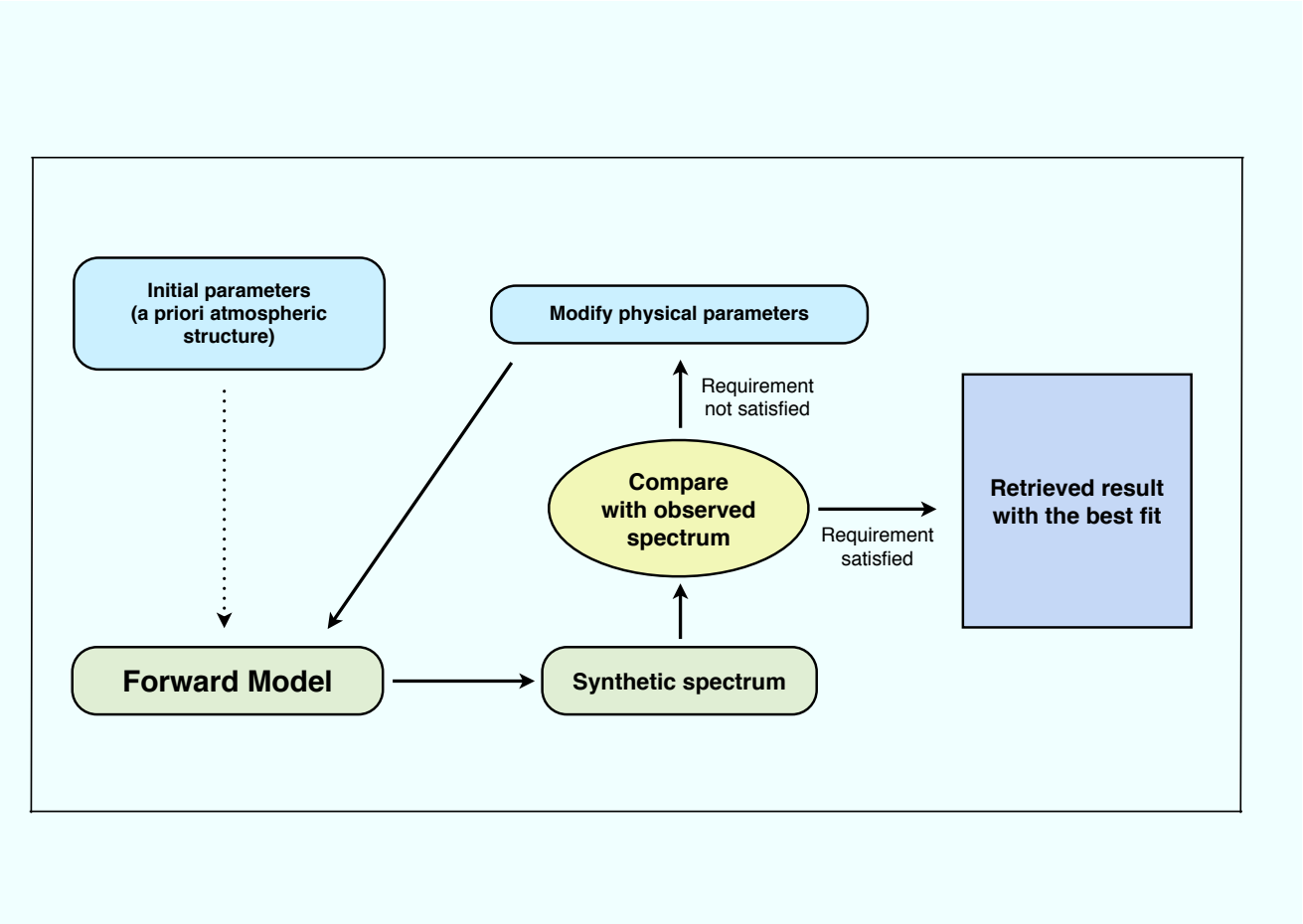

Figure 3-1. Flow chart of the retrieval algoritm.

CHAPTER 4
TEMPERATURE RETRIEVAL

4.1 Introduction

To acquire the vertical distribution and optical properties of the clouds and haze at various southern latitudes in 2005, we first construct the temperature profiles in a clear atmosphere on Saturn's southern hemisphere. In this work, we use calibrated mid-infrared data from Cassini/CIRS MIRMAP observations listed in Table 2-1. We average the radiances over 4 degrees in latitude with 2 degrees overlapping between the adjacent zonal bands. The mean emission angles within the latitudinal bands are also calculated with the average radiances. We then obtain the retrieved temperature profile with the use of the retrieval algorithm described in Sec. 3.3 by minimizing the differences within the defined spectral range between the observed spectrum and the synthetic spectrum generated by an initial temperature profile.

Fig. 4-1 shows the initial temperature profiles used for the forward calculation to generate the synthetic spectrum. For low and mid-latitudes, we use the retrieved profile (red curve in 4-1) from Voyager/IRIS observations by Courtin et al. (1984) and the modified one (green curve in 4-1) as the initial temperature profiles. For high latitudes, the initial profile (blue curve in Fig. 4-1) is about 20K warmer at pressures less than a few mbars in the stratosphere compared with the temperature profile from the Voyager/IRIS observations. The warmer stratospheric temperature is due to high emission angles at high latitudes. These initial temperature profiles are interpolated onto a grid of 200 points between 0.01 mbar and 5 bar pressure levels. For layers below the tropopause with pressures larger than 500 mbar, we assume the temperature increases with the dry adiabatic lapse rate as the pressure increases.

In the forward calculation, we use the correlated-k method (Goody et al., 1989; Lacis and Oinas, 1991; Liou, 2002) described in Sec. 3.2 to calculate the absorption spectra of CH_4 (1150 - 1600 cm^{-1}), NH_3 (600 - 1600 cm^{-1}), PH_3 (800 - 1350 cm^{-1}),

C_2H_2 (625 - 825 cm^{-1} and 1250 - 1400 cm^{-1}), C_2H_4 (825 - 1150 cm^{-1}), and C_2H_6 (750 - 900 cm^{-1}). The latitudinal dependent gravity is calculated based on equations by Anderson and Schubert (2007) varying from 12.07 m/s^2 at the pole to 9.03 m/s^2 at the equator. We assume the volume mixing ratio of He/H_2 is 0.135 (Conrath and Gautier, 2000) and the CH_4/H_2 volume mixing ratio is 5.3×10^{-3} (Fletcher et al., 2009).

The element of the functional derivative matrix **K** for the temperature retrieval modified from the one by Matcheva et al. (2005) is derived in Sec. 3.4.1 and shown as

$$K_{ij} = \frac{\partial B(\nu_i, T(z_j))}{\partial T(z_j)} \frac{\partial Tr(\mu, \nu_i, z_j)}{\partial z_j} \mathrm{d}z, \tag{4–1}$$

where $B(\nu_i, T(z_j))$ is the Planck radiance at temperature T at wavenumber ν_i, $T_r(\mu, \nu_i, z_j)$ is the atmospheric transmittance from the top of the atmosphere down to the layer z_j at the wavenumber ν_i, μ is the cosine of the emission angle, and $\mathrm{d}z$ is the difference between layer z_j and z_{j+1}. The uncertainty ε_{X_j} for temperature retrieval at altitude z_j within the retrieval spectral range is

$$\varepsilon_{X_j} = \frac{1}{|K_{qj}|} \sqrt{\frac{\varepsilon_{NESR}^2}{N_w^2} + \frac{\varepsilon_{NESR}^2}{N_c^2}}, \tag{4–2}$$

$$j = 1, 2, \ldots n,$$

where K_{qj} is the largest functional derivative amongst layer j, and K_{qj} gives the best sensitivity. N_w and N_c are the number of spectra in warm and cold calibrations, respectively, and ε_{NESR} is the mean Noise Equivalent Spectral Radiance (NESR).

In this work, we use a two-stage retrieval for temperature inversions. The collisional-induced absorption (CIA) of H_2 in the spectral range of 590 - 700 cm^{-1} is used to extract information about the temperature profile in the upper troposphere, whereas the methane emission in the spectral range of 1250 - 1350 cm^{-1} is used to retrieve the temperature profile in the stratosphere. The normalized contribution functions (functional derivatives) of H_2 and CH_4 in nadir-viewing geometry are shown in Fig. 4-2 and Fig. 4-3. The red regions in Fig. 4-2 and Fig. 4-3 indicate the regions where the rate of change of

observed radiance with temperature is the greatest. As we can see in these two figures, the pressure range sensitive to the H_2 absorptions is in the upper troposphere between 40 and 500 mbar with the peak sensitivity occurring near 100 mbar; the pressure range sensitive to the CH_4 emissions is in the stratosphere between 0.1 and 20 mbar with the peak sensitivity around 5 mbar. Temperature is well-constrained within these two sensitive pressure regions. Outside the constrained pressure range, the retrieved temperature will follow the initial guess due to the lack of direct information. For higher latitudes, the peak sensitivity to the H_2 absorptions would slightly shift to higher altitudes with lower pressures due to the increasing emission angles.

4.2 Results and Discussion

We use MIRMAP observations in 2005 for temperature inversions to analyze the vertical temperature distribution and the latitudinal variations of the temperature in the southern summer hemisphere on Saturn.

Fig. 4-4 and Fig. 4-5 present the retrieved vertical temperature profiles at 27°S and 77°S in 2005. The shaded regions indicate the uncertainties of the inversions and the red line is the initial temperature profile. Fig. 4-6 and Fig. 4-7 show the spectra after first-stage retrieval (CH_4). In these two figures, we can see the retrieved spectra are very close to the observed spectra in both latitudes within the selected spectral region between 1250 and 1350 cm^{-1}. For the second-stage retrieval (H_2), despite the small variations in the observed spectra, the retrieved spectra (blue lines) fit the general trend of the observed spectra (red lines) within the spectral range between 590 - 700 cm^{-1} as shown in Fig. 4-8 for 27°S and Fig. 4-9 for 77°S. The comparison of the observed spectra and the retrieved spectra after first- and second-stage inversions within the FP3 and FP4 spectral range (600 - 1500 cm^{-1}) are shown in Fig. 4-10 and Fig. 4-11.

4.2.1 Stratospheric Temperature

Stratospheric temperatures between 1 and 10 mbar are developed in the first stage of the two-stage temperature retrieval, which are shown in Fig. 4-12 and Fig. 4-13, with

the CH_4 emission lines at 2.8 cm^{-1} spectral resolution in the 1250 - 1350 cm^{-1}. For pressure less than 0.1 mbar and larger than 20 mbar, the retrieved temperature will tend to follow the initial guess due to lack of information for retrievals. The retrieved temperature around 5 mbar at 77°S is near 160 K and is about 15 K higher than the temperature at 27°S.

To see the latitudinal variations of the retrieved stratospheric temperature, we construct a map that shows the temperature of Saturn's southern hemisphere retrieved from 2005 MIRMAP datasets listed in Table 2-1. Our results are consistent with the temperature structure analysis of CIRS data by Flasar et al. (2005) and Fletcher et al. (2007), in which the result is derived from far-infrared data. As one can see in Fig. 4-14, the temperature increases from mid-latitudes to higher latitudes for pressure range between 0.3 mbar and 5 mbar. Temperature elevates slightly from low latitudes toward the equator. The stratospheric temperature at the polar region is about 15K-20K warmer than that at the equator around 2 mbar pressure level. This phenomenon of warmer stratospheric temperature at higher latitudes in 2005 observations may be a result of more solar insolation at higher latitudes after Saturn's southern summer solstice (October, 2002).

However, as mentioned in Flasar et al. (2005), Saturn's polar stratospheric temperature predicted by simple radiative models should only be warmer than the equator by 5 K in 2005. This is because the radiative relaxation time in the stratosphere is 9.5 years, which results in the atmospheric response lagging behind the seasonally-modulated solar heating by a sixth of a Saturn's orbital period (29.5 Earth years). The warmer than expected polar stratospheric temperature may be caused by dynamical forcing as suggested by Flasar et al. (2005).

4.2.2 Tropospheric Temperature and Temperature Knee

Tropospheric temperatures between 40 mbar and 500 mbar are retrieved at the second stage of the temperature inversion with the collisional-induced absorption of H_2

in the 590 - 700 cm^{-1}. For pressure level below 5 mbar, there is no obvious latitudinal variation of the retrieved temperature. The temperature at tropopause is between 88 K and 95 K for all latitudes at around 100 mbar as shown in Fig. 4-14. As the radiative time constant increases with increasing pressure in deeper levels of the atmosphere (Conrath and Pirraglia, 1983), the seasonal effect (Cess and Caldwell, 1979) of the tropospheric temperature related to Saturn's orbital obliquity is less pronounced comparing with the stratospheric temperature.

Tropospheric temperature knee is the change to the tropospheric lapse rate with a local maximum in the upper troposphere (Fletcher et al., 2007). Tropospheric temperature knee is first observed in retrieved temperature profiles from Voyager/IRIS observations by Hanel et al. (1981; 1982), and it is later confirmed by Fletcher et al. (2007) from Cassini/CIRS far-infrared and mid-infrared observations. Temperature knee is seen in many of our retrieved temperature profiles at different latitudes. The feature of the small inversion of the temperature near 100 mbar is shown in Fig. 4-5. Fletcher et al. (2007) studied the latitudinal variations of the temperature knee with FIRMAP datasets from 2004 to 2006, and the study concluded that the temperature knee between 150 - 300 mbar during this observation period is larger in the southern summer hemisphere than in the northern winter hemisphere. Furthermore, the temperature knee is smaller and higher in the equator, deeper and larger in the equatorial belts, and small at the poles.

Fig. 4-15 shows our retrieved results from 2005 in the southern summer hemisphere. Our results reflect that tropospheric temperature knee is deeper at low- and mid-latitudes located between 100 mbar and 200 mbar, and it is around 60 mbar at higher latitudes. We noticed that the temperature knee is not always developed in the temperature retrievals. The retrieved temperature knee has a correlation with the peak location of the normalized functional derivative K (contribution function) and the initial temperature profiles. The results also reveal that the height of the knee varies with the peak location

of K, at which pressure level is the most sensitive to H_2 absorption. K is higher at high latitudes due to increasing emission angles. With large uncertainties of the retrieved results in the upper troposphere, the physical existence of the temperature knee is still debatable. The cause of this change in the lapse rate in the upper troposphere still needs to be carefully examined.

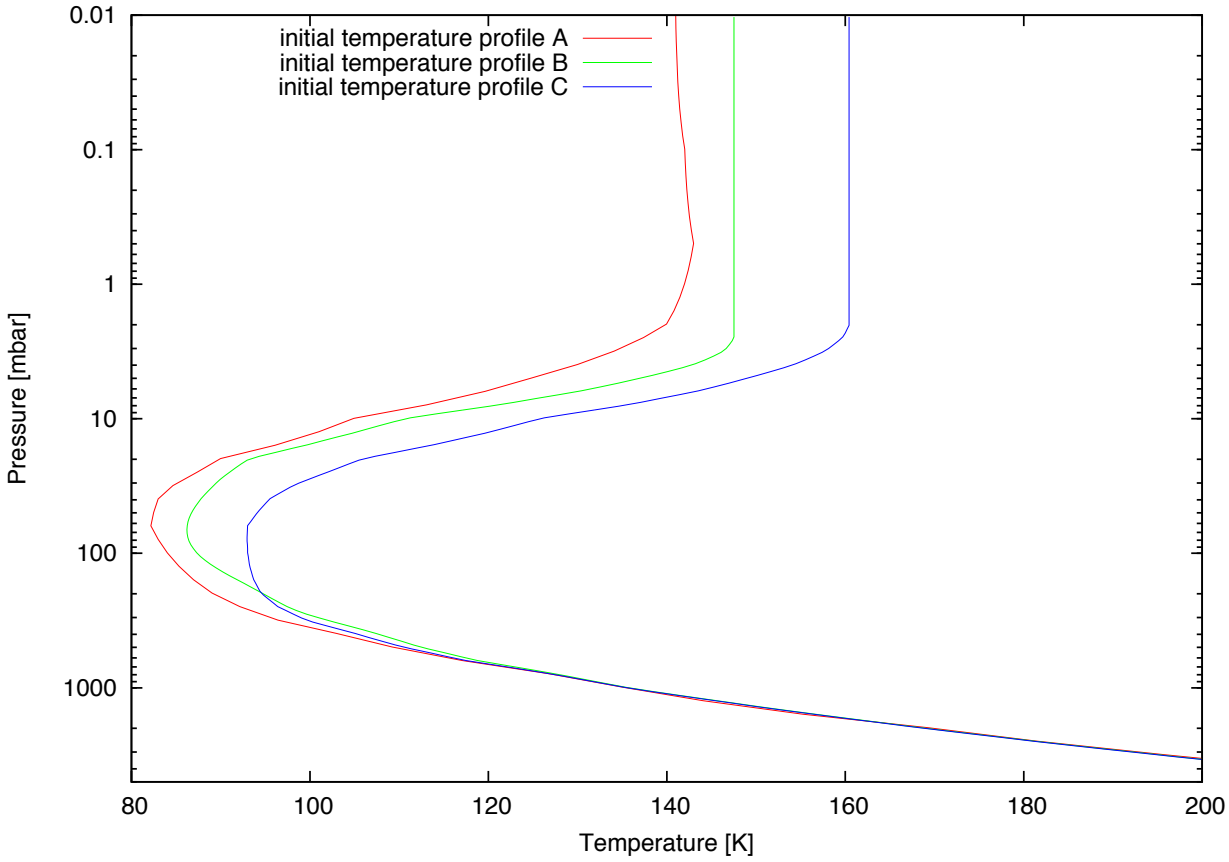

Figure 4-1. Initial temperature profiles for temperature retrievals. The initial temperature profile A, used for temperature retrievals at low and mid-latitudes, is the retrieved profile from Voyager/IRIS observations by Courtin et al. (1984). The profile C is modified from profile A, and it is used for temperature retrievals at high latitudes.

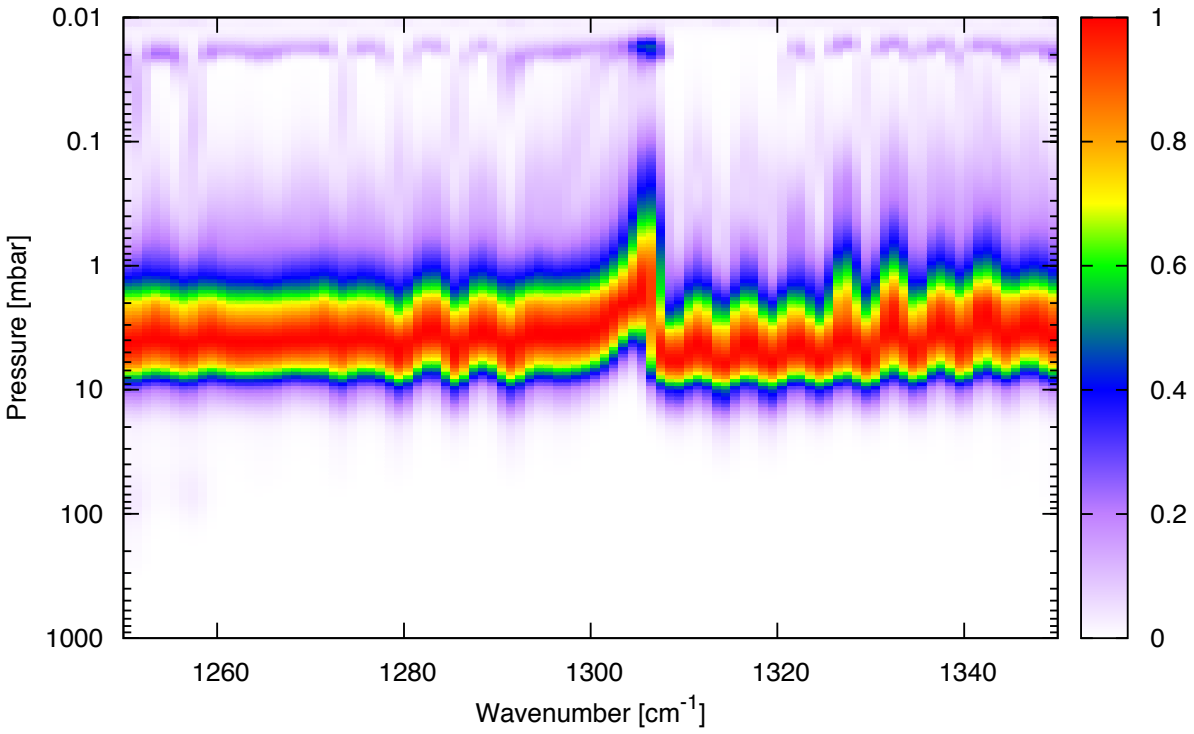

Figure 4-2. Contribution function for CH_4 at 27°S in 2005. The color zone indicates the pressure level (1-10 mbar) at where the rate of change of observed radiance with temperature is the greatest within the spectral region between 1250 cm^{-1} and 1350 cm^{-1} in the nadir-viewing geometry.

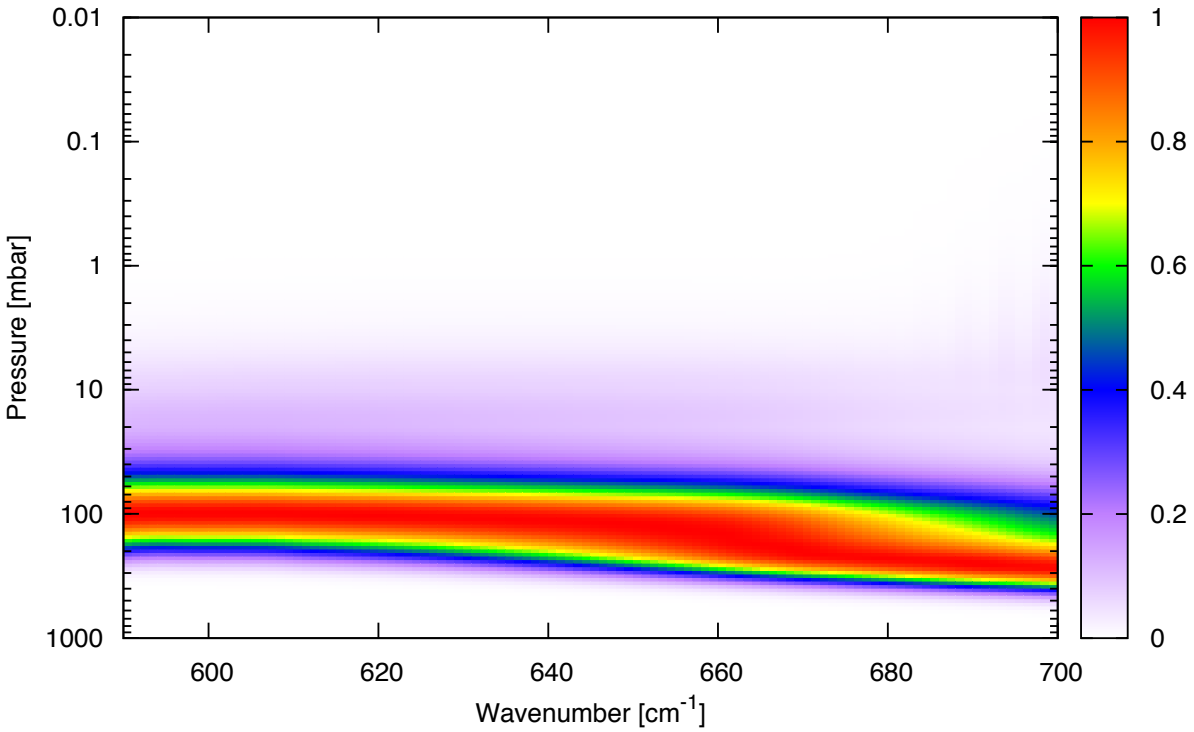

Figure 4-3. Contribution function for H_2 at 27°S in 2005. The color zone indicates the pressure level (40-200 mbar) at where the rate of change of observed radiance with temperatureis the greatest within the spectral region between 590 cm^{-1} and 700 cm^{-1} in the nadir-viewing geometry.

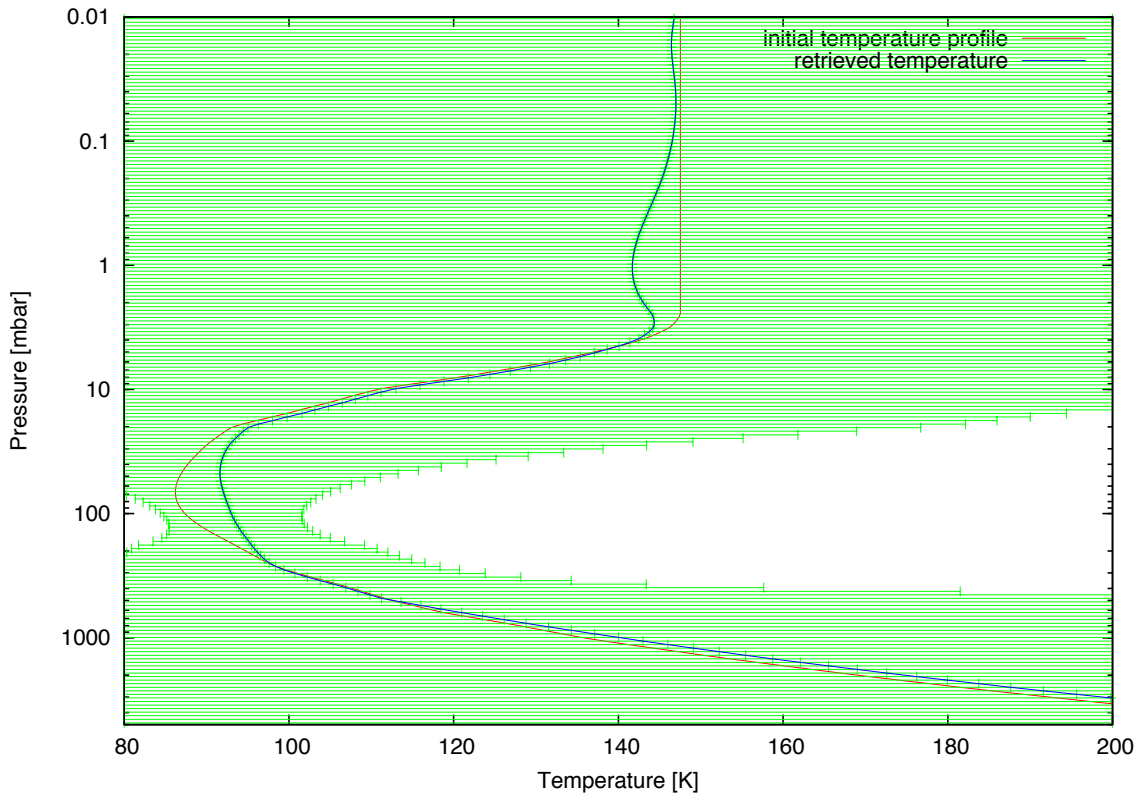

Figure 4-4. Temperature profile at 27°S in 2005 after the second stage of temperature retrieval.

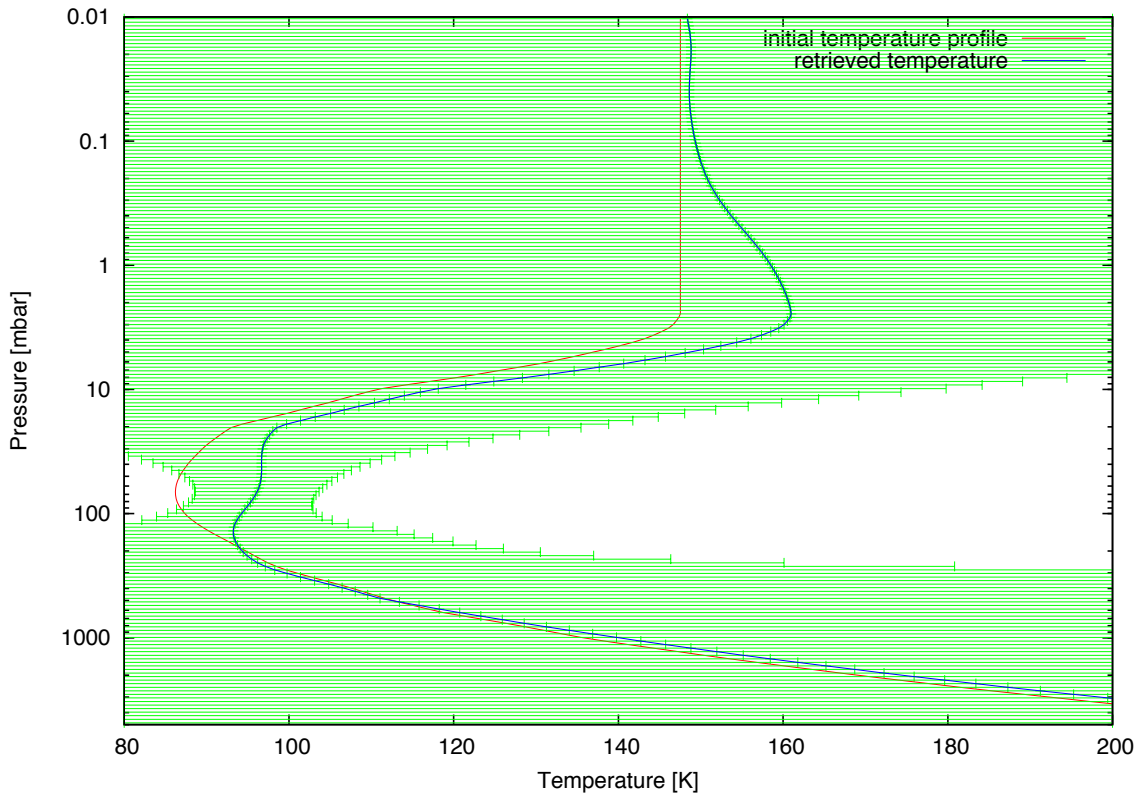

Figure 4-5. Temperature profile at 77°S in 2005 after the second stage of temperature retrieval.

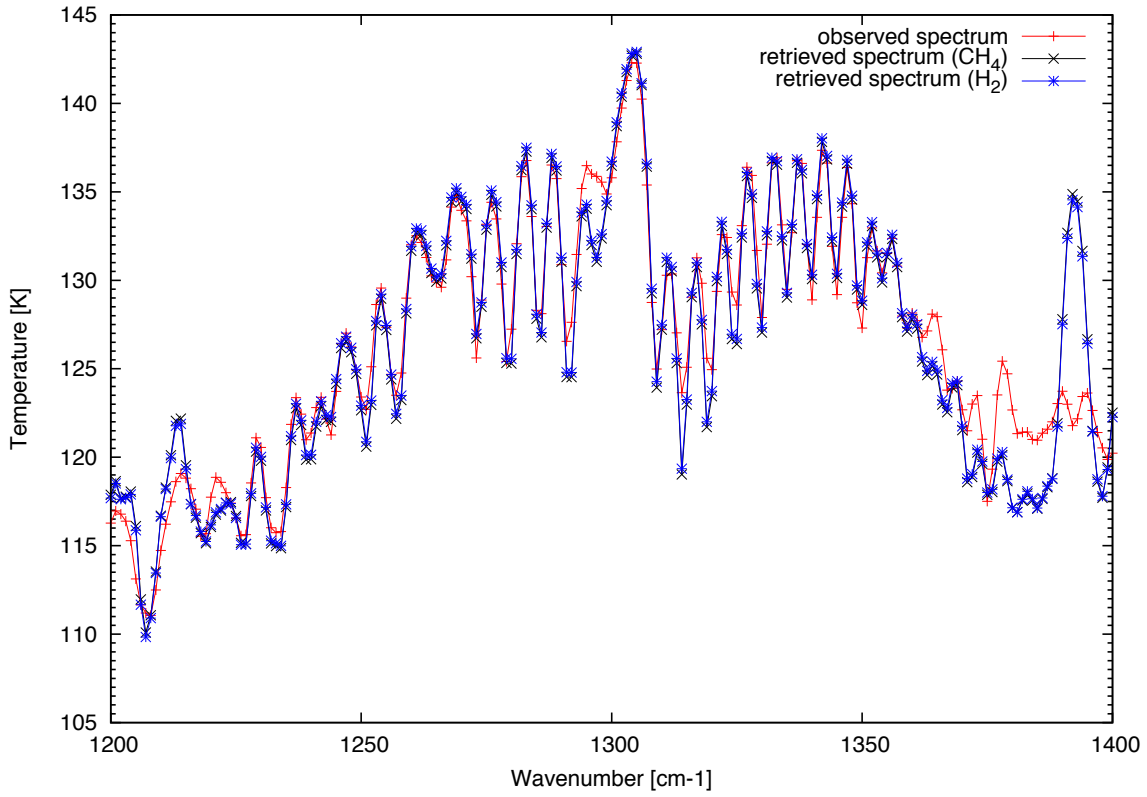

Figure 4-6. Partial spectrum (1200 - 1400 cm^{-1}) at 27°S in 2005 after the first stage of temperature retrieval.

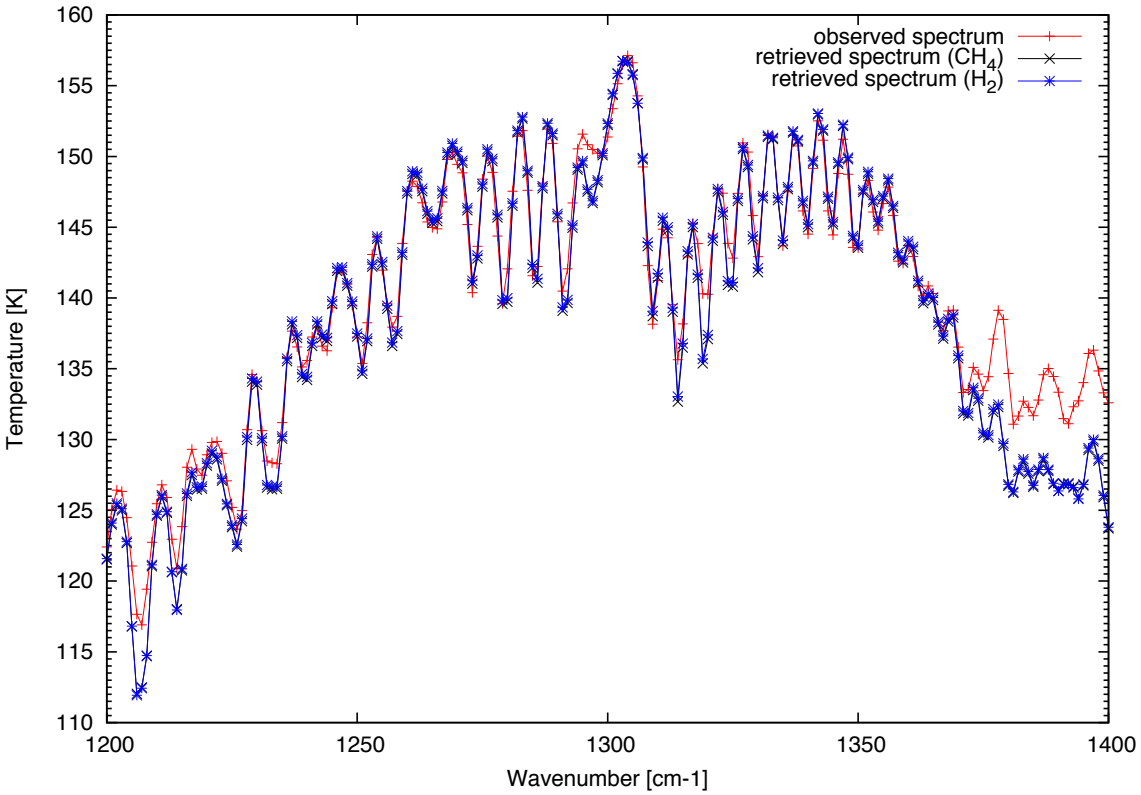

Figure 4-7. Partial spectrum (1200 - 1400 cm^{-1}) at 77°S in 2005 after the first stage of temperature retrieval.

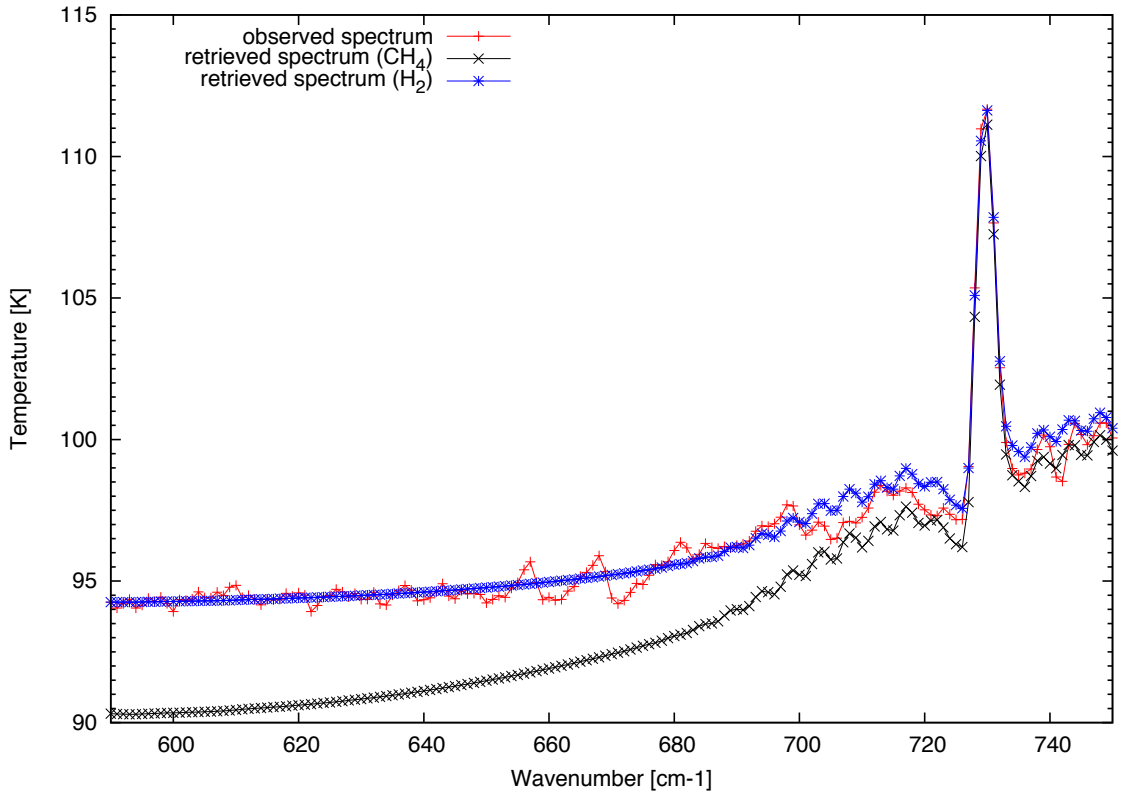

Figure 4-8. Partial spectrum (590 - 750 cm^{-1}) at 27°S in 2005 after the second stage of temperature retrieval.

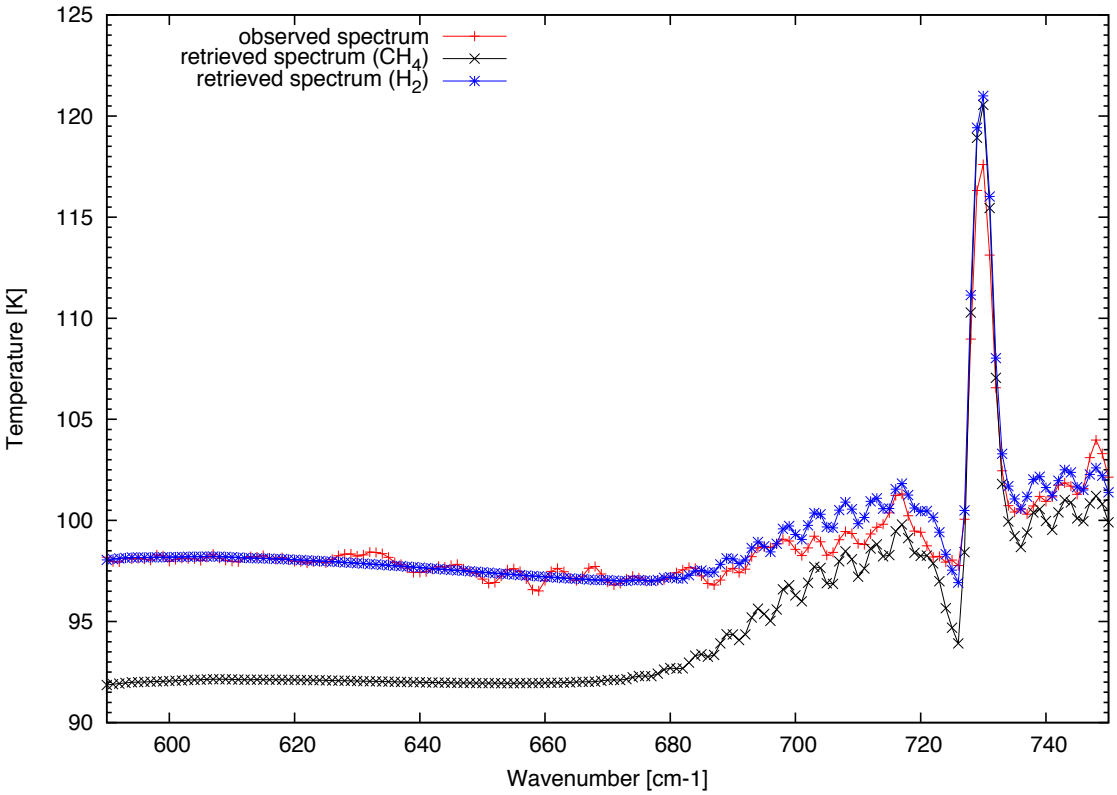

Figure 4-9. Partial spectrum (590 - 750 cm^{-1}) at 77°S in 2005 after the second stage of temperature retrieval.

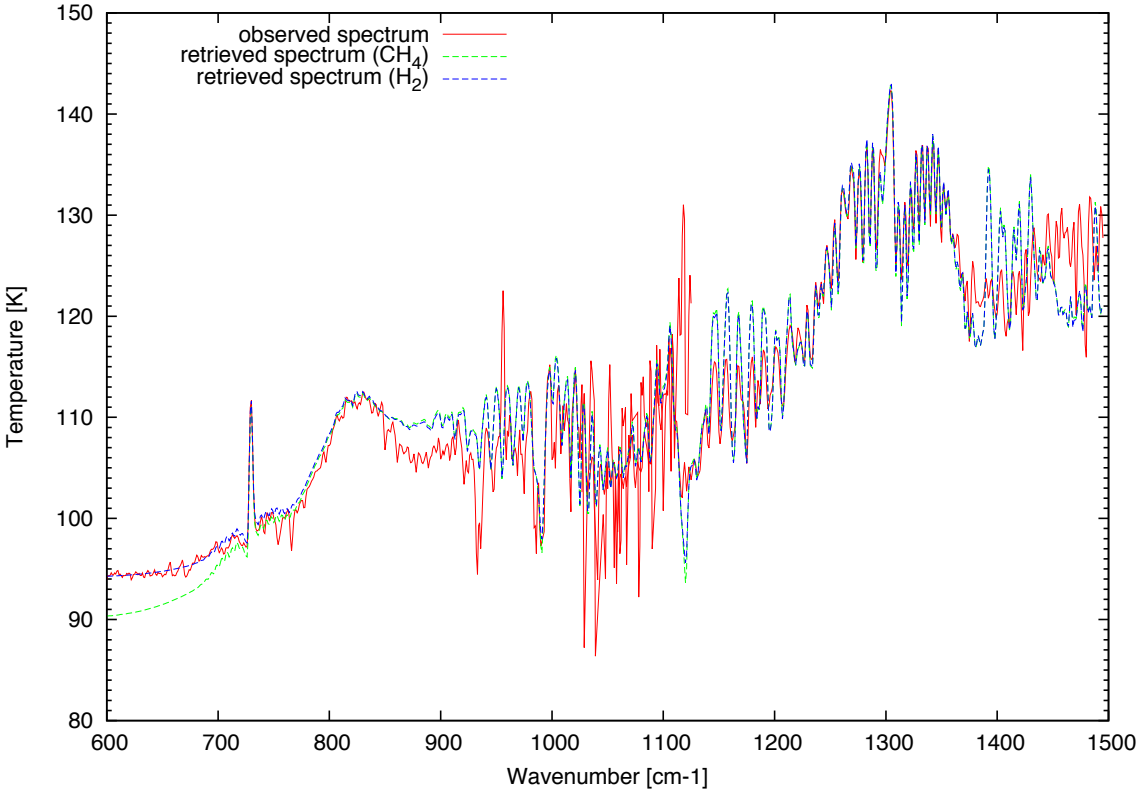

Figure 4-10. Spectrum at 27°S in 2005 after temperature retrieval.

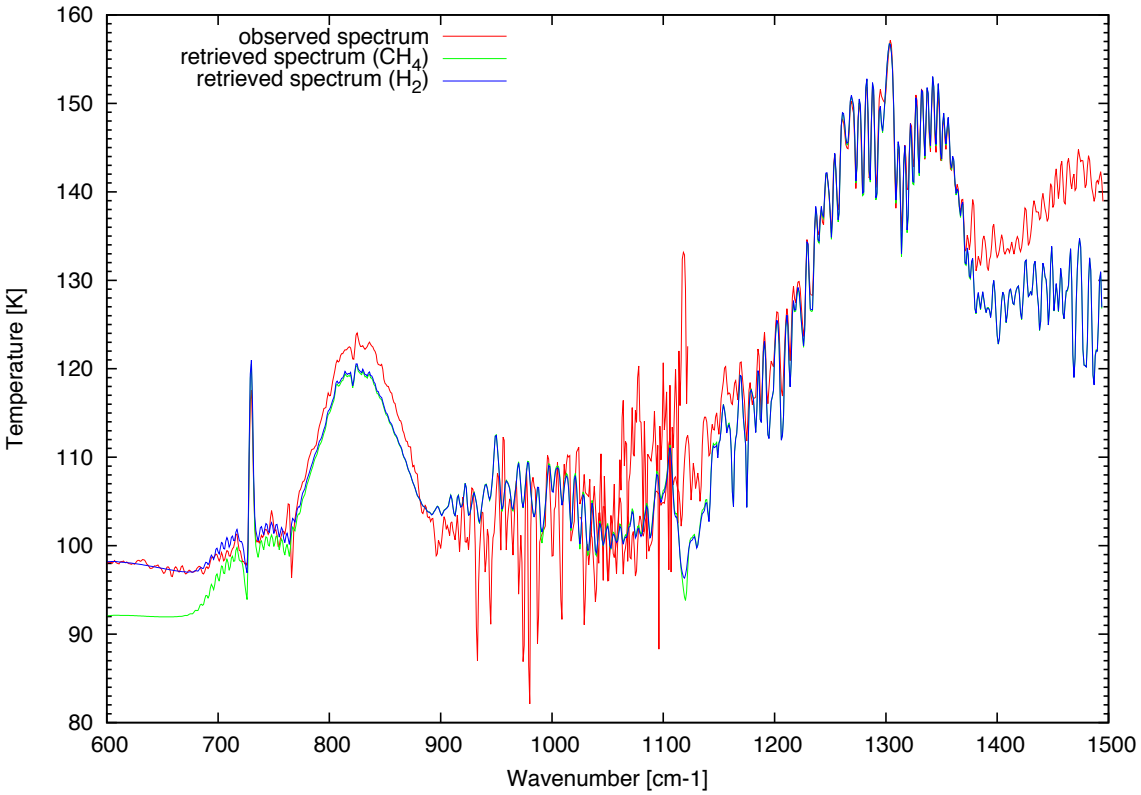

Figure 4-11. Spectrum at 77°S in 2005 after temperature retrieval.

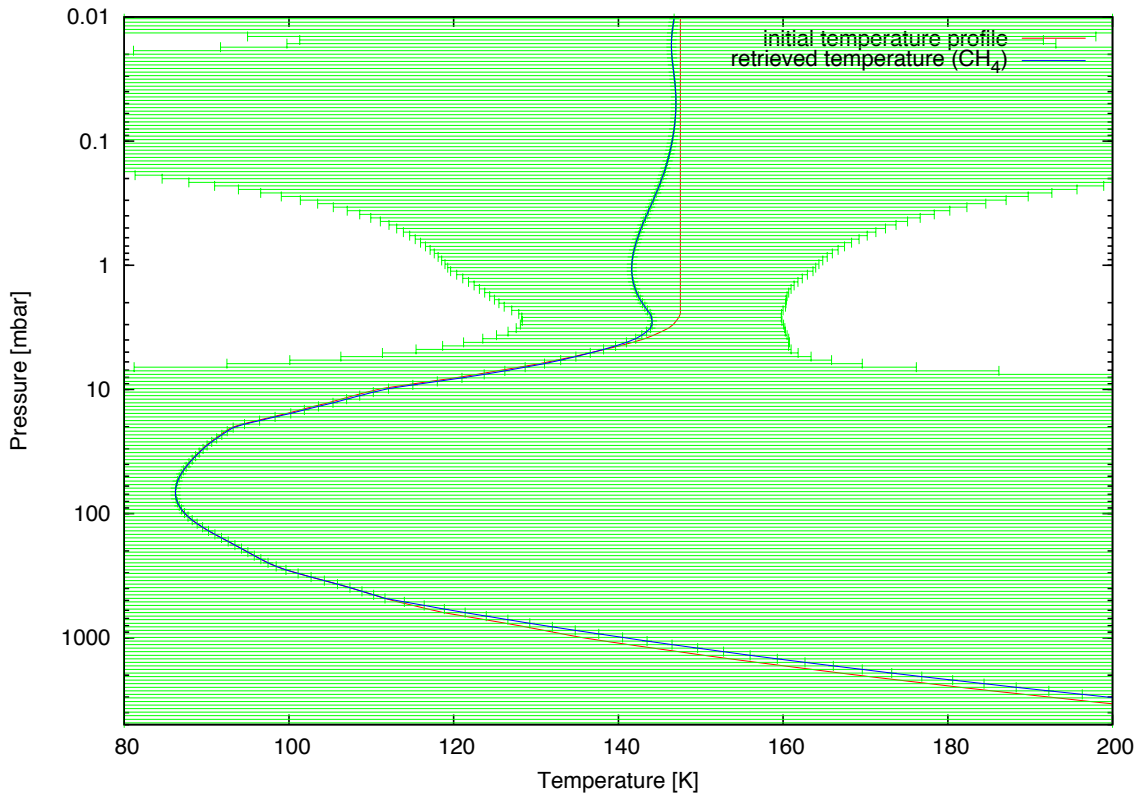

Figure 4-12. Temperature profile at 27°S in 2005 after the first stage of temperature retrieval.

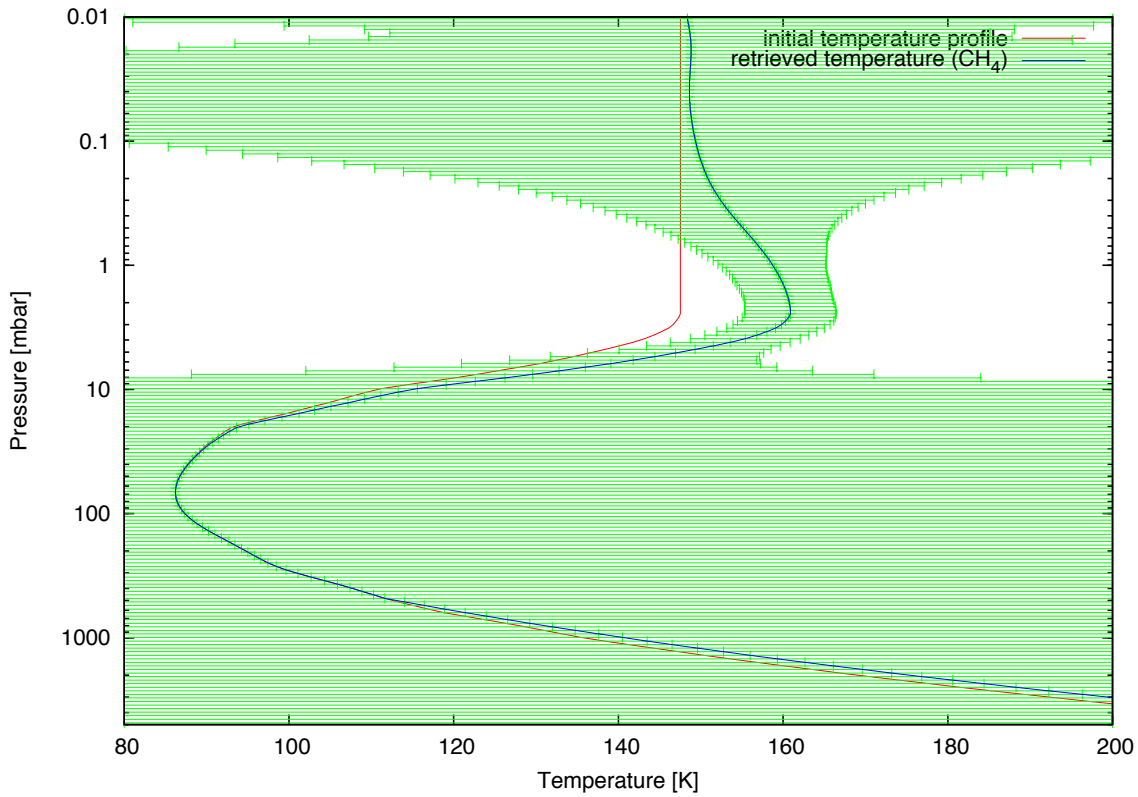

Figure 4-13. Temperature profile at 77°S in 2005 after the first stage of temperature retrieval.

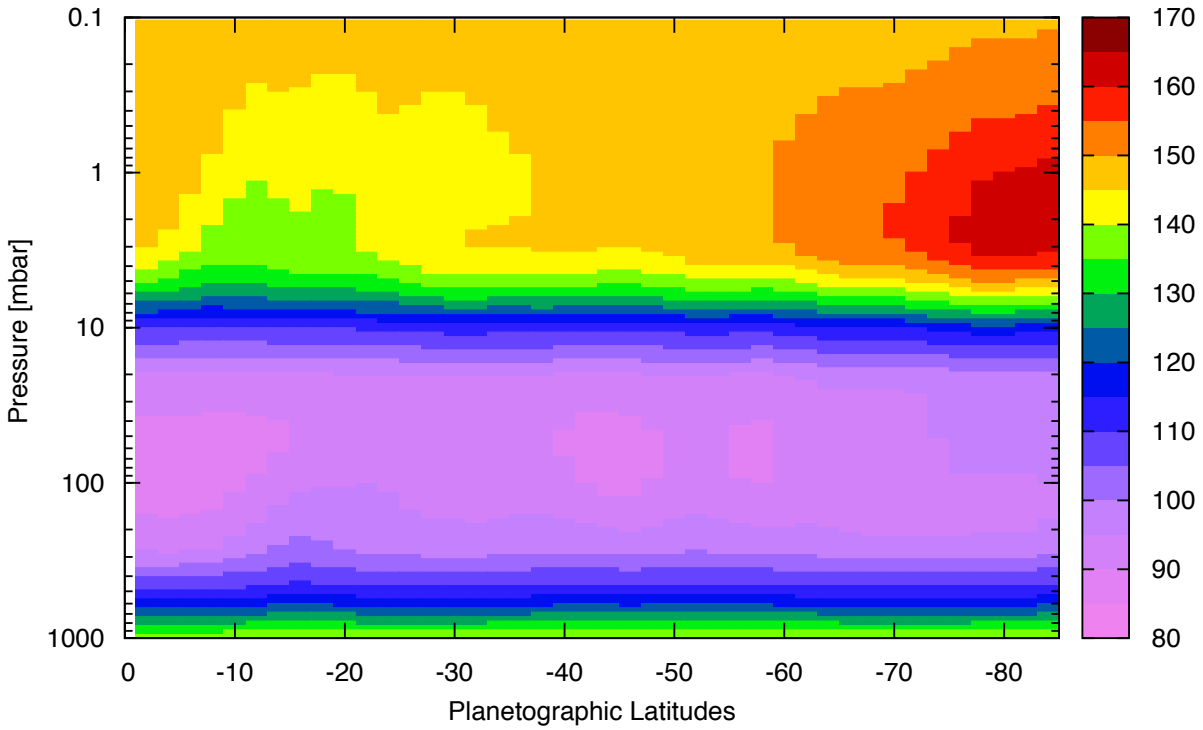

Figure 4-14. Retrieved temperature of southern hemisphere in 2005.

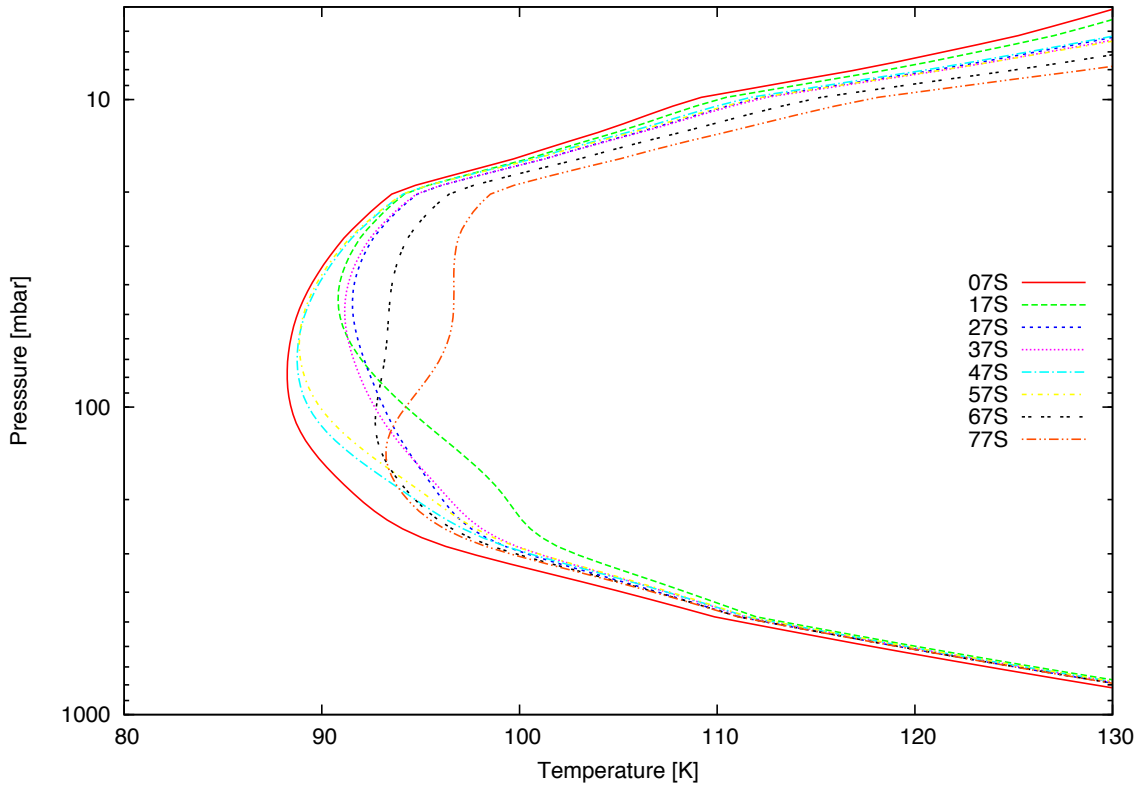

Figure 4-15. Retrieved tropospheric temperature knee in 2005.

CHAPTER 5
CLOUD RETRIEVAL

5.1 Introduction

The cloud retrieval is executed immediately after the temperature retrieval by using an identical algorithm described in Ch. 3 with different sets of inversion parameters[1] (c and γ) and initial profiles. The cloud retrieval code uses a Gaussian cloud profile and the retrieved temperature profile as initial conditions to generate a synthetic spectrum. The synthetic spectrum is then compared with the observed spectrum by Cassini/CIRS MIRMAP datasets in 2005 listed in Table 2-1.

In the cloud retrievals, we assume plane-parallel and a gray absorbing cloud with a dimensionless absorption coefficient $Y(z)$, where optical thickness of the cloud $\tau_c(z)$ at height z is defined as

$$\tau_c(z) = \int_z^\infty Y(z)\mathrm{d}z. \tag{5–1}$$

z is a dimensionless altitude defined as

$$z = -\ln \frac{p}{p_0} \tag{5–2}$$

with a reference altitude $z_0 = 0$ at $p_0 = 1000$ mbar. The dimensionless cloud absorption coefficient Y at pressure p is then calculated as

$$Y(p) = \begin{cases} -\frac{\mathrm{d}\tau_c}{\mathrm{d}\ln p}, & \text{if } p < p_0 \\ 0, & \text{if } p \geq p_0 \end{cases}. \tag{5–3}$$

The initial Gaussian cloud profile is parametrized with three adjustable variables : vertical broadness W, peak location of the initial cloud P, and the magnitude of the absorption coefficient A. The absorption coefficient of the initial Gaussian cloud is then

[1] c is the correlation parameter in scale height, and γ is the relative weight of the initial guess for the solution.

written as

$$Y_{initial} = A \exp \frac{-(\ln p - \log P)^2}{2W^2} \tag{5–4}$$

During each iteration, the retrieval code would modify the initial Gaussian cloud structure until the requirement set has been reached.

We solve for $\ln Y$ instead of Y to avoid possible unphysical solutions consistent with the mathematical problems. The functional derivative K for the retrieval of the cloud properties using the assumption in Conrath et al. (1998) and following Matcheva et al. (2005) is derived in Sec. 3.4.2 as

$$K_{ij} = Y(z_j)\frac{\Delta z}{\mu}\left[B(\nu_i,\, T(z_j))\, Tr(\mu, \nu_i, z_j) - \sum_{q=j}^{m} B(\nu_i,\, T(z_q))\Delta\, Tr(\mu, \nu_i, z_q)\right], \tag{5–5}$$

where $B(\nu_i,\, T(z_j))$ is the Planck radiance at temperature T at wavenumber ν_i, μ is the emission angle, and $Tr(\mu, \nu_i, z_j)$ is the transmittance at wavenumber ν_i at altitude z_j. The uncertainty of the retrieved absorption coefficient for clouds and haze at height z_j is

$$\varepsilon_{Y_j} = |\delta Y_j| = \frac{|Y_j|}{|K_{qj}|}\sqrt{\frac{\varepsilon^2_{NESR}}{N_w^2} + \frac{\varepsilon^2_{NESR}}{N_c^2}}, \tag{5–6}$$

$$j = 1, 2, \ldots n.$$

K_{qj} is the largest functional derivative amongst the layer j with the best sensitivity, N_w and N_c are the number of spectra for warm and cold calibrations respectively, and ε_{NESR} is the mean Noise Equivalent Spectral Radiance (NESR).

The spectral range for cloud retrieval is set to be 1389 - 1395 cm^{-1}, of which is a deep probing spectra region without influence of ammonia and phosphine. The volume mixing ratios and other atmospheric parameters are left the same as those in temperature retrievals.

5.2 Numerical Experiment

The validation of the retrieval algorithm for the clouds/haze has been tested in several numerical experiments similar with those in Matcheva et al. (2005). We inspect

the retrieval algorithm by using various sets of artificial test clouds of different geometric shapes (Gaussian cloud, rectangle cloud, and exponential cloud with flat base) at various heights and optical thicknesses. These test clouds are used to generate test spectra based on the retrieved temperature profile at 27°S in 2005. We then run the inversion code with initial Gaussian cloud profiles of different sets of parameters to fit the test spectra. By comparing the retrieved results with the test clouds, we would be able to investigate the correlation between the initial guess and the test clouds, allowing us to constrain the retrieved results for future retrievals when the real clouds/haze structure is not known.

Results of the numerical tests demonstrate that, if initial guesses covers the test cloud range, the cloud peak location can be successfully produced with small uncertainties by the retrieved cloud structures. In the regions where there exist weak cloud absorption (at high altitudes) or in an optically thick atmosphere (deep pressure levels), the spectral information alone is insufficient to drive the solution away from the initial guess. This occurrence results in large uncertainties at altitudes away from the cloud peaks. If the test cloud is located deeper at the pressure level where the atmospheric gas opacity is larger than unity, or if the test cloud itself is too thick, we may not be able to correctly retrieve the cloud peak and the optical thickness.

An example of a test cloud with optical thickness is defined as

$$\tau_{c,test}(p) = \begin{cases} \tau_{c_0}(p_0)(\frac{p}{p_0})^{H/H_c} & \text{if } p < p_0 \\ \tau_{c_0}(p_0) & \text{if } p \geq p_0 \end{cases}, \tag{5–7}$$

and it is shown as the red curve in Fig. 5-1 and Fig. 5-2. The reference pressure p_0 is 500 mbar, optical thickness τ_{c_0} is 1.0, and $H_c = 0.13H$. The base of the test cloud is at 500 mbar, the maximum absorption coefficient is 5, and the broadness is between 280 mbar and 500 mbar. The optical thickness of the test cloud increases with depth from 280 mbar and becomes unity at pressure greater than 500 mbar.

Fig. 5-1 and Fig. 5-2 also show the absorption coefficient Y and optical thickness τ_c of the initial guesses (green curves) and the retrieved results (blue curves) with uncertainties (gray zones). The results of an optically thick initial Gaussian cloud ($P = 1000$ mbar, $W = 0.6$, and $A = 2$) centered at 1 bar with a maximum cloud optical thickness $\tau_{c,max} = 3$ are shown in the top panels in both figures. The results of an optically thin initial Gaussian cloud ($P = 1000$ mbar, $W = 0.6$, and $A = 0.5$) centered at 1 bar with a maximum cloud optical thickness $\tau_{c,max} = 0.75$ are shown in the bottom panels in the figures. The orange horizontal dashed lines indicate the pressure level where the atmospheric opacity for 1392 cm^{-1} becomes unity without the presence of clouds/haze in nadir-viewing geometry. In the figures, one can see that the peak location of the test cloud is well produced by the retrieved cloud structures from both initial guesses. The retrieved optical thickness (blue curves) is also close to that of the test cloud as shown in Fig. 5-2.

Based on the results of the numerical experiments of the retrieval algorithm for clouds and haze, we are confident that our code has the capacity to derive the vertical profile of the cloud/haze with careful selections of the initial guess clouds.

5.3 χ^2 Minimization Approach

In order to examine the results from the cloud retrievals and gather information about the peak location as well as optical properties of the clouds/haze on Saturn, we also performed the χ^2 minimization approach by using a parametrized cloud structure to minimize the differences between the observed and the synthetic spectra.

A small χ^2 value reflects that the synthetic spectrum has a good fit to the observed spectrum. The calculated χ^2 value is defined as

$$\chi^2 = \frac{1}{N_\nu} \sum_{k=1}^{N_\nu} \frac{(x(\nu_k) - y(\nu_k))^2}{\sigma_x^2(\nu_k)}, \tag{5–8}$$

modified from Teanby et al. (2006). N_ν is the total number of wavenumber fitted in both spectra, $x(\nu_k)$ is the measured spectrum with variance $\sigma_x^2(\nu_k)$ at wavenumber ν_k, and

$y(\nu_k)$ is the synthetic spectrum at wavenumber ν_k. The variance $\sigma_x^2(\nu_k)$, which is defined in Equation 3–30, is calculated from the Noise Equivalent Spectral Radiance (NESR), the number of data averaged in the observed spectrum, the number of deep space calibrated spectra, and the number of the warm calibrated spectra.

In this work, we use the MIRMAP observations at 27°S on Saturn in 2005 to perform the χ^2 minimum approach. The parametrized cloud structure used to generate the synthetic spectrum is a combination of two Gaussian clouds with peaks at varying pressure levels (0.01 - 5000 mbar), widths (0.1 - 10), and amplitudes of dimensionless absorption coefficients (0 - 10). This six-parameter model is capable of simulating the atmosphere of only one cloud and no haze layers, as well as the atmosphere of one cloud and a haze layer with or without a separating layer of clear gas. A whole range survey for all six parameters with larger intervals was applied first to conserve a significant amount of computing time. After excluding combination sets of parameters with high χ^2 values, we calculate χ^2 values with smaller parameter intervals to obtain improved coverage.

Four groups of the cloud profiles provide small χ^2 values ($\approx$ 1.1) and are shown in Fig. 5-3. Type A cloud/haze (top left panel in Fig. 5-3) is a combination of a deeper broad cloud/haze layer and a thin haze layer located at higher altitudes. The stratospheric haze layer is at the pressure level between 0.01 and 2 mbar with a maximum absorption coefficient $Y = 0.1$. The tropospheric cloud spreads from 1 mbar to few thousand mbar with the peak absorption coefficient $Y = 2 \sim 3$ at around 1000 mbar. The cloud optical thickness increases slowly with depth starting between 0.01mbar and 1 mar, and the rate of increasing optical thickness suddenly changes at around few mbar, and become unity below 100 mbar. The stratospheric haze layer and the tropospheric clouds/haze layer might be separated by an aerosol free gap between 1 and 10 mbar. Type B clouds/haze (top right panel in Fig. 5-3) is a broad cloud layer ranging from 1 mbar to few thousand mbar, and its optical thickness is larger than unity

at pressure levels greater than few hundred mbar. Type C clouds/haze (bottom left panel in Fig. 5-3) is similar to Type B clouds/haze profile with the maximum absorption coefficient $Y = 1 \sim 3$ at 300 $\sim$ 500 mbar. Type D clouds/haze (bottom right panel in Fig. 5-3) is a deep broad clouds/haze layer located in troposphere extending from 0.1 mbar to few thousand mbar. The optical thickness increases slowly from 0.1 mbar and becomes 0.1 at the pressure level between 1 mar and 10 mbar; it then increases rapidly with depth between 10 mbar and 100 mbar. Near the tropopause, the optical thickness becomes unity.

Although the χ^2 minimization approach does not show the real clouds/haze structure in the atmosphere of Saturn, it still provides information about the vertical distribution at the latitudes of interest. The results of the χ^2 minimization approach at 27°S in the southern hemisphere based on 2005 observations suggest that there may be a deep broad clouds/haze layer with unknown chemical composition that extends from the lower stratosphere at the pressure about few mbar to the troposphere with the optical thickness $\tau_c = 1 \sim 10$ between 100 mbar and 5000 mbar. A possible optically thin haze layer may be located between 1 and 10 mbar on the top of the broad tropospheric cloud layer.

5.4 Cloud Retrieval Results and Discussion

As mentioned in Sec. 2.2.4.2, the higher than expected brightness temperature at latitudes higher than 70°S in the southern hemisphere in 2005 may be attributed to the presence of clouds or haze in the stratosphere. The lower than expected brightness temperature at mid- and low latitudes can be explained by the cloud layer in the upper troposphere. In this work, we perform the cloud inversion at 27°S to examine this assumption.

Fig. 5-4 to Fig. 5-6 show the retrieved results of different sets of initial parameters (peak location P, magnitude of the absorption coefficient A, and the vertical broadness W). In each of these figures, the initial cloud profiles are shown as thin solid lines,

and the retrieved absorption coefficient (left panels) and the retrieved optical thickness (right panels) are shown as thick solid lines. As we can see in these figures, an aerosol layer located at upper troposphere between 10 mbar and 700 mbar is developed during iterations. The peak location of the retrieved cloud structure may be located at pressure between 20 mbar and 500 mbar as seen in Fig. 5-6. In Fig. 5-4, a feature with a small absorption coefficient is also developed at around 4 mbar (blue lines), which may indicate that a stratospheric haze layer is located at few mbars.

Discussion. Our retrieved results show that there are two types of possible vertical distributions of the clouds and haze at 27°S in 2005. One possible cloud distribution contains a broad aerosol layer located below the tropopause at 100 mbar and extends to deeper pressure region at few thousand mbars. This vertical distribution of the tropospheric cloud/haze is consistent with previous observations (Karkoschka and Tomasko, 1993; West, 1983). The other possible cloud distribution includes the tropospheric aerosol layer and an optically thin haze layer in the stratosphere between 0.01 mbar and 10 mbar, which is consistent with the observations by Stam et al. (2001) and Karkoschka and Tomasko (1993).

However, the uncertainties of the retrieved clouds/haze profiles are large, as shown in Fig. 5-7, therefore, the results cannot be well-constrained. The uncertainties for cloud/haze retrievals can be due to the data quality issues discussed in Sec. 2.2.4.3 in the spectral range between 1389 cm^{-1} and 1395 cm^{-1}. We also noticed that the height of the retrieved cloud peak appears to have some correlation with the peak locations of the initial cloud profiles, which shows that the retrieved results may be model-dependant.

As shown in Fig. 5-8, when comparing the observed spectrum with the synthetic spectra after temperature and clouds/haze retrievals, one can see the synthetic spectrum after clouds/haze retrieval can fit the observed spectrum within the narrow spectral window centered at 1392 cm^{-1} with small χ^2 values. However, the synthetic spectrum after clouds/haze retrieval does not fit the observed spectrum in the neighboring

spectral region well. One possible explanation of this failure to fit the neighboring spectral region can be due to the lack of information of the ethane (C_2H_6) absorption coefficient within this spectral range in the retrieval code.

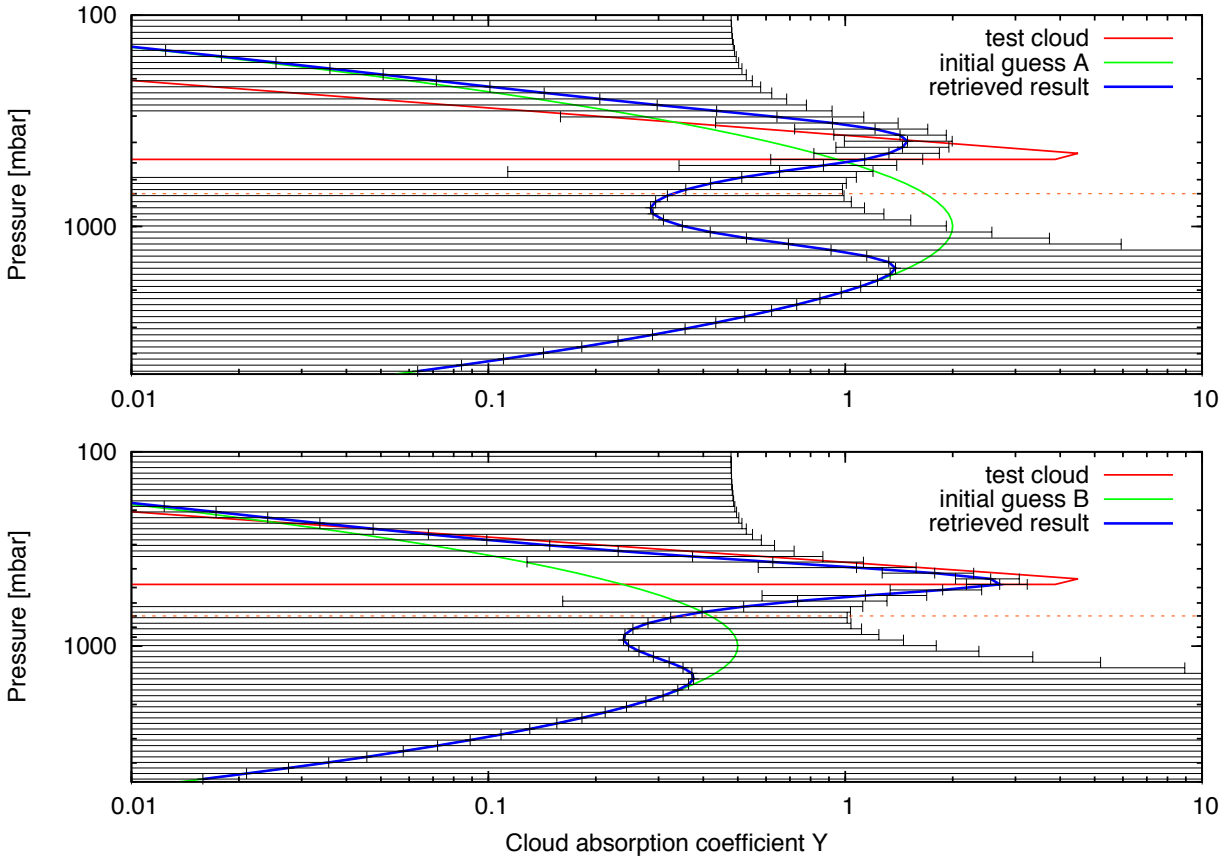

Figure 5-1. Cloud absorption coefficient of the numerical experiment.

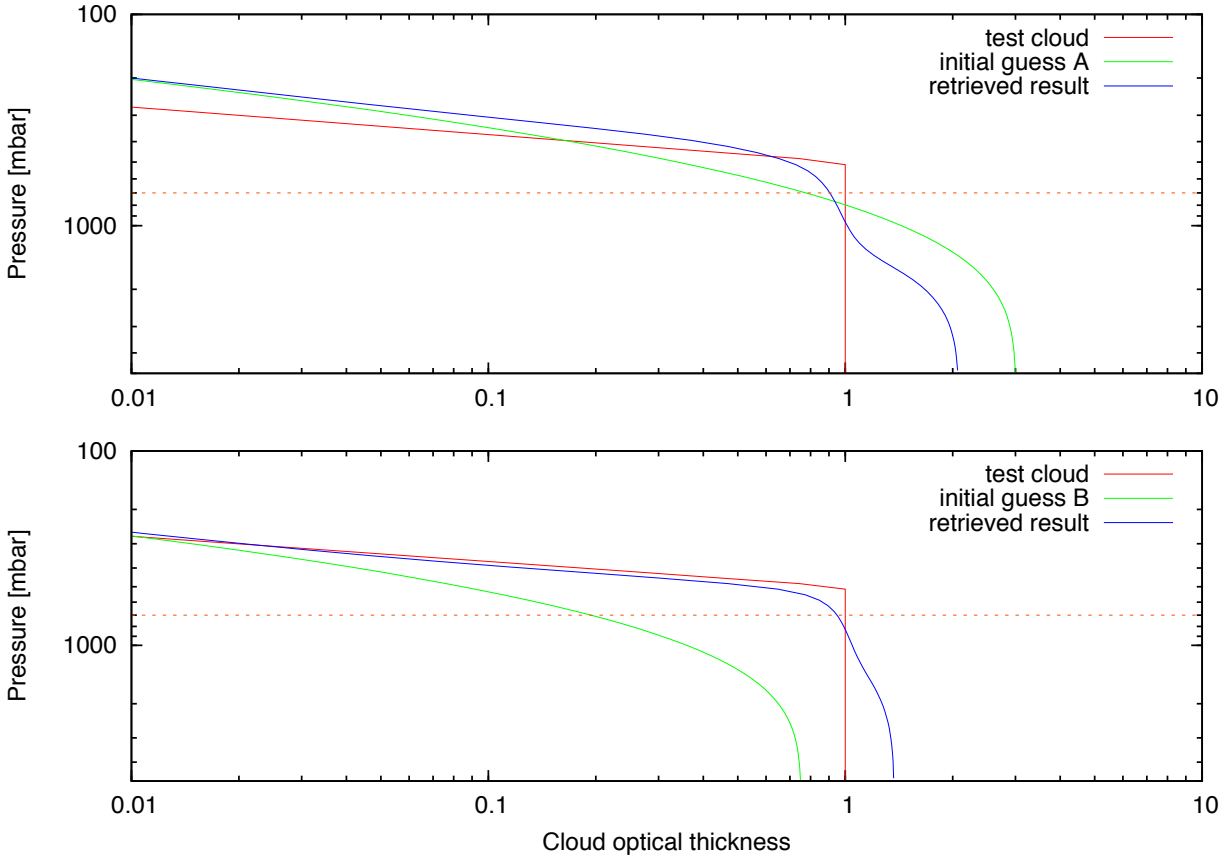

Figure 5-2. Optical thickness of the numerical experiment.

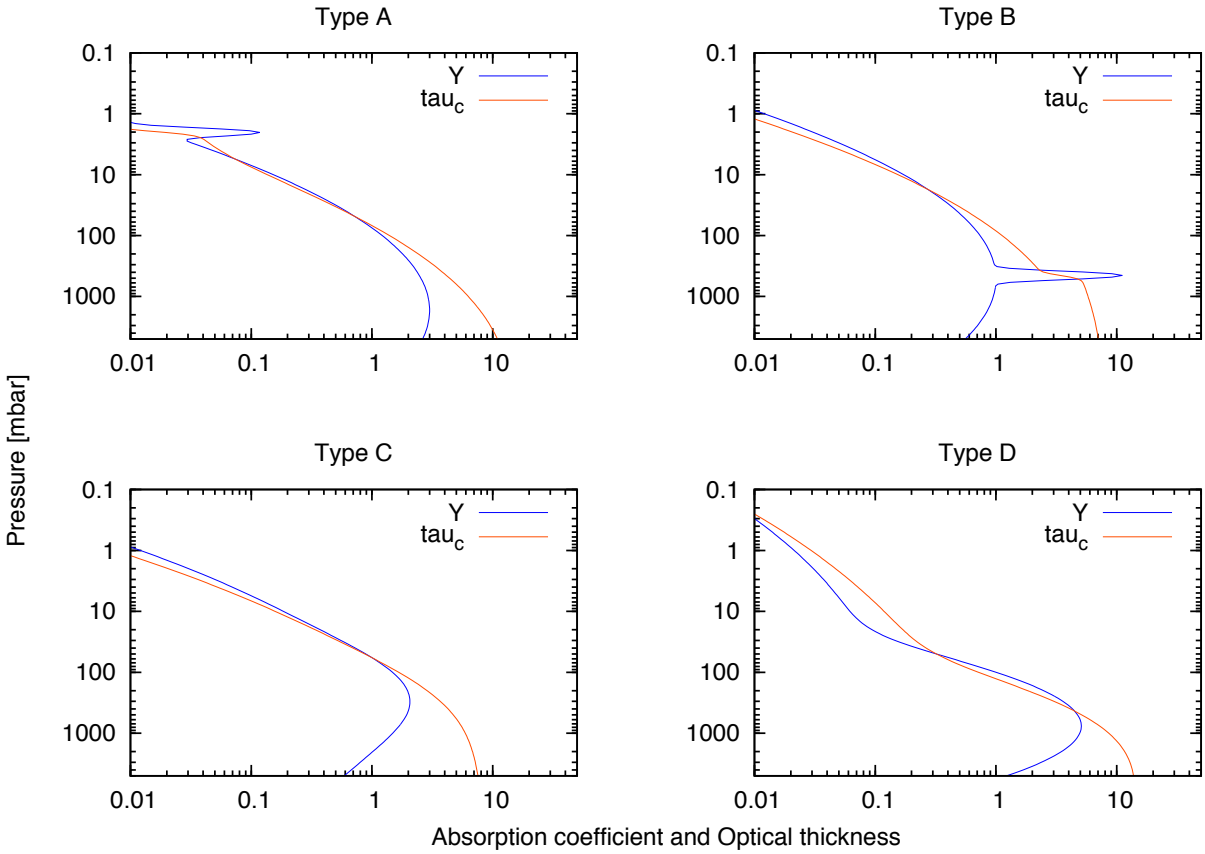

Figure 5-3. Results of χ^2 minimization approach.

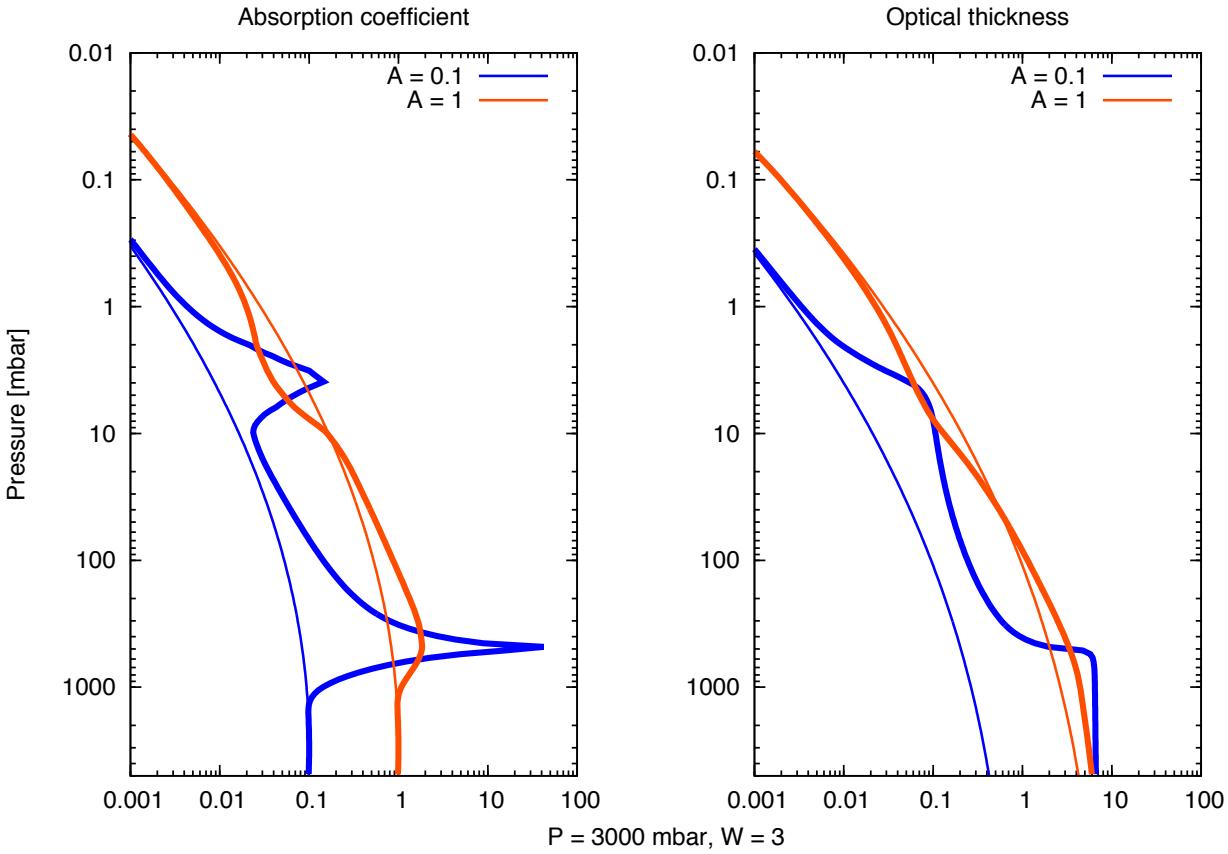

Figure 5-4. Cloud retrieval results (a).

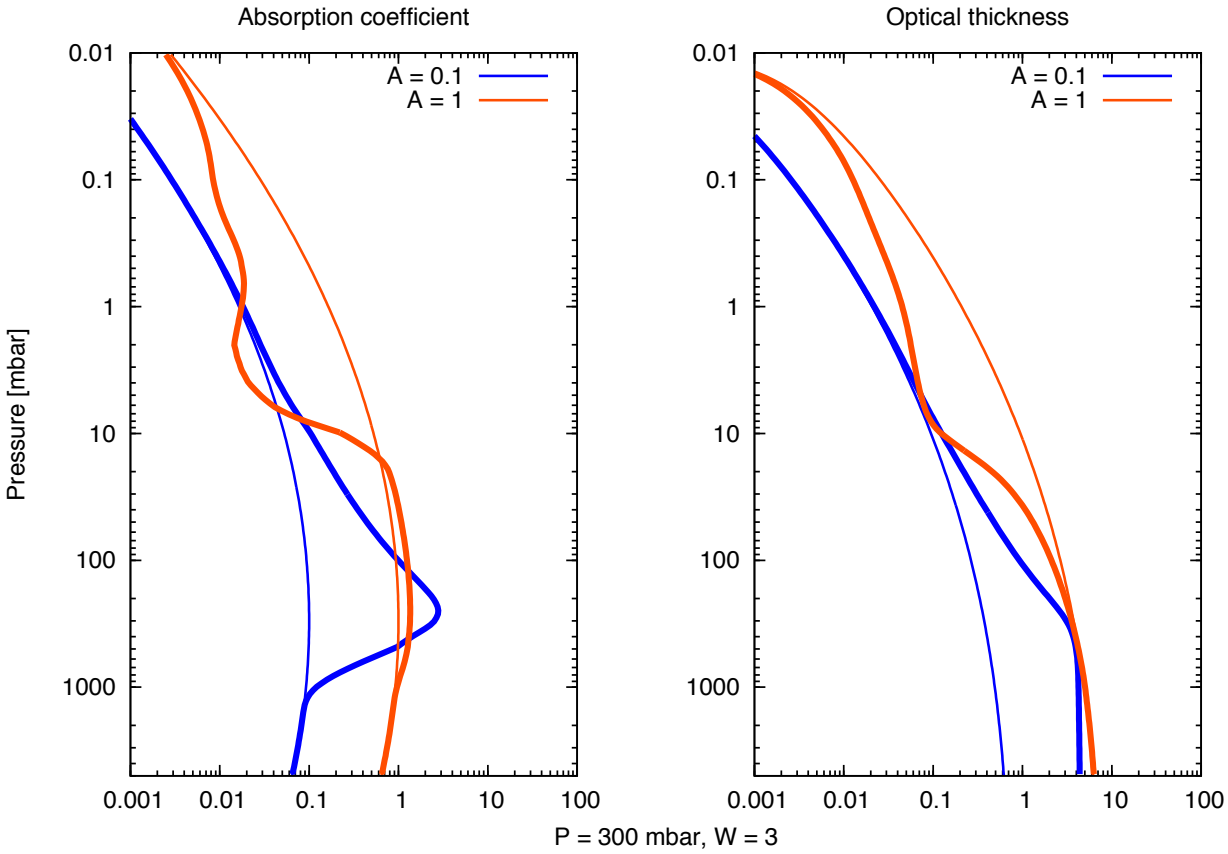

Figure 5-5. Cloud retrieval results (b).

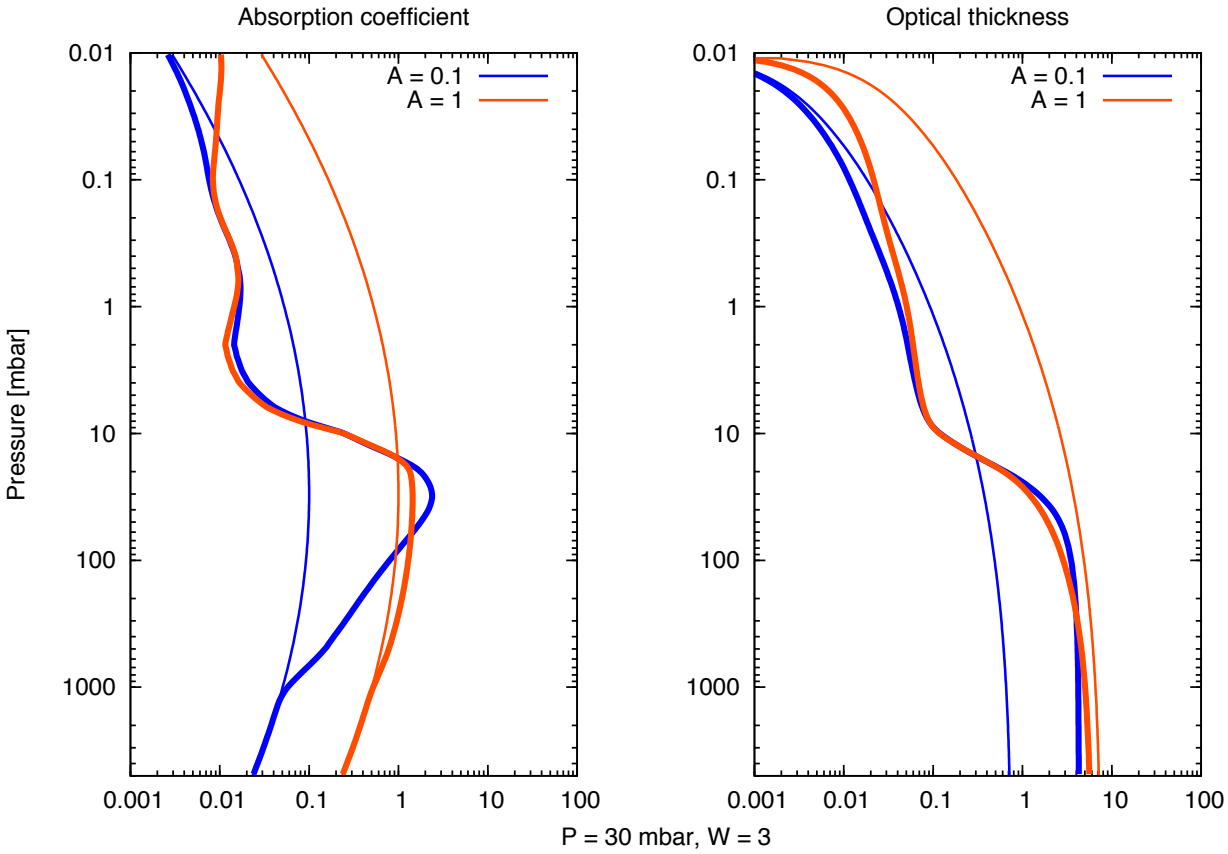

Figure 5-6. Cloud retrieval results (c)

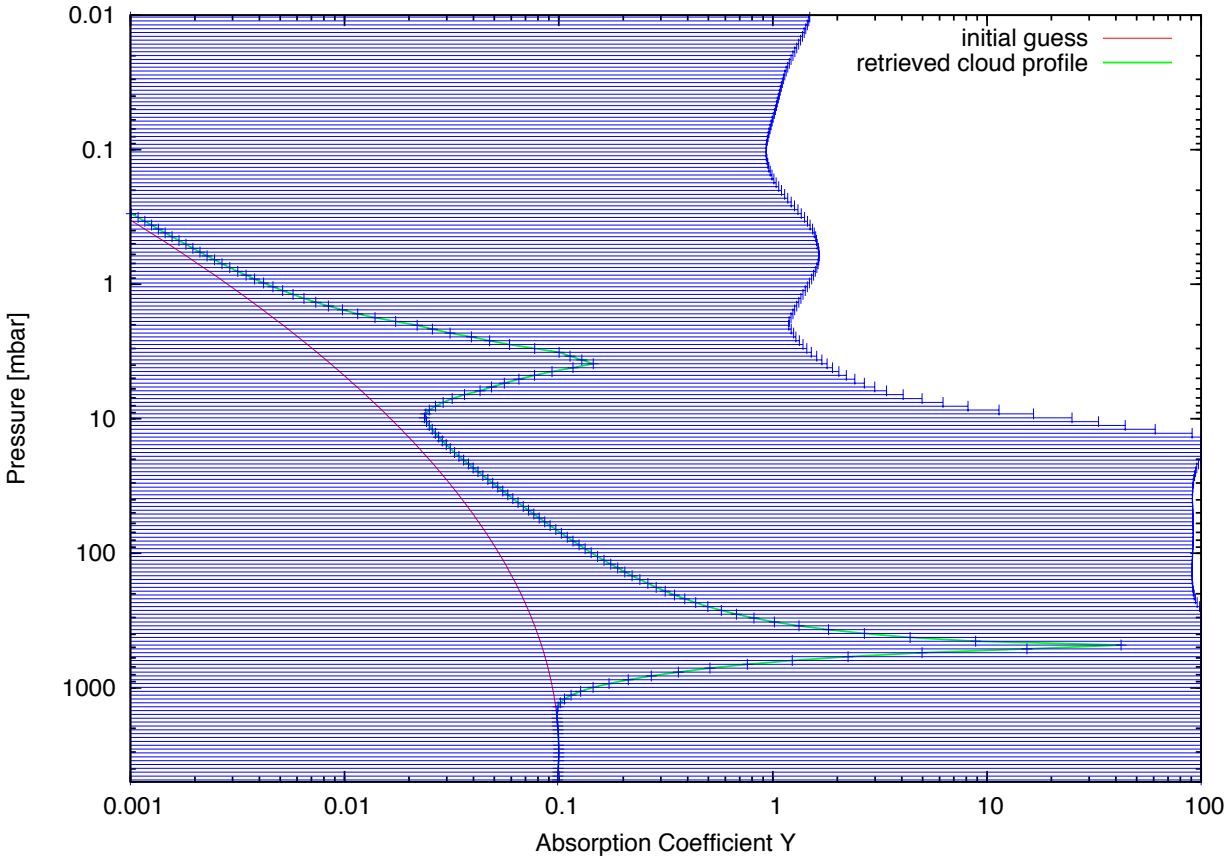

Figure 5-7. Retrieved cloud with uncertainties.

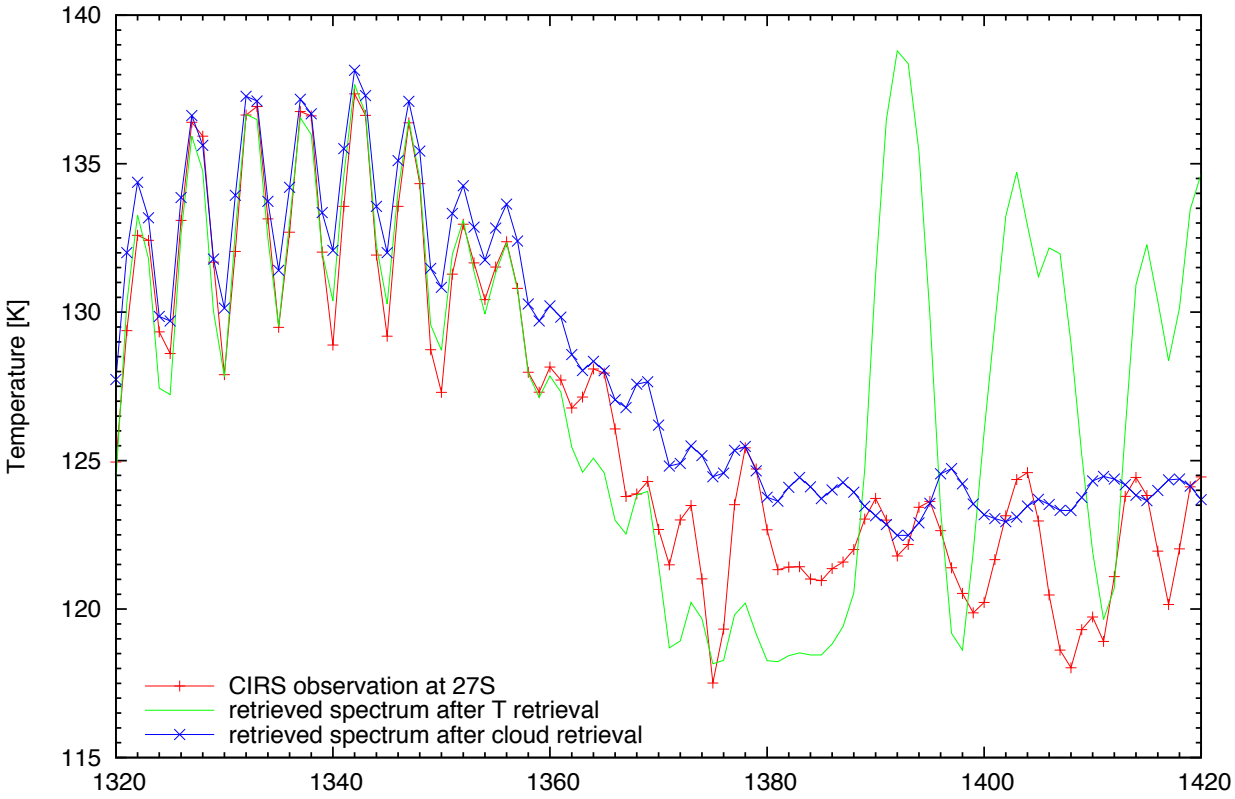

Figure 5-8. Spectrum of the retrieved cloud.

CHAPTER 6
SUMMARY

The pre-Cassini knowledge of the vertical distributions of clouds and haze on Saturn is primarily derived from ground-based and space-based observations as well as spacecraft missions such as Voyager 1 and Voyager 2. The common cloud and haze structures seen in numerous studies include : (a) three cloud layers at the pressure level deeper than 1 bar, (b) a tropospheric haze layer between the top ammonia ice cloud layer and the tropopause near 100 mbar, and (c) a stratospheric haze layer at the pressure level between 1 mbar and 100 mbar. In this work, we use the Cassini/CIRS mid-infrared data to analyze the optical properties of the clouds and haze on Saturn to provide an alternative study of the atmospheric structure.

We first perform the sensitivity study of the MIRMAP datasets from 2005 to 2008 obtained during the Cassini Prime Mission. We also construct yearly brightness temperature maps to examine the global and latitudinal brightness temperature variations at 1392 cm^{-1}. The correlation of the data quality at 1392 cm^{-1} and the calibration sequences is also discussed in this dissertation.

We develop the retrieval algorithm for temperate and clouds/haze inversions. The retrieval algorithm includes a forward model, calculations of the functional derivative matrix and error analysis. The main function of the forward model is to describe the physics of the problem. The correlated-k method is used as the forward model to balance the accuracy and the computational efficiency. We use artificial cloud structures to test the validation of the retrieval algorithm and to examine the correlation of the retrieved results and the initial parameters. χ^2 minimization approach is also applied to obtain information of the possible peak location and the optical properties of the cloud/haze structure for the retrievals.

Temperature Retrievals. Our retrieved temperature profiles in the southern hemisphere in 2005 show that : (a) the stratospheric temperature at the pressure level

between 0.3 mbar and 5 mbar is between 140 K - 150 K in the low and mid-latitudes, and the temperature is slightly increasing toward the equator; (b) the stratospheric temperature elevates from mid-latitudes toward the southern polar region, and the temperature at the polar region is about 15 K - 20 K warmer than that at the equator around 2 mbar pressure level; (c) for pressure level below 5 mbar, there is no obvious latitudinal variation of the retrieved temperature; (d) The temperature at tropopause near 100 mbar is between 88 K and 95 K for all latitudes in the southern summer hemisphere in 2005.

Our results are consistent with the temperature structure analysis of CIRS data by Flasar et al. (2005) and Fletcher et al. (2007). Tropospheric temperature knee (Fletcher et al., 2007; Hanel et al., 1981; 1982) in the retrieved temperature profiles is also discussed in Chapter 4.

Clouds and Haze Retrievals. We use 2005 MIRMAP CIRS observations at 27°S for clouds and haze retrievals. Features in our results show that : (a) an optically thick aerosol layer is developed at the pressure level between 10 mbar and 700 mbar; (b) the peak location of the tropospheric aerosol layer is located at pressure between 20 mbar and 500 mbar; (c) a possible stratospheric haze layer with small optical thickness is also seen at few mbars.

Our retrieved vertical distribution of the tropospheric haze layer derived from Cassini mid-infrared data is consistent with the previous observations by Karkoschka and Tomasko (1993) and West (1983). The other possible cloud/haze distribution with a tropospheric haze layer and a stratospheric haze layer is consistent with the observations by Stam et al. (2001) and Karkoschka and Tomasko (1993).

Discussion. Our work provides the analysis of the vertical distribution of clouds and haze in the southern summer hemisphere on Saturn by using the Cassini/CIRS mid-infrared datasets. This work also provides a foundation for future clouds and haze research on gas giants by using mid-infrared data. To improve our understanding of

the vertical distribution of the cloud and haze profiles on Saturn, several tasks can be done for future reference : (a) An inclusion of an up-to-date absorption coefficient of chemical compounds within the spectral range of interest, such as ethane (C_2H_6) emission between 1300 cm^{-1} and 1400 cm^{-1} may improve the fitting of the observed and retrieved spectra; (b) for more accurate temperature retrievals, information of other atmospheric properties, such as the ortho/para-H_2 ratio, is imperative; (c) the CIRS data released in the future with improved calibration methods should be able to decrease the uncertainties of the retrieved results and provide better resolution for clouds and haze retrievals; (d) data from different Cassini instruments at different spectral regions (UV, infrared, and visible) can be taken into account in the retrieval code to study seasonal and latitudinal variations of clouds/haze and atmospheric composition.

REFERENCES

Anderson, J., Schubert, G., 2007. Saturn's gravitational field, internal rotation, and interior structure. Science 317, 1384.

Atreya, S., Wong, A.-S., 2005. Coupled clouds and chemistry of the giant planets a case for multiprobes. Space Science Reviews 116, 121–136.

Atreya, S., Wong, M., Owen, T., Mahaffy, P., Niemann, H., de Pater, I., Drossart, P., Encrenaz, T., 1999. A comparison of the atmospheres of jupiter and saturn: deep atmospheric composition, cloud structure, vertical mixing, and origin. Planetary and Space Science 47, 1243–1262.

Bzard, B., Gautier, D., Conrath, B., 1984. A seasonal model of the saturnian upper troposphere comparison with voyager infrared measurements. Icarus 60, 274–288.

Carlson, R. C., 2001. Radiometric calibration method using interferogram differencing and complex spectra. PDS archive co-s-cirs-234-tsdr-v31.

Cassini/CIRS, 2012. Cassini cirs data. PDS archive co-s-cirs-234-tsdr-v31.

Cess, R., Caldwell, J., 1979. A saturnian stratospheric seasonal climate model. Icarus 38, 349–357.

Conrath, B., Gautier, D., 2000. Saturn helium abundance: A reanalysis of voyager measurements. Icarus 144, 124–134.

Conrath, B., Gierasch, P., Ustinov, E., 1998. Thermal structure and para- hydrogen fraction on the outer planets from voyager iris measurements. Icarus 135, 501–517.

Conrath, B., Pirraglia, J., 1983. Thermal structure of saturn from voyager infrared measurementsimplications for atmospheric dynamics. Icarus 53, 286–292.

Courtin, R., Gautier, D., Marten, A., Bzard, B., Hanel, R., 1984. The composition of saturns atmosphere at northern temperate latitudes from voyager iris spectranh3 , ph3 , c2 h2 , c2 h6 , ch3 d, ch4 , and the saturnian d/h isotopic ratio. Astrophys. J. 287, 899–916.

Flasar, F., Achterberg, R., Conrath, B., Pearl, J., Bjoraker, G., Jennings, D., Romani, P., Simon-Miller, A., Kunde, V., Nixon, C., Bzard, B., Orton, G., Spilker, L., Spencer, J., Irwin, P., Teanby, N., Owen, T., Brasunas, J., Segura, M., Carlson, R., Mamoutkine, A., Gierasch, P., Schinder, P., Showalter, M., Ferrari, C., Barucci, A., Courtin, R., Coustenis, A., Fouchet, T., Gautier, D., Lellouch, E., Marten, A., Prang, R., Strobel, D., Calcutt, S., Read, P., Taylor, F., Bowles, N., Samuelson, R., Abbas, M., Raulin, F., Ade, P., Edgington, S., Pilorz, S., Wallis, B., Wishnow, E., 2005. Temperatures, winds, and composition in the saturnian system. Science 307, 1247–1251.

Flasar, F., Kunde, V., Abbas, M., Achterberg, R., Ade, P., Barucci, A., Bzard, B., Bjoraker, G., Brasunas, J., Calcutt, S., Carlson, R., Csarsky, C., Conrath, B., Coradini, A.,

Courtin, R., Coustenis, A., Edberg, S., Edgington, S., Ferrari, C., Fouchet, T., Gautier, D., Gierasch, P., Grossman, K., Irwin, P., Jennings, D., Lellouch, E., Mamoutkine, A., Marten, A., Meyer, J., Nixon, C., Orton, G., Owen, T., Pearl, J., Prang, R., Raulin, F., Read, P., Romani, P., Samuelson, R., Segura, M., Showalter, M., Simon-Miller, A., Smith, M., Spencer, J., Spilker, L., Taylor, F., 2004. Exploring the saturn system in the thermal infrared: The composite infrared spectrometer. Space Sci. Rev. 115, 169–297.

Fletcher, L., G.S., O., N.A., T., andJ., I. P., 2009. Phosphine on jupiter and saturn from cassini/cirs. Icarus 2009, 543–564.

Fletcher, L., Orton, G., Teanby, N., Irwin, P., Bjoraker, G., 2009. Methane and its isotopologues on saturn from cassini/cirs observations. Icarus 199, 351–367.

Fletcher, L. N., Irwin, P., Teanby, N., Orton, G., Parrish, P., de Kok, R., Howett, C., Calcutt, S., Bowles, N., Taylor, F., 2007. Characterising saturns vertical temperature structure from cassini/cirs. Icarus 189, 457–478.

Fouchet, T., Moses, J., Conrath, B., 2009. *Saturn : Composition and chemistry. Saturn from Cassini-Huygens*.

Goody, R., West, R., Chen, L., Crisp, D., 1989. The correlated-k method for radiation calculations in nonhomogeneous atmospheres. Journal of Quantitative Spectroscopy and Radiative Transfer 42, 539–550.

Hanel, R., Conrath, B., Flasar, F., Kunde, V., Maguire, W., Pearl, J., Pirraglia, J., Samuelson, R., Herath, L., Allison, M., Cruikshank, D., Gautier, D., Gierasch, P., Horn, L., Koppany, R., Ponnamperuma, C., 1981. Infrared observations of the saturnian system from voyager 1. Science 212, 192–200.

Hanel, R., Crosby, D., Herath, L., Vanous, D., Collins, D., Creswick, H., Harris, C., Rhodes, M., 1982. Infrared spectrometer for voyager. Appl. Opt. 19 19, 1391–1400.

Irwin, P., 2009. *Giant planets of our solar system - Atmospheres, composition, and structure, 2nd ed.* ISBN : 978-3-540-85157-8.

Irwin, P., Calcutt, S., Sihra, K., Taylor, F., Weir, A., Ballard, J., Johnston, W., 1999. Band parameters and k coefficients for self-broadened ammonia in the range 4000-11000 cm^{-1}. Journal of Quantitative Spectroscopy and Radiative Transfer 62, 193–204.

Irwin, P., Sromovsky, L., Strong, E., Sihra, K., Teanby, N., Bowles, N., Calcutt, S., Remedios, J., 2006. Improved near-infrared methane band models and k-distribution parameters from 2000 to 9500 cm^{-1} and implications for interpretation of outer planet spectra. Icarus 181, 309–319.

Irwin, P., Teanby, N., de Kok, R., Fletcher, L., Howett, C., Tsang, C., Wilson, C., Calcutt, S., Nixon, C., Parrish, P., 2008. The nemesis planetary atmosphere radiative transfer

and retrieval tool. Journal of Quantitative Spectroscopy and Radiative Transfer 109, 1136–1150.

Jacquinet-Husson, N., Scott, N., Chedin, A., Garceran, K., Armante, R., Chursin, A., Barbe, A., Birk, M., Brown, L., Camy-Peyret, C., Claveau, C., Clerbaux, C., Coheur, P., Dana, V., Daumont, L., Debacker-Barilly, M., Flaud, J., Goldman, A., Hamdouni, A., Hess, M., Jacquemart, D., Kopke, P., Mandin, J., Massie, S., Mikhailenko, S., Nemtchinov, V., Nikitin, A., Newnham, D., Perrin, A., Perevalov, V., Regalia-Jarlot, L., Rublev, A., Schreier, F., Schult, I., Smith, K., Tashkun, S., Teffo, J., Toth, R., Tyuterev, V., Vander Auwera, J., Varanasi, P., G., W., 2005. The 2003 edition of the geisa/iasi spectroscopic database. Journal of Quantitative Spectroscopy and Radiative Transfer 95, 429–467.

Karkoschka, E., Tomasko, M., 1992. Saturns upper troposphere 19861989. Icarus 97, 161–181.

Karkoschka, E., Tomasko, M., 1993. Saturns upper atmospheric hazes observed by the hubble space telescope. Icarus 106, 428–441.

Karkoschka, E., Tomasko, M., 2005. Saturns vertical and latitudinal cloud structure 19912004 from hst imaging in 30 filters. Icarus 179, 195–221.

Kerola, D., Larson, H., Tomasko, M., 1997. Analysis of the near-ir spectrum of saturn: A comprehensive radiative transfer model of its middle and upper troposphere. Icarus 127, 190–212.

Lacis, A., Oinas, V., 1991. A description of the correlated k distribution method for modeling nongray gaseous absorption, thermal emission, and multiple scattering in vertically inhomogeneous atmospheres. Journal of Geophysical Research 96, 9027–9063.

Liou, K., 2002. *An introduction to atmospheric radiation* (2 ed.), Volume 84. ISBN : 0-12-451-451-0.

Matcheva, K., Conrath, B., Gierasch, P., Flasar, F., 2005. The cloud structure of the jovian atmosphere as seen by the cassini/cirs experiment. Icarus 179, 432–448.

Moses, J., Greathouse, T., 2005. Latitudinal and seasonal models of stratospheric photochemistry on saturn: Comparison with infrared data from irtf/texes. Journal of Geophysical Research 110, E09007.

Munoz, O., Moreno, F., Molina, A., Grodent, D., Grard, J., Dols, V., 2004. Study of the vertical structure of saturns atmosphere using hst/wfpc2 images. Icarus 169, 413–428.

Nixon, C., 2011. Cassini composite infrared spectrometer (cirs) : Planetary data system, (pds) time sequential data record (tsdr), data product software interface specification (sis). io-ar-002. PDS archive co-s-cirs-234-tsdr-v31.

Ortiz, J., Moreno, F., Molina, A., 1996. Saturn 19911996: Clouds and hazes. Icarus 119, 53–66.

Orton, G., Serabyn, E., Lee, Y., 2000. Vertical distribution of ph3 in saturn from bbservations of its 1-0 and 3-2 rotational lines. Icarus 146, 48–59.

Orton, G., Serabyn, E., Lee, Y., 2001. Erratum, volume 146, number 1, pages 48-59 (2000), in the article “vertical distribution of ph3 in saturn from observations of its 1-0 and 3-2 rotational lines. Icarus 149, 489–490.

Rodgers, C., 1976. Retrieval of atmospheric temperature and composition from remote measurements of thermal radiation. Review of Geophysics and space physics 14, 609–624.

Rodgers, C., 2000. *Inverse methods for atmospheric sounding : Theory and practice*. ISBN :13 978-981-02-2740-1.

Rodgers, C., Connor, B., 2003. Intercomparison of remote sounding instruments. Journal of Geophysical Research 108, 4116.

Rothman, L., Jacquemart, D., Barbe, A., Chris Benner, D., Birk, M., Brown, L., Carleer, M., Chackerian Jr., C., Chance, K., Coudert, L., Dana, V., Devi, V., Flaud, J.-M., Gamache, R., Goldman, A., Hartmann, J.-M., Jucks, K., Maki, A., Mandin, J.-Y., Massie, S., Orphal, J., Perrin, A., Rinsland, C., Smith, M., Tennyson, J., Tolchenov, R., Toth, R., Vander Auwera, J., Varanasi, P., Wagner, G., 2005. The hitran 2004 molecular spectroscopic database. Journal of Quantitative Spectroscopy and Radiative Transfer 96, 134–204.

Stam, D., Banfield, D., Gierasch, P., Nicholson, P., Matthews, K., 2001. Near-ir spectrophotometry of saturnian aerosols-meridional and vertical distribution. Icarus 152, 407–422.

Teanby, N., L.N., F., P.G.J., I., Fouchet, T., Orton, G., 2006. New upper limits for hydrogen halides on saturn derived from cassini-cirs data. Icarus 185, 466–475.

Temma, T., Chanover, N., Simon-Miller, A., Glenar, D., Hillman, J., Kuehn, D., 2005. Vertical structure modeling of saturns equatorial region using high spectral resolution imaging. Icarus 175, 464–489.

Weidenschilling, S., Lewis, J., 1973. Atmospheric and cloud structures of the jovian planets. Icarus 20, 465–476.

West, R., 1983. Spatially resolved methane band photometry of saturn: Ii. cloud structure models at four latitudes. Icarus 53, 301–309.

Williams, D., 2012. Saturn fact sheet, national space science data center, nas. http://nssdc.gsfc.nasa.gov/planetary/factsheet/saturnfact.html.

BIOGRAPHICAL SKETCH

Hsin-Jung Lin was born in Pingtung, Taiwan and grew up in southern Taiwan. Ze[1] went to National Chiao Tung University majoring in Electrical and Control Engineering. Instead of getting a job as an engineer like most NCTU graduates do, Hsin-Jung started zir Ph.D program in Physics at the University of Florida in 2006. After finishing the first year courses, ze worked in LIGO (Laser Interferometer Gravitational-Wave Observatory) designing the Mach-Zehnder electro-optic modulator for advanced LIGO. In 2009, Hsin-Jung switched to the field of planetary sciences.

[1] ”Ze” and ”zir” are gender-neutral pronouns.